# Modeling and Simulation of Electronic Excitation in Oxygen-Helium Discharges and Plasma-assisted Combustion

A thesis accepted by the Faculty of Aerospace Engineering and Geodesy
of the University of Stuttgart in partial fulfillment of the requirements
for the degree of Doctor of Science (Dr. rer. nat.)

by

**Nikolaj Kuntner**

born in Vienna

main referee: Prof. Dr. rer. nat. Uwe Riedel
co-referee: Prof. Dr.-Ing. Stefanos Fasoulas
date of defense: 31.5.2017

Institute of Combustion Technology for Aerospace Engineering
University of Stuttgart

2018

Herzlich möchte ich an dieser Stelle meinen Vorgesetzten und Lehrern
Uwe Riedel und Nadja Slavinskaya für eine prägende Zeit am DLR Stuttgart danken
sowie meinen Kollegen und Kolleginnen für wohl etwa 900 Kaffees um drei.

Ich widme diese Arbeit meiner Mutter Ursula.

# Contents

Table of Symbols . . . . . 9
List of Figures . . . . . 11
List of Tables . . . . . 14
Kurzfassung . . . . . 16
Abstract . . . . . 18

**I Introduction 20**

**1 Principles of plasma assisted combustion 20**

1.1 Thesis overview . . . . . 22
1.2 Types of plasma . . . . . 23
1.3 Redistribution of energy . . . . . 24
1.4 Types of processes for plasma chemical kinetics . . . . . 25
1.5 The basic strategy of plasma assisted combustion . . . . . 29
1.5.1 Plasma generation . . . . . 29
1.5.2 Heuristics . . . . . 30

**2 Discharge kinetics theory 31**

2.1 The interaction cross section . . . . . 31
2.2 The reaction rate coefficient . . . . . 32
2.3 The Boltzmann equation . . . . . 32
2.4 The electron energy distribution function . . . . . 34
2.5 Macroscopic observables from microscopic physics . . . . . 35
2.6 Discharge behavior of the constant current model . . . . . 36

**3 Chemical species generated in oxygen-helium discharges 37**

3.1 Energy hierarchy of electron-oxygen collision processes . . . . . 37
3.2 Rotationally and vibrationally excited states . . . . . 38
3.3 Singlet oxygen states $O_2(a^1\Delta_g)$ and $O_2(b^1\Sigma_g^+)$ . . . . . 39
3.4 Atomic oxygen and ozone . . . . . 40

3.5 Charged species and attachment/detachment . . . . . 40
3.6 Helium . . . . . 41

**4 Before this work** **42**
4.1 On oxygen plasma generation . . . . . 42
4.1.1 Excited oxygen yield . . . . . 43
4.1.2 On diluents . . . . . 45
4.1.3 Validation experiment . . . . . 45
4.1.4 Other notable oxygen discharge studies . . . . . 48
4.2 On plasma assisted combustion . . . . . 49
4.2.1 Hydrogen gas studies . . . . . 49
4.2.2 Methane gas studies . . . . . 50
4.2.3 Syngas studies . . . . . 50

**5 Experiment and results at Magdeburg University** **51**
5.1 Description of the discharge and burner setup . . . . . 51
5.2 Description of the voltage generator . . . . . 53
5.3 Experimental results . . . . . 54
5.3.1 Plasma generation . . . . . 54
5.3.2 Flame . . . . . 54
5.3.3 Temperature development . . . . . 54

**II Oxygen-helium discharges and combustion mechanisms** **56**

**6 Rates for discharge zone mechanisms** **56**
6.1 Oxygen plasma . . . . . 58
6.1.1 Bimolecular reactions of neutral molecules . . . . . 58
6.1.2 Third body reactions of neutral species . . . . . 61
6.1.3 Elastic electron-atom and electron-molecule collisions . . . . . 62
6.1.4 Electron impact excitation of molecules and atoms . . . . . 62
6.1.5 Ionization processes . . . . . 63
6.1.6 Electron impact dissociation of a molecule . . . . . 64
6.1.7 Electron attachment . . . . . 65

6.1.8 Electron detachment . . . 65
6.1.9 Ion-molecule reactions . . . 67
6.1.10 Recombination of charged particles . . . 68
6.1.11 Diffusion to the wall and photoprocesses . . . 68
6.2 Helium and oxygen-helium plasma processes . . . 69

**7 Mechanisms for plasma assisted combustion 72**
7.1 Principal effect of plasma species on combustion kinetics . . . 72
7.2 Temperature rise in discharge- and combustion zone . . . 73
7.3 Hydrogen combustion . . . 74
7.3.1 On basic combustion mechanisms . . . 74
7.3.2 Excited oxidizer effect on hydrogen combustion pathways . . . 75
7.4 Methane combustion . . . 76
7.4.1 On basic combustion mechanisms . . . 76
7.4.2 Excited oxidizer effect on methane combustion pathways . . . 77

**III Model development and simulation 79**

**8 Modeling approach 79**
8.1 Available data and principal approach . . . 79
8.2 Power input and consumption . . . 81
8.3 Residence times . . . 82
8.4 Oxygen species relaxation time estimates . . . 83
8.5 Physics in the post-discharge zone . . . 84
8.6 Reduced electrical field and simulation tools . . . 84

**9 Mechanism validation 86**
9.1 Simulation approach . . . 86
9.2 Simulation results . . . 86
9.3 Simulation of the pure helium system . . . 88

**10 Simulation of the discharge volume 94**
10.1 Summary of approach and settings . . . 94
10.2 Simulation results . . . 95

10.2.1 Parameter study with respect to current density, I . . . . . 95
10.2.2 Species evolution in the discharge zone . . . . . 96
10.2.3 Parameter study with respect to current density, II . . . . . 103
10.2.4 Yield for nitrogen containing mixtures . . . . . 106
10.3 Discussion of the discharge zone . . . . . 107

**11 Simulation of the burner zone** **110**
11.1 Simulation approach . . . . . 110
11.2 Simulation results . . . . . 110
11.2.1 Methane combustion . . . . . 110
11.2.2 Hydrogen combustion . . . . . 112
11.3 Discussion of the burner zone . . . . . 113

**12 Summary** **115**

**References** **116**

**Appendix** **125**
A) Physical constants . . . . . 125
B) Implementation of the Boltzmann equation . . . . . 125

## Table of Symbols

| Latin Character | Physical quantity | Unit |
|---|---|---|
| $A$ | cross section | $\mathrm{m}^2$ |
| $c$ | species concentration | $\mathrm{m}^{-3}$ |
| $C$ | heat capacity | $\mathrm{kg\,m^2 s^{-2}/K}$ |
| $d$ | discharge gap distance | m |
| $E$ | electrical field strength | $\mathrm{kg\,m\,s^{-3}/A}$ |
| $E_a$ | threshold energy | $\mathrm{J = kg\,m^2/s^2}$ |
| $E_{\mathrm{kin}}$ | kinetic energy | $\mathrm{J = kg\,m^2/s^2}$ |
| $f$ | distribution function | various |
| $f_0$ | pulse frequency | $\mathrm{s}^{-1}$ |
| $f_{\mathrm{rep}}$ | repetition rate | $\mathrm{s}^{-1}$ |
| $\mathfrak{F}$ | distribution function | $\mathrm{m^{-3}s^3}$ |
| $F$ | force | $\mathrm{N = kg\,m/s^2}$ |
| $g$ | relative velocity | m/s |
| $I$ | electrical current | A |
| $\mathcal{I}$ | Boltzmann cross section | $\mathrm{m}^2$ |
| $j$ | current density | $\mathrm{A/m}^2$ |
| $\mathcal{J}$ | Boltzmann current term | $\mathrm{m}^2$ |
| $k$ | reaction rate coefficient | $\mathrm{m}^{3n}/\mathrm{s}$ |
| $l$ | tube length | m |
| $m$ | mass | kg |
| $M$ | mass | kg |
| $n$ | particle density | $\mathrm{m}^{-3}$ |
| $N$ | particle number | 1 |
| $p$ | pressure | $\mathrm{Pa = kg\,m^{-1}s^{-2}}$ |
| $P$ | electrical power | $\mathrm{W = kg\,m^2/s}$ |
| $\mathcal{P}$ | microscopic power | $\mathrm{W = kg\,m^2/s}$ |
| $q$ | gas flow rate | $\mathrm{m}^3/\mathrm{s}$ |
| $\mathfrak{q}$ | electrical charge | $\mathrm{C = A\,s}$ |
| $\mathcal{Q}$ | collision integral | $\mathrm{m\,s/kg}$ |
| $r$ | reaction rate | $\mathrm{m}^{-3}/\mathrm{s}$ |
| $\mathfrak{r}$ | radial distance | m |
| $R$ | electrical resistance | $\mathrm{\Omega = kg\,m^2 s^{-3}/A^2}$ |
| $t$ | time | s |
| $T$ | temperature | K |
| $U$ | electrical voltage | $\mathrm{V = kg\,m^2\,s^{-3}/A}$ |
| $v$ | particle velocity | m/s |
| $V$ | volume | $\mathrm{m}^3$ |
| $x$ | spatial distance | m |
| x | species mole fraction | 1 |

| **Greek Character** | **Physical quantity** | **Unit** |
|---|---|---|
| $\epsilon$ | energy | $\mathrm{kg\,m^2/s^2}$ |
| $\eta$ | efficiency | 1 |
| $\eta_P$ | power efficiency | 1 |
| $\mu$ | mobility | $\mathrm{A\,s^2/kg}$ |
| $\nu$ | frequency | $\mathrm{s^{-1}}$ |
| $\rho$ | resistivity | $\mathrm{m^3 kg\,A^{-2} s^{-3}}$ |
| $\varrho$ | charge density | $\mathrm{A\,s/m^3}$ |
| $\sigma$ | interaction cross section | $\mathrm{kg\,m^2/s^2}$ |
| $\sigma_{\mathrm{e^-}}$ | conductivity | $\mathrm{A^2 s^3 m^{-3} kg^{-1}}$ |
| $\tau$ | characteristic time | s |

A subscript $i, j, k, l$ always denotes either a numerical index or a species index (as in $n_i$). Symbols such as species names are often used as index as well (as in $n_{\mathrm{O_2}}$).

The prefix $\Delta$ is used either to signify differences (as in $\Delta E := E_{\mathrm{kin}} - E'_{\mathrm{kin}}$) or to denote an interval on a grid (as in $\Delta V$ vs. infinitesimal $\mathrm{d}V$). Several auxiliary greek letters are used for angles and to denote detailed information about chemical states (as in $\mathrm{O_2}(X^3\Sigma_g^-)$).

| **Symbol** | **Usage** |
|---|---|
| $\mathrm{A, B, C}$ | auxiliary species name |
| $M$ | collision partner in third body reactions |
| $\mathrm{O_2}$ | molecular oxygen in the ground state, $\mathrm{O_2}(X^3\Sigma_g^-)$ |
| $\mathrm{O_2^*}$ | molecular oxygen in an excited state |
| $\mathrm{O^*}$ | atomic oxygen in an excited state |
| $h\nu$ | photon particle |

# List of Figures


1 Discharge generator at the University of Magdeburg. . . . . 21

2 Electron- and ion motion in a Townsend breakdown (graphic from [29]). . . . 30

3 Energy loss fraction for an oxygen-helium mixture ($O_2$ : He = 1 : 30) vs. constant reduced electrical field strengths at one nanosecond - this system is discussed in more detail in subsection 8.6; The dissociation process presented here (dark blue line) must be understood as production of the dissociative intermediate $O_2(B^3\Sigma_u^-)$; The largest electron energy fraction is transferred in elastic collisions with helium in $He + e^- \rightarrow He + e^-$ and is not shown in the graph; The energy fractions for ionization by electron impact, e.g. $O_2 + e^- \rightarrow O_2^+ + e^- + e^-$, are also not shown. . . . . 44

4 Discharge gap in the experiment performed at Bochum University [34]. . . . 46

5 Working conditions without arcing established for the He-flow of 1.5 *slpm* [47]. 47

6 The concentrations of O for 0.6% oxygen in helium, graphic from [47]. [O] has been obtained by TALIF and MBMS measurements, inside the tube as well as at the effluent. . . . . 47

7 Left: Computer generated design of the discharge zone, also depicted in figure 8; Right: Cross section of the burner module on top of the discharge outlet. . . . . 51

8 Full plasma assisted combustion setup; Right: Differently colored cables provide oxidizer, fuel and cooling gas; Left: The voltage cables on both ends of the discharge are black. . . . . 52

9 Temperature differences between the injection and the burner outlet, vs. temperature at the burner outlet. For each duty cycle, a gray line connects the values for pure helium (left) and a mixture with 3.2% oxygen addition (right). For those pairs, temperature at the outlet differs by a factor of about 0.86 and this value is largely independent of duty cycle. . . . . 55

10 Experiment and associated computational model for the plasma discharge. . 80

11 Varying values of $E/n$ for a species ratio of $O_2$ : He = 1 : 30. . . . . 85

12 Development for different mechanisms for $I = 2\,\mathrm{mA}$. Low to high O concentration: variation of Chernysheva et al. [18], version of [18] augmented with oxygen-helium interaction processes, variation of Waskoenig et al. [107]. . . 87

13 Comparison of the final concentrations at $t = 1.6\,\mathrm{ms}$ of the relevant species vs. current. . . . . 88

14 EEDF (log-scale) for the $j = 3.5\,\mathrm{mA/mm^2}$ simulation of the pure helium system for a broad variety of times. The almost horizontal line corresponds to the first time step at $t \leq 10^{-9}\,\mathrm{s}$. . . . . 89

15 Electrical field for the $j = 3.5\,\mathrm{mA/mm^2}$ simulation of the pure helium system. 90

16 Selection of rates for the $j = 3.5\,\mathrm{mA/mm^2}$ simulation. . . . . 91

17 Selection of species concentration for the $j = 3.5\,\mathrm{mA/mm^2}$ simulation. . . . . 92

18 Electrical field for a simulation run, where $3.2\%\,O_2$ has been added to helium. 93

19 Predicted residence times $\tau$, using the fit $\tau(j) = \frac{\mathrm{A/cm^2}}{j}\,0.218\,\mathrm{ms}$. The fit of the data is more accurate for larger current densities. The least current density value which gives good convergence is $2 \times 10^{-3}\mathrm{A/cm^2}$. . . . . 96

20 Excited species concentrations for the simulation with $j = 0.5\,\mathrm{A/cm^2}$. . . . . 97

21 Relevant oxygen species concentrations (linear time axis) in the discharge zone for $j = 0.5\,\mathrm{A/cm^2}$. The species $O_2(a^1\Delta_g)$ was still growing in the last short zone 21. In contrast, now entering the large tube, the system witnesses a sudden expansion, temperature drop and decay of all excited species. . . . . 98

22 Oxygen species mole fractions for the simulation with $j = 0.5\,\mathrm{A/cm^2}$ The kink in the graphic is a mere artifact of few data points for simulations with small $N_2$ fractions, which require exponential computational resources. . . . . 99

23 Oxygen species mole fractions for the simulation with $j = 0.05\,\mathrm{A/cm^2}$. . . . . 100

24 Oxygen species concentrations in the first tube after the discharge for $j = 0.5\,\mathrm{A/cm^2}$. . . . . 102

25 Oxygen species concentrations in the second tube after the discharge for $j = 0.5\,\mathrm{A/cm^2}$. The parameter change at the sudden tube expansion result in a short delay of the de-excitation of $O_2(a^1\Delta_g)$. As $O_2(b^1\Sigma_g^+)$ and O de-excitate resp. recombine, we see a peak of the $O_2(a^1\Delta_g)$ mole fraction. . . . . 103

26 Energy as temperature difference over heat capacity stored in plasma vs. current density $j$, displayed using polynomial fits for two regimes . . . . . 104

27 Final species concentrations for $O_2(a^1\Delta_g)$ (gold), $O_2(b^1\Sigma_g^+)$ (green) and O (blue) vs. constant current value at the end of the discharge zone (solid lines), and beginning for the mixing zone (dashed lines). . . . . 105

28 Energy stored in the mixtures vs. constant current value. . . . . 106

29 Mole fractions for two constant current simulations with discharge parameters as in figure 22: An initial $N_2$ fraction of about 1/3 reduces the excited oxygen yield most significantly. . . . . 107

30 Mole fractions at $t = 5 \times 10^{-4}$s for $q_{O_2} = 0.01\,\mathrm{m}^3/\mathrm{h}$ and $q_{He+N_2} = 0.3\,\mathrm{m}^3/\mathrm{h}$ and $j = 0.2\,\mathrm{A}/\mathrm{cm}^2$ for various ratios $He : N_2 = 1 : x$. For low $N_2$ fractions, stable results could not be obtained computationally. . . . . 108

31 Flame velocity for the hydrogen flame for various excitation levels. . . . . 113

# List of Tables


1 Crucial definitions in the computer implementation of plasma physics. . . . . 35

2 Possible products of the electron impact process, sorted by electron energy. . 38

3 Energies for six electronically excited states of molecular oxygen, [15]. . . . . 39

4 Reactions of neutral oxygen species [18]. . . . . 59

5 Trimolecular reactions of neutral species [18]. . . . . 61

6 Collision efficiency parameters of the third body reactions in table 5. . . . . 61

7 Elastic electron atom- and electron-molecule collisions [18]. . . . . 62

8 Electron impact excitation of molecules and atoms [18]. . . . . 63

9 Ionization processes [18]. . . . . 63

10 Electron impact dissociation of a molecule [18]. . . . . 64

11 Electron attachment [18]. . . . . 65

12 Electron detachment [18]. . . . . 66

13 Ion-molecule reactions [18]. . . . . 67

14 Ion-molecule reactions, third body reactions [18]. . . . . 67

15 Bi- and trimolecular ion-molecule reactions [15]. . . . . 67

16 Recombination of charged particles [18]. . . . . 68

17 Recombination with electrons [18]. . . . . 68

18 Pure helium processes. [18]. . . . . 69

19 Oxygen-helium interaction processes [18]. . . . . 70

20 O destruction processes, [107]. . . . . 70

21 Possible Penning ionization reactions with gas temperature $T_g$ [107]. . . . . 71

22 Photoprocesses, [107]. Here $T_e$ denotes the electron temperature of the system. 71

23 Basic hydrogen combustion scheme. . . . . 75

24 Experimental data. . . . . 80

25 Flow data estimates. . . . . 82

26 Characteristic times for discharge- and burner zone (third, resp. fourth column). 83

27 Experimental and calculated values of the validation experiment [25]. . . . . 86

28 Residence times required for the $O_2 : He = 1 : 30$ mixture to reach 900 K as a function of constant discharge current . . . . . 95

29 Rate coefficients for the simulation with $j = 0.5\,A/cm^2$. . . . . 100

30 Electronic rates for the simulation with $j = 0.5\,A/cm^2$. . . . . 101

31 Smaller $\eta$-factor for the simuation with $j = 0.5\,A/cm^2$. The $\eta$-factor for $O_2 + e^- \rightarrow O_2(B^3\Sigma_u^-) + e^-$ grows up to 60% during the whole discharge developement, followed by the factor for $He + e^- \rightarrow He + e^-$ and $O_2 + e^- \rightarrow O_2(4.5) + e^-$. . . . . 101

32 Chemical rates for $j = 0.5\,A/cm^2$. . . . . 101

33 Mole fractions entering the mixing zone for $j = 0.5\,A/cm^2$. . . . . 105

34 Methane premixed fuel- and discharge zone simulation output flow. . . . . 110

35 Mixing reactor temperatures vs. discharge outlet flow temperatures. . . . . 111

36 Hydrogen premixed fuel- and discharge zone simulation output flow. . . . . 112

37 Physical constants. . . . . 125

## Kurzfassung

Die vorliegende Arbeit untersucht die Erzeugung elektronisch angeregter Oxidatoren in nicht-thermischen Entladungen im Rahmen der plasma-unterstützen Wasserstoff- und Methanverbrennung bei atmosphärischen Drücken. Diese Bedingungen sind in der Verbrennungstechnik von praktischer Relevanz. Da die Umsetzung elektrischer Leistung in gezielte chemische Freiheitsgrade tendenziell durch geringe Molekül-Interaktion erleichtert wird, ist der atmosphärische Parameterbereich jedoch in der Literatur weitgehend unterrepräsentiert. Zielsetzung dieser Arbeit ist die Entwicklung und Validierung von akkuraten und effizienten Berechnungsmodellen, die für die Vorhersage der technischen Umsetzbarkeit einer plasma-unterstützen Verbrennung verwendet werden können.

Es wird ein Vergleich relevanter Literatur zu experimentellen und theoretischen Studien, sowie insbesondere die numerische Berechnung eines Versuchsaufbaus an der Universität Magdeburg zum Verhalten plasma-unterstützer helium-verdünnter Flammen durchgeführt. Hierbei wir zunächst mittels eines Radio-Frequenz-Generators ein Heliumstrom, welchem Sauerstoff beigemischt wurde, teilweise ionisiert. Das resultierende Plasma verlässt die Entladungszone und wird einer Mischung aus Sauerstoff und Wasserstoff bzw. Methan beigemischt und verbrannt. Die theoretische Diskussion umfasst dementsprechend die chemische Reaktionsmechanismen für drei Modelltypen: Räumlich 0-dimensionale Plasma-Entladungszonen, 1-dimensionale Pfropfenströmungen und schließlich 1-dimensionale Misch- und Flammenzonen. Solche Modelle können mit dem verwendeten Softwarepaket Chemical Workbench gekoppelt berechnet werden. Der technische Nutzen solch eines Aufbaues bedingt eine gute Effizienz der Umsetzung von elektrischer zu chemischer Energie. Die Erzeugung der nicht-thermischen Plasmen erfolgt rechnerisch durch die detaillierte Berechnung der zeitabhängigen Verteilungsfunktion der Elektronenenergie im Bereich der Entladung.

Für die Simulation der Plasmaentwicklung bis zum Brennkammerauslass werden, neben den Abmessungen des Versuchsaufbaus, die von den Experimentatoren in Magdeburg ermittelten Temperaturmesswerte für verschiedene Gaszusammensetzungen zugrunde gelegt. Verfügbare Reaktionsmechanismen für Sauerstoff-Plasmen mit Fokus auf elektronische Anregungszustände werden für den Kontext der Helium-Beimischung erweitert und die Auswirkung auf die Chemie von atomarem Sauerstoff und Ozon anhand eines verfügbaren Literaturexperiments validiert. Um die zeitliche Entwicklung der Speziesprofile zu ermitteln, wird eine Parameterstudie bzgl. der Leistung durch verschiedene elektrische Stromdichten durchgeführt, wobei die maximal zugeführte Energie festgehalten und durch den gemessenen Temperaturanstieg festgelegt ist. Schließlich werden Voraussagen für die Konzentrationen in den drei Zonen berechnet und Vorhersagen zur Verwendung von Stickstoff als Verdünnungsgas getroffen.

Das Verhalten der Mischung beim Quenching ohne Brennstoff oder Stickstoff stimmen für die eindimensionale Simulation mit dem experimentellen Ergebnis überein, so dass für die untersuchte Anlage auch bei atmosphärischen Drücken angeregte Sauerstoffteilchen noch Zentimeter über dem Auslass detektierbar sind. Da die Temperatur hier in der Plasmazone um mehrere hundert Grad steigt, spielt aufgrund der dann vermehrt einsetzenden Dissoziation die Spezies Ozon im Vergleich zum Aufbau im betrachteten Validierungsex-

periment eine verschwindende Rolle. Bei einem anfänglichen $O_2$-Molenbruch von 0,032 erreicht atomarer Sauerstoff hier für die Simulation mit einer hohen Stromdichte von $j = 0,5\,\mathrm{A/cm^2}$ einen Wert von 0,012 am Ende der Entladungszone, rekombiniert jedoch in der nachfolgenden Zonen wieder zu molekularem Sauerstoff. Der Molenbruch von $O_2(a^1\Delta_g)$ ist gegenüber O und $O_2(b^1\Sigma_g^+)$ stabiler, so dass selbst für den günstiger umsetzbaren Strom von $j = 0{,}06\,\mathrm{A/cm^2}$ vor der Flammenzone 11% $O_2(a^1\Delta_g)$ in $O_2$ generiert wird. Das Ergebnis der Berechnung der plasmachemischen Prozesse sagt hier voraus, dass ein Aufbau mit geringem Leistungsaufwand eine vergleichbar hohe Produktion von $O_2(a^1\Delta_g)$ bewirken kann. Nach instantanem Beimischen des Brennstoffes vor der Flammenzone reicht dies jedoch nicht für eine relevante Verbesserung der Flammencharakteristika. Darüber hinaus fällt der $O_2(a^1\Delta_g)$-Molenbruch bereits bei Anwesenheit geringer Stickstoffkonzentrationen auf einen verschwindenden Wert ($< 1\%$).

Das Modellierungsschema und die Simulation der Speziesprofile für die RF-Entladung und die nachfolgende Verbrennung bei atmosphärischen Drücken wurde damit validiert und liefert plausible Ergebnisse. Die beschriebenen Resultate für die Flammenzone lassen den effektiven Einsatz einer Oxidator-Plasmaquelle in dieser Konfiguration (RF-Plasma bei atmosphärischen Drücken) allerdings nicht als plausibel erscheinen.

Diese Arbeit wurde von der Deutschen Forschungsgemeinschaft unter der Projektnummer RI 839/5-1 finanziell unterstützt.

## Abstract

The present work concerns the generation of electronically excited oxidizers in non-thermal discharges in the context of plasma-assisted hydrogen and methane combustion at atmospheric pressures. These conditions are of practical relevance for the combustion technology. However, as the conversion of electrical power into particular, chosen chemical degrees of freedom is facilitated by low molecular interaction, the atmospheric parameter range is often neglected in the literature. The aim of this work is the design and validation of accurate and efficient computational models, which aid to the prediction for the possibility of technical realization of plasma-assisted combustion.

A literature comparison of relevant experimental and theoretical studies is conducted. Then, in particular, an experiment on the behaviour of plasma-assisted helium diluted flames, which was performed recently at the University of Magdeburg, is modeled and simulated. This system involves the partial ionization of an oxygen-helium flow with a radio frequency generator. The resulting plasma leaves the discharge zone and is mixed with a premixed oxygen-hydrogen or oxygen-methane flow. Accordingly, chemical reaction mechanisms for three model types are discussed: Spatially 0-dimensional plasma discharges, 1-dimensional plug flows and finally 1-dimensional mixing and flame zones. These models can be coupled using the Chemical Workbench software package. The technical usability of this system requires a good efficiency of the translation of electrical to chemical energy. The generation of non-thermal plasma is taken into account via detailed computation of the time-dependent electron energy distribution function in the discharge area.

The experimental results of the temperature development for various gas compositions are taken as the main input for the computation of the plasma dynamics. Available reaction mechanisms for oxygen plasma with a focus on electronically excited states are adapted for helium and the effect on the chemistry of atomic oxygen and ozone are validated. To understand the time development of species profiles, a parameter study with respect to various current densities is performed, in a way that is consistent with the temperature measurements. This enables the computation of the concentrations in all three modeling zones. Moreover, the influence of the effect of adding nitrogen to the mixture is estimated.

The simulated quenching behaviour of the plasma without the admixture of fuel or nitrogen matches the experimental results. As affirmed in the experiment, excited oxygen particles can be detected centimeters above the discharge outlet, even at atmospheric pressure. As the plasma temperature rises by several hundreds Kelvin, which aids particle dissociation, ozone only plays a small role in the dynamics of this setup. At an initial $O_2$-mole fraction of 0.032 and at a current density of $j = 0.5\mathrm{A/cm^2}$, the atomic oxygen mole fraction reaches a value of 0.012 at the end of the plasma zone. However, in the following zones a significant recombination to molecular oxygen is observed. The mole fraction of $O_2(a^1\Delta_g)$ is more stable than those of O and $O_2(b^1\Sigma_g^+)$, so that even at $j = 0.06\,\mathrm{A/cm^2}$, right before the flame zone, 11% $O_2(a^1\Delta_g)$ in $O_2$ is generated. These results imply that configurations with lower power consumptions can generate comparable amounts of $O_2(a^1\Delta_g)$. After instantaneous mixing with the fuel, none of these concentrations suffice for a significant improvement of the flame characteristics. In the presence of nitrogen, the $O_2(a^1\Delta_g)$ production is negligible altogether ($< 1\%$).

The model scheme and the simulation of species profiles for the RF discharge and its combustion at atmospheric pressures is validated and provides realistic results. However, the results for the flame zone outlined here, do not suggest the effectiveness of an oxidator discharge in this configuration at atmospheric pressures.

This work was financially supported by the German Research Foundation (Deutsche Forschungsgemeinschaft, DFG), under the project number RI 839/5-1.

# Part I

# Introduction

## 1 Principles of plasma assisted combustion

The capacity to affect charged particles using exterior electrical fields has motivated the research of a broad range of discharges in the context of combustion technology. From the perspective of chemical kinetics, the electrical power coupled to a combustion system manifests itself in three different ways:

- Heating of the gas,
- Excitation of rotational, vibrational and electronical particle states,
- Generation of charged species like ions and highly reactive radicals.

An enhancement by thermal means is unfocused and therefore the production of radicals and targeted excitation has a higher potential to reach high energy efficiency. For its potential to beneficially affect on flames of various configurations, non-equilibrium plasma treatment of oxidizers and fuel gases has been investigated extensively in recent years. At least under academic conditions [13], experiments of various different electrical discharges have demonstrated that the promoting action on combustion processes may result in the following:

- Reduction of ignition delay times,
- Extension of flammability limits, e.g. reduction of the inflammation temperature,
- Increase of flame stability and laminar flame speed,
- Increase of thermal flame thickness and flame luminosity,
- Reduction of soot formation.

The feasibility of practical implementations, especially at elevated pressures, remains to be established. And despite the grown interest and the progress being made, when compared to conventional combustion, the detailed chemical kinetics of plasma assisted combustion is still in its infancy. This is foremostly because discharge systems introduce a wealth of new parameters that are relevant for different time scales. Moreover, the dynamics of non-equilibrium systems, inhomogeneous electrical fields and discharge instabilities are a challenge for models and computations. The textbook series by Fridman [30] provides an introduction to plasma technology. An introduction paper to oxygen plasma production is presented by Ionin et al. [41], while topical overviews of plasma assisted combustion are provided by Starikovskiy [98, 99].

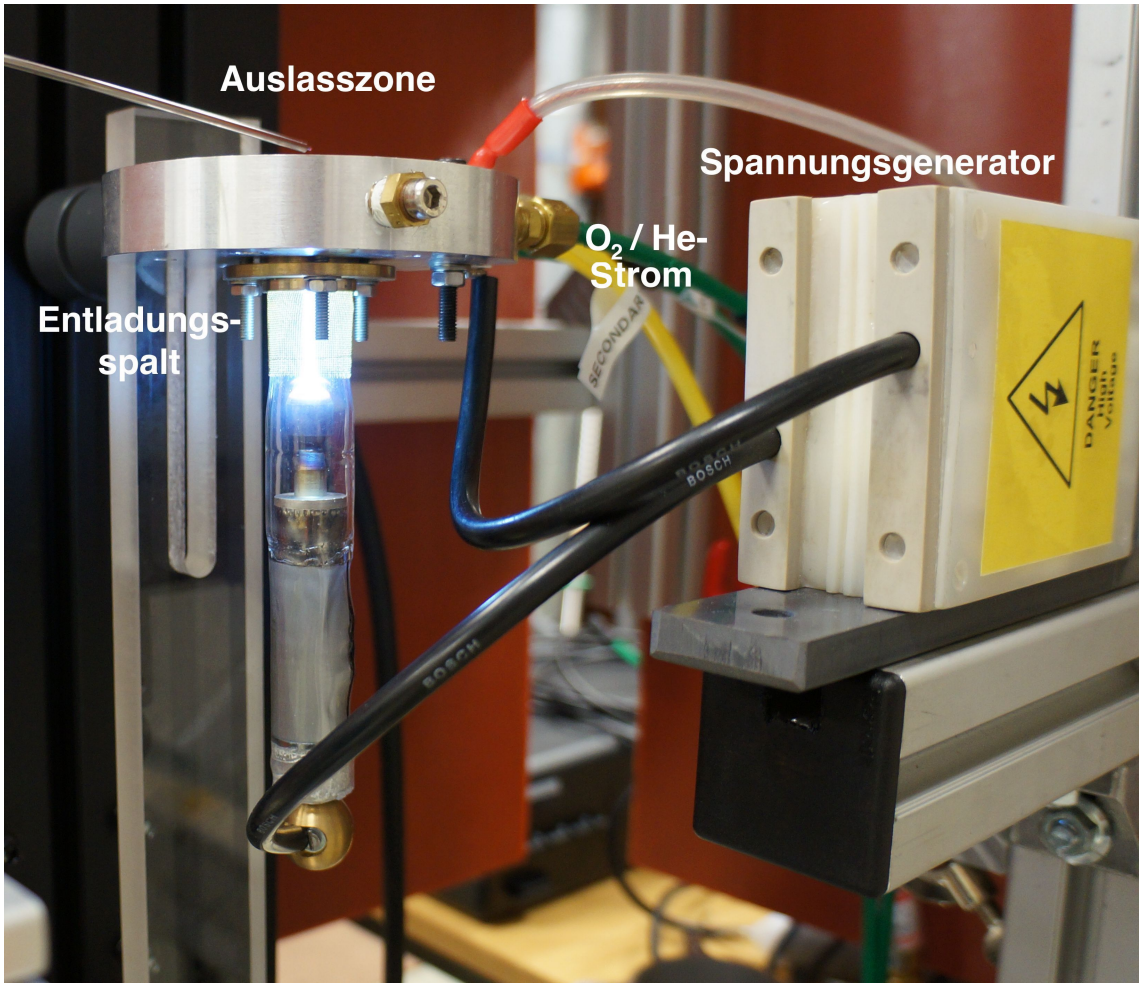


Figure 1: Discharge generator at the University of Magdeburg.

The present work concentrates on the study and simulation of non-equilibrium kinetics in the context of the research project *Combustion of renewable fuels assisted by non-thermal plasmas* operated by the *University of Magdeburg* in collaboration with the *German Aerospace Centre, Institute of Combustion Technology* and the *University of Stuttgart*. The installation consists of a high voltage radiofrequency generator (figure 1), a burner and measurement equipment providing temperature data, LIF diagnostics and spectroscopy. We are interested in the possibility of excitation of oxygen mixtures and its effect on a co-flow flame. Accordingly, the goal of this work is the simulation of atmospherical pressure $O_2$/He plasma discharge kinetics at temperatures below 1000 K, as well as hydrogen and methane-combustion with plasma treated oxidizers. This includes a detailed investigation of existing reaction mechanisms and their adaptation for the described experiment together with the development of appropriate modeling approaches.

## 1.1 Thesis overview

### Part I — Introduction

The present chapter serves as an introduction to the principal ideas of non-equilibrium plasma generation and its prospects in combustion technology. The concept underlying the derivation of reaction rate coefficients is the interaction cross section together with the Boltzmann equation. To aid the understanding of reaction mechanisms for plasma generation, the principal types of scattering processes are discussed. This is followed by an explanation of relevant classical statistical mechanics and charged fluid physics. After an overview of the peculiarities of the relevant plasma treated mixtures from the perspective of physical chemistry, recent experiments and theoretical studies on electronic excitation of oxygen and its effect on combustion are surveyed. We then give an outline of the present project, a description of the experiments performed, and their results.

### Part II — Oxygen-helium discharges and combustion mechanisms

The systems for which we will perform the simulations are divided with respect to different requirements, namely discharge- and combustion zone. This second part comprises a literature overview of reaction mechanisms on the level of detailed chemical kinetics. We conclude with a discussion of modifications for mechanisms suitable for the present study.

### Part III — Model development and simulation

Heuristics for the described experiments are performed and, taking into account the computational tools, possible physical models for simulations are discussed. The mechanisms developed previously are validated using available data from literature experiments. The systems are compared against each other and suggestions for improvements of the physical model as well as the reaction mechanisms are discussed.

Finally, we describe the results of the simulation of the main experiment. This is accomplished by the calculations of the electron energy distribution functions for different time steps, together with the corresponding reaction rates for electron collision, followed by the simulation of the plasma evolution and finally the simulation of the flames. The model is compared with the experimental results and we finish with a conclusion of the work.

The text closes with an appendix and a bibliography.

## 1.2 Types of plasma

Plasma is defined as an ionized gas with overall neutral charge. Examples for natural plasmas are stars, nebulae, pulsars, the aurora borealis, lightning, solar wind or the ionosphere [15]. Some artificial or industrial plasma are the following: Lamps, plasma screens, plasma torches, production of X-ray, propulsion plasmas and nuclear fusion. Reactive species generated in plasma discharges find their use in plasma treatment for deposition and there are various applications in medicine [30, 88]. This list demonstrates how the same long-range electromagnetic forces lead to an extremely rich range of phenomena. For our purposes, it is useful to divide plasmas into two main categories: Non-thermal plasmas are usually defined in contrast to thermal plasmas, by the existence of a large temperature gap between different subsystems. In particular in the former case, the free electron temperature $T_\mathrm{e}$ (i.e. a fraction 2/3 of the mean energy) is high, while the heavy particle temperature $T_\mathrm{gas}$ is still low. A prominent example for the utilization of thermal plasmas in combustion technology is spark ignition. We are going to be concerned with the much less understood case of non-thermal plasmas of moderate gas temperature (several hundred Kelvin), and when the ratio of charged to uncharged particles (ionization degree) typically lies between $10^{-7}$ and $10^{-4}$.

**Thermal plasmas:** This regime is characterized by hot equilibrium conditions of $T_\mathrm{e} = T_\mathrm{gas} > 10^3\,\mathrm{K}$. The electron and ion densities are very high and even complete ionization is possible. Arc discharges are examples for hot thermal plasmas and here thermal ionization and Joule heating play a significant role. Such thermal conditions can be run at high pressures and find their application in welding and fusion processes. However, for the plasma chemical applications we are interested in, such high temperatures lead to electrode problems, imply a low excitation selectivity and hence a limited energy efficiency.

**Non-thermal plasmas:** When dealing with a range of subsystems at different temperatures, we are in the regime of non-equilibrium physics. The typical temperature hierarchy of non-thermal plasmas is

$$T_\mathrm{e} > T_\mathrm{vib} > T_\mathrm{rot} \approx T_\mathrm{ion} \approx T_\mathrm{gas},$$

where $T_\mathrm{ion}$ is the ion temperature and $T_\mathrm{vib}, T_\mathrm{rot}$ denote the temperature of vibrationally and rotationally excited particles, respectively. We may furthermore speak of cold plasmas when $T_\mathrm{e} \approx 1\,\mathrm{eV} = 10^4\,\mathrm{K}$ and $T_\mathrm{gas}$ is at room temperature. Types of discharges which fall in this regime are low pressure discharges, corona discharges (AC, DC or pulsed), dielectric barrier discharge (AC or pulsed), nanosecond discharges, among others. Examples for applications of those devices are glow discharges, plasma lamps or plasma screens. In this work, we focus on so-called warm or intermediate plasmas, $T_\mathrm{e}$ is higher than $T_\mathrm{gas}$, but the latter can still reach thousands of Kelvin. Corresponding discharges are radio frequency or microwave discharges, low current arcs, gliding arcs, sparks or atmospheric pressure glow discharges. Applications are, for example, corona discharges for treatment of polymer fibers and plastics, sterilization and packaging, or radio frequency discharges for plasma etching or treatment of microelectronics. For a classification of discharge types see ref. [60].

## 1.3 Redistribution of energy

In the statistical description of a gas or plasma, one deals with a large set of possible microscopic states of the system. The state space depends on the system to be described, but it is generally given by an array of particles, which are moreover classified into species types $i$ with different properties. Those are, for example, their particle mass $m_i$, their charge $q_i$ or the list of their internal degrees of freedom. The most important are called translational, rotational, vibrational and electronical. The configuration of a single particle is determined by (the probabilities for) the value of those degrees of freedom. Microscopic data for individual particles are for example the particle velocity $v$ as well as translational, rotational and electronical quantum number [28]. If the values for the particle's degrees of freedom are discrete, one speaks of excitations and then one must also consider particles with different excitation levels as different species. So for example, $O_2$, $O_2(a^1\Delta_g)$ and $O_2(b^1\Sigma_g^+)$ are three oxygen molecules with different electronical configuration. The degrees of freedom are all associated with certain quanta of energy. One can expect the rotational quanta of $\approx 0.03\,\mathrm{eV}$ ($\hat{=}\ 300\,\mathrm{K}$), the vibrational quanta to range between 0.2 and $2\,\mathrm{eV}$ ($\hat{=}\ 1000\,\mathrm{K}$ to $3000\,\mathrm{K}$), and the electronical quanta to lie above that, from $\approx 3$ to $10\,\mathrm{eV}$ [98]. When a particle gains an even higher energy, ionization or even the dissociation of the particle may occur.

Particles are excited in scattering events and there is a simple way of dividing them into three principle types: Consider two colliding particles of masses $m$ and $M$ and denote their velocity by $v_m$ and $v_M$, respectively. The kinetic energy is

$$E_{\mathrm{kin}} := \tfrac{1}{2}mv_m^2 + \tfrac{1}{2}Mv_M^2.$$

If $g := v_m - v_M$ denotes the relative velocity and if primed velocities denote the changed quantities after a collision took place, then the change of the total kinetic energy of the system is given by

$$\Delta E_{\mathrm{kin}} := E_{\mathrm{kin}} - E'_{\mathrm{kin}} = \tfrac{1}{2}\tfrac{mM}{m+M}\left(g^2 - g'^2\right).$$

This variable is used to distinguish three types of collision processes:

- $\Delta E_{\mathrm{kin}} = 0$ ... elastic encounters,
- $\Delta E_{\mathrm{kin}} < 0$ ... inelastic encounters,
- $\Delta E_{\mathrm{kin}} > 0$ ... super-elastic encounters.

As the total energy of the particle system is conserved, an energy change $\Delta E \neq 0$ is associated not only with momentum exchange, but also with a state transition or change of species. The electronical excitation by electron impact

$$\mathrm{A} + \mathrm{e}^- \rightarrow \mathrm{A}^* + \mathrm{e}^-$$

and related quenching processes

$$\mathrm{A}^* + \mathrm{B} \rightarrow \mathrm{A} + \mathrm{B}$$

will be a particular focus for us. These processes are associated with energy barriers, which can be computed via quantum chemical methods. In practice, the resulting values are very

often presented in power series expansions and so the data is given in terms of the associated coefficients. From the elementary theory it follows that the energy of a molecule is generally composed of electronical, vibrational and rotational contributions. This field of study has large overlap with spectroscopy, but we will not develop it here.

For low energy systems, the kinetic energy of particles participating in the collision changes often merely redistributes, so that $\Delta E = 0$. Reactions with internal energy exchange are of course at the core of chemistry, but elastic collisions can't be neglected either. In particular, we will discuss this type of collisions for reactions $\mathrm{A} + \mathrm{e}^- \to \mathrm{A} + \mathrm{e}^-$. The behavior of many physical systems can be qualitatively understood if one knows about the time scales at which these different types of processes take place. The previous example is very important for momentum and energy redistribution in reactive plasmas, because energy is generally transferred to the electrons first. They are the most mobile charged species, which then excite the background gas species. The average kinetic energy transfer fraction for two particles of masses $m, M$ can be estimated using the dimensionless ratio $\frac{2\,m\,M}{(m+M)^2}$. In the limiting case of $m \ll M$, one gets $\frac{2\,m}{M}$. For electrons and ions this is only about $\approx 10^{-4}$. Turning to a less detailed description suitable for computer simulations, one defines the concentrations $c_i := N_i/V$, where $N_i$ are the corresponding particle numbers of the global gas state and $V$ is the characteristic volume of our system. The concentration of a species A is conventionally denoted by [A]. Chemical kinetics theory is concerned with setting up a system of differential equations for each chemical reaction. This is the topic of the second chapter, *Oxygen-helium discharges and combustion mechanisms*. The energy of the global state, given by the sum of all energy contributions, is constant and there are of course similar laws for total mass, charge or species conservation. The kinematics then tells us how the values of the particles degrees of freedom can be rearranged. We want to classify chemical reactions by the energy transfer process which take place. For example, the de-excitation process

$$\mathrm{H_2} + \mathrm{O_2}(a^1\Delta_g) \to \mathrm{H_2} + \mathrm{O_2}$$

turns electronical energy into translational energy, which is an attribute denoted by $E$-$T$. Rotational energies are significantly lower than chemical reaction thresholds and rotational-translational relaxation, $R$-$T$, is fast (e.g. $\approx 0.5\,\mathrm{ns}$ for oxygen and nitrogen in air). Hence, its only effect for plasma assisted combustion can be incremental gas heating. Meanwhile, the vibrational-translational relaxation, $V$-$T$, is rather slow ($\approx 10 - 100\,\mu\mathrm{s}$) [98]. The main types of energy transfers are: $T$-$T$, $R$-$T$, $V$-$T$, $E$-$T$, $E$-$R$, $E$-$V$, $V$-$R$ and $V$-$V$.

## 1.4 Types of processes for plasma chemical kinetics

A detailed understanding of plasma kinetics comprises knowledge of non-equilibrium processes involving electrons, ions and higher particle excitations. Broadly, we are concerned with

- Initial plasma-chemical processes involving electrons,
- Secondary plasma chemical processes involving molecular and atomic ions,
- The chemical reactions involving neutral atoms and molecules

For simulation purposes, processes involving electrons are always associated with a bare microscopic scattering cross section $\sigma$. These are used as input for the Boltzmann solvers, as will be described in detail in the second section. The resulting reaction rates are then different for different simulations. In the following discussion, we start describing main heavy particle processes. Unless otherwise stated the symbols A, B and C will denote any atom, molecule or the electron.

• **Equilibrium reactions of neutral molecules** Those are processes where the reactants are ground state species. This includes bonding and recombination reactions, but the products can also include excited species.

• **Reactions of neutral molecules under non-equilibrium conditions** Here the reactants are excited species. Consider a recombination of uncharged heavy particles yielding molecules

$$\mathrm{A} + \mathrm{B}^* \rightarrow \mathrm{A} + \mathrm{B}$$

or also

$$\mathrm{A} + \mathrm{B}^* \rightarrow \mathrm{AB}.$$

A reaction of the former type indicates an energy transfer from internal to kinetic energy.

For such processes, the rate expressions can become quite complicated, since e.g. for vibrationally excited reacting particles, the rate might depend on the temperature $T$ and also on the vibrational temperature $T_{\mathrm{vib}}$. However, in simulations, such reactions are very often approximated by a simple constant value. If $T_{\mathrm{vib}} > T$, then there is vibrational energy to be gained, and hence the reaction

$$\mathrm{A} + \mathrm{BC}(v) \rightarrow \mathrm{AB} + \mathrm{C}$$

typically takes place faster than

$$\mathrm{A} + \mathrm{BC} \rightarrow \mathrm{AB} + \mathrm{C}.$$

• **Electron impact excitation of atoms and molecules**

$$\mathrm{A} + \mathrm{e}^- \rightarrow \mathrm{A}^* + \mathrm{e}^-.$$

Those reactions are the major player in terms of particle excitation for plasma assisted combustion.

• **Dissociation of atoms and molecules**

$$\mathrm{AB} + \mathrm{e}^- \rightarrow \mathrm{A} + \mathrm{B} + \mathrm{e}^-.$$

On a refined microscopic level, these reactions in particular are often taking place only stepwise, i.e.

$$\mathrm{AB} + \mathrm{e}^- \rightarrow \mathrm{AB}^* + \mathrm{e}^-,$$

followed by

$$\mathrm{AB}^* \rightarrow \mathrm{A} + \mathrm{B}.$$

Note that the excited particle $AB^*$ does not have to arise in an electron impact collision.

• **Ionization processes**

◦ **Direct ionization by electron impact**

$$A + e^- \rightarrow A^+ + e^- + e^-.$$

Here A is a previously unexcited atom, radical or molecule. These are important when electrical fields and hence the electron energies are quite high, but the excitation levels of neutral species are moderate.

◦ **Stepwise ionization by electron impact**

$$A^* + e^- \rightarrow A^+ + e^- + e^-.$$

These will be relevant in thermal and energy-intense discharges. This is the case, specifically, when $n_e \gg n_0$ and/or $n_{A^*} \gg 0$.

◦ **Ionization by collision of heavy particles**

These can take place whenever the energy of collision partners exceeds the ionization potential. As such, the probability for these processes increases when the molecules are vibrationally or electronically excited.

We speak of Penning ionization when the impact partner is electronically excited. Similarly, a Penning dissociation is a process where a particle dissociates due to excited particle impact.

◦ **Photo-ionization**

$$A + h\nu \rightarrow A^+ + e^-.$$

Photo-ionization is mostly relevant in thermal plasmas.

As a remark, note that photons can also be a by-product of particle reactions.

• **Ion-molecular reactions** These are reactions including simple charge transfer

$$A^- + B \rightarrow A + B^-,$$

where we allow $A^-$ to be an electron, as well as thermal decomposition processes

$$AB^- + C \rightarrow A^- + B + C.$$

At least in equilibrium, ion-molecule reactions tend to be not too sensitive to changes of temperature. For computer simulations, the rates are mostly assumed to be constant. This is explained by the relatively simple form of the cross sections for the "effective polarization interaction" $\propto \mathfrak{r}^{-4}$ for the ion-molecule collisions [15]. Conversely, ion-ion reactions discussed below, e.g. processes of type $A^- + B^+ \rightarrow AB$, have a much higher rate than reactions involving uncharged molecules, i.e. by a factor 2 or more. This is due to the strong Coulomb attraction.

The next few types can be considered subtypes of the ion-molecular reaction class.

• **Electron detachment** After direct ionization processes by electron impact, reactions like

$$A^- + B \rightarrow A + B + e^-$$

or

$$A^- + B \rightarrow AB + e^-$$

are secondary sources of electrons, after direct ionization processes.

• **Electron attachment** This process can be seen as a transfer of electric charge to A resp. $A^*$ and it is important to note that the interaction behavior $A^-$ will be significantly different than that of the light electron:

$$A + e^- \rightarrow A^-,$$

$$A^* + e^- \rightarrow A^-.$$

In the second reaction, if $A^*$ is a composite molecule, the resulting high energy ion $A^-$ is prone to fast dissociation. Three body attachment processes are possible as well.

Lastly, we have processes of the form

$$AB^* + e^- \rightarrow A + B^-.$$

This includes the case where the species A and B coincide.

• **Recombination** These are processes where positive and negatively charged particles recombine to neutral species:

$$A^+ + B^- \rightarrow A^* + B^*$$

Important processes when the negative particle is an electron are

$$A^+ + e^- \rightarrow A^* + A^* + h\nu,$$

$$A^+ + e^- + M \rightarrow A^* + M,$$

$$A^+ + e^- + e^- \rightarrow A^* + e^-.$$

For molecular ions, recombination very often takes the form

$$AB^+ + e^- \rightarrow A^* + B^*.$$

• **Surface ionization** Via electron-, ion-, or photon impact, or via surface heating.

• **Quenching at the wall** Chemical reaction of excited species or radicals with the environment.

• **Photoprocess** Spontaneous radiation is of the form

$$A^* \rightarrow A + h\nu,$$

where $A^*$ is any high energy state and $h\nu$ denotes electromagnetic waves. In the simulation, this process is associated with energy losses.

## 1.5 The basic strategy of plasma assisted combustion

A high temperature $T$ and a low particle process specific threshold energy $E_a$ is usually beneficial with respect to the speed at which a gas reaction takes place. This is apparent, for example, when the rate coefficient $k$ is given by $k \propto \mathrm{e}^{-E_a/k_B T}$, where $k_B$ is Boltzmann's constant. Accelerating a reaction by raising $T$ is costly, since this amounts to heating up the whole mixture. The goal of plasma assisted combustion is to selectively excite particular species, as their higher states can have desirable chemical properties when compared to the ground states [64]. Charged particles can be energized via external electrical fields and the idea is therefore to achieve the excitation via electron collisions, for example

$$\mathrm{O_2} + \mathrm{e^-} \rightarrow \mathrm{O_2}(a^1\Delta_g) + \mathrm{e^-}.$$

### 1.5.1 Plasma generation

The first goal of a plasma discharge system is to generate charged particles by initiation of a chain of ionization reactions. To this end, two electrodes are placed in midst of a non-charged gas volume. The voltage results in an electrical field, which is capable of dragging charged particles from one electrode to the other. Initially, single electrons from the cathode will propagate through the volume and occasionally collide with other particles. If their kinetic energy exceeds the ionization energy of the gas species in the bulk gas, $E_{\mathrm{kin}} \geq I$, ionization processes

$$\mathrm{A} + \mathrm{e^-} \rightarrow \mathrm{A^+} + \mathrm{e^-} + \mathrm{e^-}$$

take place and more electrons are freed and are accelerated, see figure 2. These electrons in turn participate in excitation processes such as the excited oxygen generation example above. The idea is to carry vibrationally, rotationally and/or electronically excited particles produced in the discharge zone into the combustion zone. Intensifying the chemical kinetics, e.g. by decreasing barriers for endoenergetic reactions, can be much more energy efficient than simply heating up the whole mixture [9]. Note that the described technology is not restricted to plasma assisted combustion. The influence of electrical fields on charged particles happens at any temperature and hence also provides a means of flame control and flame stabilization.

We are mainly interested in the production of single oxygen species $\mathrm{O_2}(a^1\Delta_g)$ and $\mathrm{O_2}(b^1\Sigma_g^+)$, which carry an energy 22.5 kcal/mol resp. 36.5 kcal/mol, when compared to the unexcited oxygen molecule. The $\mathrm{O_2}(a^1\Delta_g)$ particle has a relative long lifetime and is therefore singled out as interesting candidate for flame enhancement. This will be discussed in the next section. To reach the goal set out here, we must first understand discharge systems and their parameter spaces.

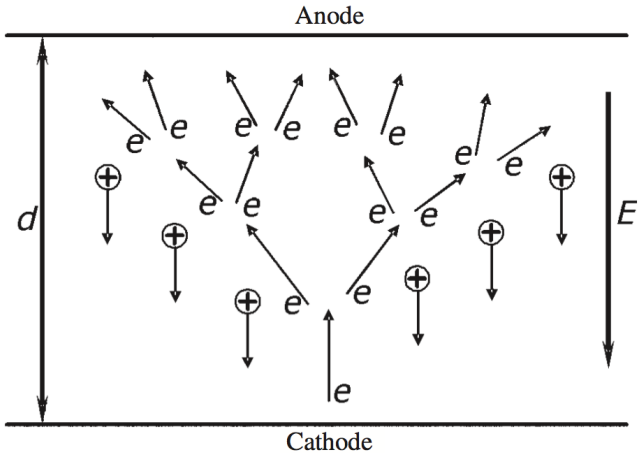


Figure 2: Electron- and ion motion in a Townsend breakdown (graphic from [29]).

### 1.5.2 Heuristics

In the next section the details of the physical theory of plasmas is studied. Meanwhile, we are already in the position to qualitatively understand the behavior of discharges with respect to parameter changes. We use Newton's law $F = m\,a$ relating force $F$ to mass $m$ and acceleration $a$, together with the expression $F = \mathfrak{q}\,E$, which defines electrostatic force in terms of the charge $\mathfrak{q}$ in an electrical field of strength $E$:

- Stronger acceleration leads to high velocity and kinetic energies before collision, and so higher electrical fields favor excitation, ignition but also temperature development.
- Light charged particles like electrons are accelerated particularly strong. As a result, until temperature equilibration, the electron temperature $T_\mathrm{e}$ will lie significantly above the bulk gas temperature $T_\mathrm{gas}$.
- A longer interaction time with the electrical field leads to more heavy particles of high kinetic energy and hence a higher gas temperature $T_\mathrm{gas}$.
- Higher pressures and density lead to more collisions in the discharge volume, shorter mean free paths and so it is harder for the particles to accumulate the required ionization energies. At the same time, higher pressure leads to faster equilibration of the temperature $T_\mathrm{gas}$.

The above description is sparse regarding the chemistry involved. Notice, for example, that the negative and positive ion chemistry is qualitatively different, as the light electrons are all negatively charged. The non-equilibrium character of many plasma systems necessitates the knowledge of numerical data such as electron cross sections of physical processes. Unfortunately, these often can only indirectly be obtained via experiments designed to determine values for drift velocity, diffusion coefficients and discharge breakdown characteristics such as the Townsend coefficients [15, 39].

# 2 Discharge kinetics theory

We now get to the subject of detailed statistical mechanics. The basics of equilibrium kinetics is laid out and contrasted to the non-equilibrium situation, thereby showing how the Arrhenius rate coefficients arise. This paves the way to the Boltzmann equation, governing the plasma dynamics. Finally, an outline of its software implementation for the relevant models is provided.

## 2.1 The interaction cross section

Microscopic cross sections are the key ingredient for reaction rates and are experimentally obtained by molecular beam methods. Consider a beam of particles of sort $A$ approaching particles of sort $B$ with relative velocity $g$. The number of particles of sort $A$ scattered from the volume $\Delta V$ should be proportional to $\Delta V$ and the concentrations $n_A$ and $n_B$:

$$\Delta N_A \propto -n_A\, n_B\, \Delta V.$$

Inspecting the units, we see that the missing factor must be a volume. The characteristic interaction length in beam direction is $g\,\Delta t$ and so this gives rise to the implicit definition of the effective cross section of interaction. The proper infinitesimal definition of the *interaction cross section* $\sigma_{AB}(g)$ is now given in terms of infinitesimal time steps:

$$\mathrm{d}N_A := -n_A\, n_B\, (\sigma_{AB}(g)\, g\, \mathrm{d}t)\, \Delta V. \tag{1}$$

A thorough derivation is presented in Smiths monograph [85]. In the following, we will drop excessive indexing, if dispensable.

The general concept of "cross section" comes in many flavors in the literature and for this purpose we try to summarize some of its incarnations. Firstly, the derivation of such a cross section from a more fundamental theory involves computing averages for interactions which might depend on factors such as interaction distance, relative velocity and so on.
It is worth noting that collisions of two particles are often reduced from three down to two dimensions. In computing a cross section from a microscopical theory, the spatial impact parameter is integrated out, so that one is left with a function of velocity. Thus, in many cases, the cross section is only a function of speed and hence of energy. We will consider many types $i$ of interactions in a system and denote their respective cross section by $\sigma_i(g)$. This quantity may moreover be partitioned with respect to a parameter $z$, or several of those, which in turn gives us new cross sections $\sigma_i(g, z)$. For example, we will consider partitions of a species A into different states, i.e. quantum numbers $n$, which occur according to a distribution $f_n$. If $\sigma_{m|n}(g)$ is the cross section for the transition of $\mathrm{A}_n \to \mathrm{A}_m$, then the overall cross section is the sum over the end states $m$ of the $n$-averaged contributions

$$\sigma(g) = \sum_m \left( \sum_n \sigma_{m|n}(g) \cdot f_n \right).$$

Another prominent example of this concept is implicitly given via

$$\sigma(g) = \int_0^{2\pi} \int_0^{\pi} \frac{\mathrm{d}\sigma}{\mathrm{d}\Omega}(g, \Theta, \Phi) \cdot \sin(\Theta)\, \mathrm{d}\Theta\, \mathrm{d}\Phi.$$

The so-called *differential cross section* $\frac{\mathrm{d}\sigma}{\mathrm{d}\Omega}$ distinguishes between different spatial spherical angles $\Theta, \Phi$, with respect to which the process can be investigated. The main axis of the coordinate system is chosen to lie parallel to the vector of collision.

A comprehensive list of cross section models is presented in the reference works by Chernyi et al. [20, 21], as well as the recent topical textbook by Capitelli et al. [16].

## 2.2 The reaction rate coefficient

We can use the above concept of the cross section $\sigma$ to make a series of simple definitions. Firstly, the *reaction rate* is defined as the change of concentration in time,

$$r_A := \dot{n}_A.$$

Definition (1) implies $r_A = -(\sigma(g)\, g)\, n_B\, n_A$. But a scenario with a cluster of particles of single fixed velocity $g$ is not feasible. Taking a second look at the concentration rate equation, we are lead to consider the average of the expression $\sigma(v)\, v$ over all velocities in the system. This is the *detailed reaction rate coefficient*

$$k := \langle \sigma(v)\, v \rangle. \tag{2}$$

The velocity distribution required for the averaging is the topic of the next subsection. With the reaction rate coefficient at hand, a macroscopic reaction is described by

$$\dot{n}_A = -k\, n_B\, n_A.$$

This is the general form of a bimolecular differential equation solved in chemical kinetics theory. After summation over contributions from all possible collision partners, one obtains the system of equations

$$\dot{n}_A = \sum_B k_{AB} \prod_C n_C^{j_{BC}}, \tag{3}$$

where $j_{BC}$ denotes an exponent. Reactions which take place without another reaction partner are called unimolecular reactions, and their kinetic equations are of the form $\dot{n}_A = -k\, n_A$. This means that most exponents are set to zero in formula (3). In that case, $k$ is a frequency and alternatively denoted by $\nu$.

## 2.3 The Boltzmann equation

For a given species, a major concept in the kinetic theory of gases is the *total distribution function* $\mathfrak{F}(x, v, t)$, where $x$ and $v$ now denote vectorial position and velocity. The *particle concentration*, the *particle number* and the normalized *one-particle distribution function* are then respectively given as

$$n(x,t) := \int \mathfrak{F}(x,v,t)\, \mathrm{d}^3 v, \qquad N(t) := \int n(x,t)\, \mathrm{d}^3 x, \qquad f(x,v,t) := \mathfrak{F}(x,v,t)/N(t).$$

The *expectation value* with respect to velocity for a quantity $X$ is then given as

$$\langle X \rangle := \int X \cdot f \, \mathrm{d}^3 v. \tag{4}$$

For example, we have the *mean particle velocity* $\langle v \rangle$ and the *mean kinetic energy* $\langle \frac{m}{2} v^2 \rangle$. If $f$ describes electrons in a conductor, the former is generally called the *electron drift velocity* $v_{\mathrm{dr}}$. It is also worth noting that the approximation $\langle \sigma(v) \rangle \langle v \rangle$ is sometimes used to estimate the rate coefficients $k := \langle \sigma(v)\, v \rangle$. The integro-differential equation governing the evolution of the particle velocity distribution $f$ is the famous *Boltzmann equation*. Roughly, as far as its time evolution is concerned, the equation tells us that

$$\frac{\partial}{\partial t} f(t,v) = -\nu[f] \cdot f(t,v) \; + \ldots \qquad \text{with} \qquad \nu[f] := \int \int |v - w| \, \frac{\mathrm{d}\sigma}{\mathrm{d}\Omega}(w) \, f(t,w) \, \mathrm{d}\Omega \, \mathrm{d}w.$$

Here, we encounter the differential cross section again. The equation bears similarities with an unimolecular rate equation for $f$, but what makes it much more complicated is that the solution $f$ itself determines the rate $\nu$. This is already non-linear in a computationally really unpractical way. Even worse, the remaining term of the right hand side (not shown) involves an integral over a product of two instances of $f$. It describes a self-interaction capturing velocity redistributions, bounded by energy and momentum conservation. All common computer implementations significantly simplify the equation, as we will do in the next section. Let $i$ be the index of the $i^{\mathrm{th}}$ species with masses $m_i$, let $\mathcal{I}_{ij}(g, \Omega)$ encode those interaction cross sections and consider particles in an external force field $F$. In its complete form, the Boltzmann equation is given by

$$\frac{\partial f_i}{\partial t} + \sum_{k=1}^{3} v^k \frac{\partial f_i}{\partial x^k} + \sum_{k=1}^{3} \frac{F^k}{m_i} \frac{\partial f_i}{\partial v^k} = \sum_j \int g \, \mathcal{I}_{ij}(g, \Omega) \left( f_i' \cdot f_j' - f_i(x,v,t) \cdot f_j(x, v_1, t) \right) \mathrm{d}\Omega \, \mathrm{d}^3 v_1,$$

where $g$ is the initial velocity relative to the integrand and $f_i' \cdot f_j' := f_i(x, v'(v, v_1), t) \cdot f_j(x, v_1'(v, v_1), t)$. The heuristic derivation of this equation is presented in many textbooks and we will not repeat it here, nor will we elaborate on its formal derivation from the phase space postulates of statistical physics. For a more detailed discussion, we refer to the well known classical textbook by Hirschfelder et al. [37]. It is noteworthy to mention that there are simplification schemes, which completely integrate out the velocity-dependence. In this case, one ends up with a straight forward approximation for the species evolution of the form $\dot{n}(t) = -\nu \, n(t) + C$, where $C$ denotes a small correction to the linear differential equation. For a historical account on the development of electron physical notions, as well as a more detailed physical explanation, we refer to the textbook by Huxley [39].

Let us consider the limiting case of local equilibrium scenarios, which leads into the realm of conventional chemistry. It turns out that for the stationary case, Boltzmann's theory implies

$$\frac{\partial}{\partial t} f(t,v) \stackrel{!}{=} 0 \quad \Longrightarrow \quad f(t,v) = A \, \mathrm{e}^{-\varepsilon(v) \cdot B},$$

where $\varepsilon(v) = \frac{m}{2} v^2$ and $A, B$ are constants. The latter depend on the system volume, total number of particles, and so, in the equilibrium case, eventually on the temperature $T$. This simple time independent function $f(v) \propto \mathrm{e}^{-\varepsilon(v)/(k_B T)}$ , where $k_B$ is Boltzmann's constant,

is known as *Maxwell-Boltzmann distribution*. Computing expectation values defined by the integral (4) always requires knowledge of a distribution function $f$. In particular, the reaction rate coefficients defined in formula (2), $k := \langle \sigma(v)\, v \rangle$, depend on it. A case where the integral can easily be performed is the hard-sphere model of gases, which assumes that the collision cross sections $\sigma$ only depend on the radii of the particles. Without going into great detail, for the equilibrium case one can use the mathematical relation

$$\int_\epsilon^\infty \mathrm{e}^{-\varepsilon/k_B T}\, \varepsilon^{n-1}\, \mathrm{d}\varepsilon \;\propto\; T^n\, \mathrm{e}^{-\epsilon/k_B T} + \mathcal{O}(T^{n-1}),$$

and finally obtain expressions of the form $k(T) = A(T)\, \mathrm{e}^{-\epsilon/(k_B T)}$, where now $\epsilon$ is a characteristic threshold energy. These so-called *Arrhenius rate coefficients* are the principal data for describing rates in equilibrium chemistry. In the simulation we are going to perform, processes involving electrons in the presence of an electrical field $E$ do not obey the Boltzmann distribution. In that case, the corresponding rate coefficients can not be characterized in this time-independent way.

## 2.4 The electron energy distribution function

Consider a gas containing neutral particles, ions and electrons with charges $\mathfrak{q}$ in an area with an external force field $F = -\mathfrak{q}\, E$, determined by an electrical field $E$. Electrons are charged particles of small mass, meaning they receive kinetic energy quickly and then transmit it relatively fast among each other. Thus, one often has a situation in which the electrons are in non-equilibrium and the heavy particles can be considered to be Maxwellian, meaning we only need to solve the time-dependent Boltzmann equation for the electrons. As this can not generally be done for the full set of interdependencies, one often passes on to a simpler description. For a situation with a vector field $E$ which doesn't change its direction, a relevant quantity is the angle $\theta$ between the *electron drift velocity vector* $v_{\mathrm{dr}}$ and the field. In the so-called two-term approximation, one then expands $f$ in trigonometric functions of $\theta$ and drops all but the first two terms

$$f(v) \approx f_0(v) + \cos(\theta)\, f_1(v),$$

see Pitchford et al. [8] for the standard computer implementation and Capitelli [15] for more theory. Here, spherical coordinates in velocity space were adopted so that less significant angle dependencies can be integrated out. Furthermore, in an intricate series of computations, the function $f_1$ can be eliminated in favor of $f_0$ by invoking the Boltzmann equation and taking averages over time [77]. One generally expresses the resulting differential equations in terms of the mean kinetic energy $\varepsilon(v)$, with $\mathrm{d}\varepsilon = m\, v\, \mathrm{d}v$ and $v \frac{\partial}{\partial v} = 2\, \varepsilon \frac{\partial}{\partial \varepsilon}$. The *electron energy distribution function* (EEDF) $f(\varepsilon)$ is implicitly introduced in $\sqrt{\varepsilon} f(\varepsilon)\, \mathrm{d}\varepsilon \stackrel{!}{=} 4\pi\, v^2 f_0(v)\, \mathrm{d}v$. The electron energy distribution function is commonly abbreviated as "EEDF" and it satisfies the equation

$$\sqrt{\varepsilon} \frac{\partial}{\partial t} f(\varepsilon) + \frac{\partial}{\partial \varepsilon} \mathcal{J}[f] = n \sum_i \mathcal{Q}_i[f], \quad \text{with} \quad \mathcal{J}[f] \approx -n\, \frac{1}{3} \frac{1}{\sqrt{2 m_{\mathfrak{q}}}} \left( \frac{\mathfrak{q}\, E}{n} \right)^2 \frac{1}{\sum_k \mathrm{x}_k\, \sigma_k} \cdot \varepsilon \frac{\partial}{\partial \varepsilon} f(\varepsilon).$$

Here $\mathrm{x}_k$ is the mole fraction of the $k^{th}$ species and $\mathcal{Q}_i[f]$ capture different types of collision integrals. Note that the so-called *reduced electrical field* $E/n$ is the quantity that determines the behavior, and not $E$ alone.

## 2.5 Macroscopic observables from microscopic physics

The definitions in the upper half of table 1 are of crucial importance in the discussion of the EEDF and the response of a gas in presence of an applied voltage in the discharge gap. Here $\mathfrak{q}_{\mathrm{e}^-}$ is the electron charge, see table 37. The microscopic power $\mathcal{P}$ is also known as *Joule heating*. Further relevant quantities are the power density $\mathcal{P}\,[\mathrm{e}^-] = j\,E$ and the input energy density $\int_0^\tau j\,E\,\mathrm{d}t$ corresponding to a time $\tau$.

Let $\mathrm{x}_j$ denote the mole fraction for a species $j$ and let $\epsilon_{ij}$ be the threshold energy for the process $i$ with associated rate coefficient $k_{ij}$. The product of $\epsilon_{ij}$ with $k_{ij}\,\mathrm{x}_j\,n$ is a characteristic energy transfer rate and so the so-called *eta-factor*

$$\eta_{ij} := \frac{\epsilon_{ij}\cdot k_{ij}\,\mathrm{x}_j\,n}{\mathcal{P}} = \frac{\epsilon_{ij}\,k_{ij}}{v_{\mathrm{dr}}\,\mathfrak{q}_{\mathrm{e}^-}(E/n)}\,\mathrm{x}_j$$

captures the distribution of electrical power transferred into the gas. The energy transported in an elastic process between electrons and a species of mass $M_j$ is $2\,\frac{m_{\mathrm{e}^-}}{M_j}\langle\varepsilon\rangle$ and leads to a relaxation between electron temperature $T_{\mathrm{e}}$ and gas temperature $T$.

Assume that the total current density $j$ is predominantly determined by a single species, namely the electrons. Recall that those have small mass and are therefore accelerated more easily than the heavy positively charged molecules. Consider now a discharge of volume $V = d\,A$, where $d$ and $A$ denote the discharge gap and cross section $A$, respectively. The resistance of a resistor should be higher if the discharge is longer, and smaller if it is broader. As a first order approximation (i.e. for time independent electrical fields), the work per charge of a particle passing through a field is given by $\int E\,dx$.

Hence we make identifications presented in the lower half of table 1. Multiplying the equations $\mu\,E = v_{\mathrm{dr}}$ and $[\mathrm{e}^-]\,\mathcal{P} = j\,E$ by $d\,\varrho/\sigma_{\mathrm{e}^-}$ resp. $V$ tells us that

$$U = R\,I \qquad \text{and} \qquad P = U\,I.$$

| **Electrodynamical quantity** | **Name** |
|---|---|
| $\varrho := \mathfrak{q}_{\mathrm{e}^-}[\mathrm{e}^-]$ | charge density |
| $j := \varrho\,v_{\mathrm{dr}} = \mathfrak{q}_{\mathrm{e}^-}[\mathrm{e}^-]\,v_{\mathrm{dr}}$ | current density |
| $\mathcal{P} := F\,v_{\mathrm{dr}} = \mathfrak{q}_{\mathrm{e}^-}E\,v_{\mathrm{dr}}$ | microscopic power |
| $\mu\,E := v_{\mathrm{dr}}$ | mobility |
| $\sigma_{\mathrm{e}^-} := \varrho\,\mu = j/E$ | conductivity |
| $\rho := 1/\sigma_{\mathrm{e}^-}$ | resistivity |
| $P := [\mathrm{e}^-]\,V\,\mathcal{P}$ | electrical power |
| $I := j\,A$ | electrical current |
| $R := \rho\,d/A$ | electrical resistance |
| $U := E\,d$ | electrical voltage |

Table 1: Crucial definitions in the computer implementation of plasma physics.

## 2.6 Discharge behavior of the constant current model

To understand the workings of the *Chemical Workbench* implementation of the Boltzmann equation, it is valuable to emphasize the following chain of dependencies, valid at a fixed time $t_0$:

- Given: cross sections $\sigma(\varepsilon)$, $E$ and $[\mathrm{A}_j]$ at time $t_0$.
  $\Longrightarrow$ $f(\varepsilon, t_0)$ ... via Boltzmann equation.
- Computing: $v_{dr} := \langle v \rangle$.
  $\Longrightarrow$ $\mu = \langle v \rangle / E$
  $\Longrightarrow$ $j = \mathfrak{q}_{\mathrm{e}^-} [\mathrm{e}^-] \langle v \rangle$.
- Computing: $k := \langle \sigma(v)\, v \rangle$.
  $\Longrightarrow$ $[\mathrm{A}_j]$ at new time $t_0 + \Delta t$ ... via chemical kinetics.

The electrical field $E(t)$ is a quantity which is generally hard to measure. However, if the true current density $j(t)$ is known, then the Boltzmann equation can be solved self-consistently using the condition presented in the second bullet point above.

We are mainly interested in electrical currents which are approximately constant. This is because in the discharge setup which will concern us later, the current $I = \mathfrak{q}_{\mathrm{e}^-} [\mathrm{e}^-]\, \mu\, E\, A \propto [\mathrm{e}^-]\, E$ is continuously regulated. The mobility doesn't vary much, thereby coupling the field to the electron velocity. In this case, the electron dynamics of the simulation follow a simple pattern: As the electron concentration $[\mathrm{e}^-]$ goes up due to ionization processes, the electrical field $E$ goes down. Physically, this is because a higher charge transfer lowers the potential $U = E\, d$.

The "constant current module" of the *Chemical Workbench* software package operates by iteratively computing the EEDF from a small user defined initial electron seed of less than $10^{-10}\,\mathrm{cm}^{-3}$. This concentration $[\mathrm{e}^-]$ will then go up (and so $E$ goes down), until it reaches it's stable physical value within a few hundred nanoseconds. The obtained electrical field values, velocities and mean electron energies are very stable with respect to a variation of the initial seed and even with respect to the value of the fixed current density. The time span that follows may be called the "chemical regime". A simulation with a higher $j$-value, corresponding to a higher resulting electron concentration, leads to a higher molecular input power density $\mathcal{P}\,[\mathrm{e}^-] = j\, E$ into the gas, which is usually expressed as characteristic energy in eV per molecule and second.

# 3 Chemical species generated in oxygen-helium discharges

We are concerned with atmospheric pressure, low- to medium temperature alternating current $O_2$/He-microdischarges. In the present section, we discuss the characteristics of chemical species, in that they are crucial to the understanding of the plasma-chemical reaction mechanisms developed here. The candidates to be considered for the reaction mechanisms are:

- Ground state particles: $O_2, O, O_3, He$
- Electronically excited molecular oxygen: $O_2(a^1\Delta_g), O_2(b^1\Sigma_g^+), \ldots$
- Electronically excited atomic oxygen: $O(^1D), O(^1S), \ldots$
- Furthermore: $O_2(r)$, $O_2(v), He^*, He_2^*, He(met)$
- Charged particles: $O^+, O_2^+, O_4^+, O^-, O_2^-, O_3^-, O_4^-, He^+, He_2^+$

Here, the species in the fourth line do not denote particular states but auxiliary particles. For example, $He^*$ denotes several energetically similar helium states lumped together. The same holds for rotationally or vibrationally excited oxygen states $O_2(r)$ and $O_2(v)$. Due to the spatial separation of discharge and flame zone, we need not to be concerned with so-called ionic oxidation formation, in which charged species such as $OH^-$ participate. As a result, the charged particle chemistry remains fairly simple, at least relatively speaking, and it won't be in the focus of this work. In discharges with field strengths in the order of $10^1$ Td to $10^2$ Td, $O^-$ and $O_2^+$ are produced in higher quantities than other charged oxygen particles [96]. The relevance of processes involving large charged clusters such as $O_4^+$ is determined by the time scales of the charged particle recombination vs. the cluster formation processes.

## 3.1 Energy hierarchy of electron-oxygen collision processes

Our main focus is on molecular oxygen with its many facets. The full formula for its ground state is $O_2(X^3\Sigma_g^-)$. The first character in the bracket denotes the main quantum number, which for ground states is generally written as "$X$". Higher levels are denoted by upper or lower case latin letters. The "3" means that it is a triplet state and this rare feature of oxygen is responsible for many of oxygen's distinguishing characteristics, for example non-zero paramagneticity. Unpaired spins in $O_2$'s ground state give a permanent magnetic moment. The character in the position that follows, $\Sigma$, denotes the lowest electronic state. Higher states are denoted, by $\Pi, \Delta, \Phi, \Gamma, \ldots$. The symbol's numerical exponent relates to the particles spin and "$-$" (or "$+$") and "$g$" (or "$u$") denote reflection symmetry and parity, respectively. Molecular oxygen is a diatomic molecule and so its internal potential energy depends on the intermolecular distance. Apart from the main and electronic number, one also distinguishes between vibrational levels. The molecule has an atomic weight of 32 and six outer electrons. A more in depth explanation of its structure can be found in [35, 51].

| **Products** A | [eV] |
|---|---|
| $O_2(v=1)$ | 0.19 |
| $O_2(v=2)$ | 0.38 |
| $O_2(v=3)$ | 0.57 |
| $O_2(v=4)$ | 0.75 |

| **Products** A | [eV] |
|---|---|
| $O_2(a^1\Delta_g)$ | 0.98 |
| $O_2(b^1\Sigma_g^+)$ | 1.63 |
| $O_2(4.5)$ | 4.50 |
| $O_2(6)$ | 6.00 |

| **Products** A + B | [eV] |
|---|---|
| $O(^3P) + O(^3P)$ | 6.12 |
| $O(^3P) + O(^1D)$ | 8.40 |
| $O(^1D) + O(^1D)$ | 9.97 |
| $O_2^+ + e^-$ | 12.06 |

Table 2: Possible products of the electron impact process, sorted by electron energy.

We now consider collisions of the form

$$O_2(X^3\Sigma_g^-) + e^- \rightarrow A + e^-$$

and

$$O_2(X^3\Sigma_g^-) + e^- \rightarrow A + B + e^-,$$

in which electrons transfer energy to oxygen. In the simplest case, this manifests in excitation of translational degrees of freedom of oxygen, i.e. direct gas heating, but the chemical state of $O_2(X^3\Sigma_g^-)$ may also be affected. Experimentally, the cross section data for many major species such as A = $O_2(b^1\Sigma_g^+)$ was first extensively investigated by Phelps et al. and the resulting data is the basis of the implementation of many Boltzmann solvers. The online library of the *LXCat project* provides a major resource [53]. Table 2 is a selection of possible products A, B together with the electron energy associate with the process, as implemented in the small reaction mechanism found in [13]. It does not include very low and very high energy states.

The symbol $O(^3P)$ is the detailed name of atomic oxygen in its ground state, i.e. O. Its first two electronically excited atomic oxygen states are called $O(^1D)$ and then $O(^1S)$, see [38] for details. In the literature, the states $O_2(a^1\Delta_g)$ and $O(^1D)$ are sometimes denoted by the symbols $O_2^*$ and $O^*$, but other times these are the names of auxiliary particles, representing several states of similar energy at once. In [105], the symbol $O_2^*$ represents the sum of the high electronically excited so-called Herzberg states $O_2(A^3\Sigma_u^+)$, $O_2(A'^3\Delta_u)$ and $O_2(c^1\Sigma_u^-)$, which are characterized by similar energies up to about 4.5 eV, see table 3. In this work, $O_2^*$ denotes any electronically excited oxygen molecule and the sum of the three higher states is written as $O_2(4.5)$, as is done, for example, in [103]. Oxygen excitation and bond-dissociation energies will later be discussed in more detail. In any case, states higher than $O_2(b^1\Sigma_g^+)$ or $O(^1S)$ are energetically hard to generate and thus of less significance for the discharge behavior of our interest. The costly ionization of the gas becomes the dominant process for electron energies above 10 eV.

## 3.2 Rotationally and vibrationally excited states

Rotational states, with energies significantly lower than chemical reaction thresholds (e.g. 0.02 eV) will generally affect plasma assisted combustion via incremental gas heating. At least when compared to electronic excitation, vibrational and translational temperature equilibrate fast as well. Those of course always depend on the mixture composition, being generally higher for heavier particles (e.g. $\approx 0.5$ ns for $O_2$ and $N_2$ $R$-$T$ relaxation in air). As

explained in more detail below, figure 3 demonstrates the declining importance of those vibrational species, when discharge is tuned to produce many $O_2(a^1\Delta_g)$ and $O_2(b^1\Sigma_g^+)$ particles. At higher electrical field strengths, the energy fraction distributed towards the low vibrational level can be completely neglected. In the mechanism below they are represented by a joint particle, $O_2(v)$, and the same holds for $O_2(r)$, capturing rotational oxygen excitation.

The situation for systems involving nitrogen is slightly different and is worth noting. Here vibrational levels play a more prominent role. Some simulation methods in the literature keep track of $T_{\text{vib}}$ of the individual species vs. time [98]. The referenced review lists several $V$-$T$-relaxation rate coefficients, also including those for $O_2(v=1), H_2(v=1), N_2(v=1)$. In the present overview, we won't discuss reactions involving excited species other than oxygen or helium.

## 3.3 Singlet oxygen states $O_2(a^1\Delta_g)$ and $O_2(b^1\Sigma_g^+)$

The first two excited states of molecular oxygen, which we shortly denote by $O_2(a^1\Delta_g)$ and $O_2(b^1\Sigma_g^+)$, are of special interest. Their systematic investigation goes back to Hans Kautsky in the 30's, see [33,81]. Known to exist since the 20's, they are often called "singlet delta" and "singlet sigma" and differ in how two of the oxygen molecules paired electrons occupy oxygen's molecular orbitals. In oxygen gas mixtures, the two states generally appear together: If one produces $O_2(a^1\Delta_g)$, the molecule $O_2(b^1\Sigma_g^+)$ will also appear in the mixture due to the $E$-$E$ exchange reaction

$$O_2(a^1\Delta_g) + O_2(a^1\Delta_g) \leftrightarrow O_2(b^1\Sigma_g^+) + O_2(X^3\Sigma_g^-)$$

as well as in third body collisional excitations. The significance of the higher state is discussed in "Singlet Sigma: The "Other" Singlet Oxygen in Solution" by Weldon et al. [108]. The amount of energy stored in these molecules, as compared to the ground state formation, is 0.98 eV ($\hat{=}$ 11372 K $\hat{=}$ 7918.1 cm$^{-1}$) and 1.64 eV ($\hat{=}$ 19031 K $\hat{=}$ 13195.1 cm$^{-1}$), respectively. In statistical physics, energies are often expressed in Kelvin, while in spectroscopy, cm$^{-1}$ is used. Here the mediating natural constants are $k_B \approx 8.62 \times 10^{-5}$ eV/K and $hc \approx 1.24 \times 10^{-4}$ eV cm, respectively. For a convenient converter into eight different energy units, see [22, 51] for an in-depth spectroscopic analysis. In terms of chemical kinetics, those energies lead to a reduction of reaction barriers by 22.5 kcal/mol (= 94 kJ/mol) and 36.5 kcal/mol (= 157 kJ/mol).

As is to be expected for the reduction of energy barriers, chemical reactions of excited species generally take place much faster than the equivalent involving the unexcited counterpart. Indeed, the rate coefficients of vibrationally and electronically excited particles can be higher by factors between 100 to 1000 [93]. Values for the first few spectroscopic constants to compute the energies are presented in table 3.

| $O_2$ **state** | $X^3\Sigma_g^-$ | $a^1\Delta_g$ | $b^1\Sigma_g^+$ | $c^1\Sigma_u^-$ | $A'^3\Delta_u$ | $A^3\Sigma_u^+$ | $B^3\Sigma_u^-$ |
|---|---|---|---|---|---|---|---|
| **Energy,** [eV] | 0 | 0.982 | 1.636 | 4.099 | 4.301 | 4.389 | 6.174 |

Table 3: Energies for six electronically excited states of molecular oxygen, [15].

The state $O_2(b^1\Sigma_g^+)$ is naturally produced in the stratosphere by O-recombination and in a secondary reaction of photodissociation of $O_3$ by solar ultraviolet radiation [13]. Man-made devices such as electrical discharges or lasers are used to generate singlet oxygen. In a mixture with non-noble gases, energy stored in excited particles can be transferred and so these durations might be significantly reduced in a mixture for an early suggestion of this idea, see [4] . This ability for energy distribution is the main motivation for the present study.

The de-excitation rates for $O_2(a^1\Delta_g)$ are comparatively small, stalling equilibration. To state a numerical example, the collisional lifetime of $O_2(a^1\Delta_g)$ in a methan-air mixture at atmospheric pressures is $4.2 \times 10^{-2}\,\mathrm{s}$ [93]. On the other hand, the transition from the $b^1\Sigma_g^+$-state to the ground state is "electric-dipole-forbidden" and hence rare. Its very long lifetime is about 75 minutes (see [14, 88] ) and it is hence difficult to detect by emission spectroscopy. The emission lines of those two species are at 1268 nm and 762 nm, respectively. Their radiative lifetime is $\approx 3900\,\mathrm{s} = 65\,\mathrm{min}$ and $\approx 14\,\mathrm{s}$, respectively [93]. But of course, in mixtures the rate is much lower. The transition $O_2(b^1\Sigma_g^+ \rightarrow a^1\Delta_g)$ is spin-allowed and of relatively high rate, as will be thoroughly discussed in the section on oxygen reaction mechanisms.

## 3.4 Atomic oxygen and ozone

The need to keep track of the ground state particles $O(^3P)$ is clearly unavoidable in discharges, where the electrons reach the oxygen dissociation energy of 5.15 eV. Note that this value lies well above the amount required for electronical excitation. While higher concentrations of atomic oxygen generally advance the combustion process, this reactive radical is often undesirable in real applications. For our cases, it must also be considered a quencher of excited oxygen.

Given $O_2$ and O, production of $O_3$ is also immanent. From all the oxygen-plasma products, ozone has the longest lifetime and can hence be considered to be a carrier of atomic oxygen. Ombrello et al. investigate ozone and discuss its role as quencher of excited species [64]. Not only do higher power densities and temperatures lead to dissociation of ozone, but ozone's production rates also tend to decrease with higher temperatures. This aspect makes higher energy systems favorable for singlet oxygen production. Moreover, as discussed above, higher power also leads to higher electron concentrations, which favor electron impact excitation.

## 3.5 Charged species and attachment/detachment

As has been explained in section 2.6, if the current $I = q_e\,[\mathrm{e}^-]\,\mu\,E\,A$ in a discharge gap is fixed, then the electrical field correlates inversely with the electron concentration. Hence, electron attachment $A + \mathrm{e}^- \rightarrow A^-$ leads to a rise in the field $E$. The chemical configuration of $O_2$ makes it prone to attract and absorb electrons and negative ions. The global processes at work are

$$\mathrm{O_2} + \mathrm{e}^- \rightarrow \mathrm{O_2^-} \qquad \text{and} \qquad \mathrm{O_2} + \mathrm{O_2^-} \rightarrow \mathrm{O_4^-}.$$

For any given applied voltage $U$, removal of light species (electrons $e^-$, resp. negative oxygen ions $O_2^-$) in favor of heavier reactants lead to a reduction of mean particle speed and hence a smaller electrical current $U/R = I \propto [e^-]$. Therefore, compared to electronically passive chemicals, molecular oxygen effectively raises the electrical resistance $R$. Consider now a discharge with constant current $I$ and observe that

$$E \approx \frac{U}{d} = \frac{R \cdot I}{d} \propto R.$$

Effectively, an oxygen discharge will raise the electrical field $E$ to balance the force that would lower the current. A stronger field, i.e. a higher energy, leads to new ionizations and hence more charges and different excitation levels are sensitive to different electrical field values. Moreover, note that this loss of electrons when adding more electronegative species to the system can result in a lowering of the dissociation rates $AB + e^- \rightarrow A + B + e^-$. In this way, raising the mole fraction of $O_2$ in an oxidizer (while keeping the electrical power input constant) can actually lower the O production. Detachment processes such as $O_2^- + A \rightarrow O_2 + A + e^-$ affect the discharge in the analogous fashion. We see that molecular oxygen has a significant non-linear effect on discharge systems. By the above reasoning, an increased initial $O_2\%$ can also be expected to lead to a higher power consumption [88]. Conversely, increasing power input, even if not necessarily affecting the net resulting electrical field, leads to higher electron concentrations which favors oxygen excitation and dissociation.

Due to the electronegativity of oxygen, $O^-$ and $O_2^-$ are formed relatively easy, compared to other particles and their concentrations sometimes even exceed these of the electrons [15]. Nevertheless, the number of charged particles is typically still smaller than that of excited ones by a factor of tens of thousands or more, e.g. $10^4$ in the recent investigation by Kelly and Turner (see [43, 44] ), which will be described later. As such, it does not influence the chemistry of the fuel-oxygen mixture and does not need to be taken into account in the combustion zone. In fact, as in our case (section 5), such small concentrations often do not survive the plug connecting the discharge and the combustion zone.

## 3.6 Helium

For a fixed reduced electrical field $E/n$, the characteristic energy of the electrons is higher the simpler the bath gas is, i.e. the less it absorbs energy itself. For high electron energies, classical gases considered are $Xe, He, N_2, H_2, CO_2$, see [98]. In the following we describe the properties of He, which is of direct interest to us.

Beyond the inert ground state of helium He, energetically speaking, we find metastable states, which are followed by various excited states, above which ionization occurs. Technically, these are also just excited states. However, for several purposes their relaxation times back to the ground state are long enough for them to be considered stable. This is the same situation that occurs with the excited state $O_2(a^1\Delta_g)$. In a low pressure environment, it can have a very long lifetime (more than an hour). Notable metastable helium states are $^3S_1$ or $^1S_0$, with quantum number $n = 2$. Their spin is different from that of the ground state, so that spontaneous transition is forbidden. In helium gas, there are no energy losses due to rotational or vibrational excitation.

# 4 Before this work

## 4.1 On oxygen plasma generation

Over the last decade, a substantial amount of research on plasma assisted combustion has accumulated. As a rule, this research is either presented from the perspective of establishing the principles behind the plasma chemistry involved, or with the aim of empirically establishing more stable and energy efficient burner systems. The recent paper by Starikovskiy and Aleksandrov on the subject provides an introduction and reports of many successes in the field [98]. In this article, different configurations are demonstrated to operate over a wide variety of equivalence ratios, pressures and flow velocities. See also [97] for an earlier overview by Starikovskiy.

The approach we focus on here is the excitation and subsequent combustion of oxygen gas. Due to the variety and range of parameters such as field strength and frequency, input power, gas composition, pressure, and so on, it is almost impossible to find studies on perfectly comparable independent research projects. The literature to analyze is narrowed down substantially by acknowledging that the following topics are of smaller relevance for the present study:

- Thermal regime / very high energy input,
- The low pressure regime,
- Plasma treated oxygen mixtures involving nitrogen,
- Diverse discharge types (self-sustained, electron beam sustained, etc.),
- Fuel gas inside of the discharge,
- Removal or conversion of particular exhaust species.

Most works inevitably differ in at least one relevant aspect from the experiment in Magdeburg, to be described in section 5 . Nevertheless, many of them provide us with an accurate picture of what to expect. Even articles with no particular focus on combustion technology can be amongst the relevant papers on singlet oxygen generation in discharges. For example, a common research topic (see e.g. [13, 103]) is the production of high energy oxygen species $O_2^*$ to facilitate the generation of oxygen-iodine laser light via

$$O_2^* + I \;\rightarrow\; O_2 + I^* \;\rightarrow\; O_2 + I + h\nu.$$

Continuing the description of the chemical properties of singlet oxygen from the last section, we now start out with a review of results on the feasibility of its generation in discharge systems. This motivates and provides the context for the present project. In this section, kinetic theory itself is not explicitly discussed, i.e. we don't consider individual processes. An in-depth study of the reaction chemistry required for the simulation of such systems is the content of chapter II, were reaction mechanisms are discussed.

### 4.1.1 Excited oxygen yield

The excited oxygen yield is defined as

$$Y_{O_2^*} := \frac{[O_2^*]}{[O_2] + [O_2^*]},$$

where $O_2^*$ may be a particular excited species, such as $O_2(a^1\Delta_g)$ or $O_2(b^1\Sigma_g^+)$, or several lumped together. Note that the yield is sometimes alternatively defined as $[O_2^*]$ over just $[O_2]$ or over the sum of all possible oxygen molecule species. If we know the energy fraction going into a particular particle excitation, $Y_{O_2^*}$ can be estimated by multiplying said fraction by the ratio of the total input energy over energy required for the excitation. For example, if we have an effective energy delivery of $0.28\,eV$ versus a cost of $0.98\,eV$ for the excitation $O_2(X^3\Sigma_g^- \rightarrow a^1\Delta_g)$ and if at a reduced electrical field of $E/n = 15\,\mathrm{Td}$ the energy fraction going into this state is 10%, then the expected yield is $\frac{1}{10} \cdot \frac{0.28\,\mathrm{eV}}{0.98\,\mathrm{eV}} \approx 0.028$, or about 2.8%. Note, however, that this is an estimate for the discharge zone. Thus, unavoidable quenching at the outlet or population through higher states such as $O_2(b^1\Sigma_g^+ \rightarrow a^1\Delta_g)$ are not taken into account.

We see that energy efficiency is a matter of choosing the appropriate discharge system and one of the most significant parameters determining the translation of electrical power into the desirable chemical channels is the value of $E/n$. Accordingly, Starikovskiy et al. draw the following conclusion [98]: "*The main theoretical issue of plasma chemistry for combustion can be formulated as the question of energy redistribution of the field and accelerated electrons into the internal states of the gas.*"

A typical result of a simulation of the so-called energy loss fractions, for electron collision processes in a mixture containing oxygen and as a function of electrical field strengths $E/n$ applied to an oxygen containing gas, is shown in figure 3. The graph is a quantitative reflection of the fact that production of O and $O^*$ by dissociation processes removes $O_2$ and $O_2^*$ from the mixture, which reduces the possible excited oxygen yield. What is important to note is that the maximum energy fraction going into *electronical* excitation is reached at comparatively weak fields. Usually, these excitations are associated with higher energies and become relevant for fields of 100-500 Td. However, the oxygen state $O_2(a^1\Delta_g)$, being effectively populated for 3-10 Td already, is an exception to this [98]. A field of 11 Td is the commonly considered empirical optimum for $O_2(a^1\Delta_g)$ generation in oxygen plasma, see [90, 93] as well as the $O_2$/He mixture shown in figure 3. The peak is slighly shifted to the left here. This is due to the presence of $O_2(b^1\Sigma_g^+)$, which will quickly transition to lower energy states and thus in fact also contributes to the $O_2(a^1\Delta_g)$ fraction. Since this value lies notably below the typical field strengths required for discharge breakdown, non-self-sustained discharge systems, in which ionization is supported by a secondary source, are often utilized. Note that in this figure, excitations of higher states that may decay into $O_2(a^1\Delta_g)$ must be taken into account, when computer simulations are used to estimate the $O_2(a^1\Delta_g)$ production. Production of short lived particles such as $O_2(4.5)$ is always beneficial.

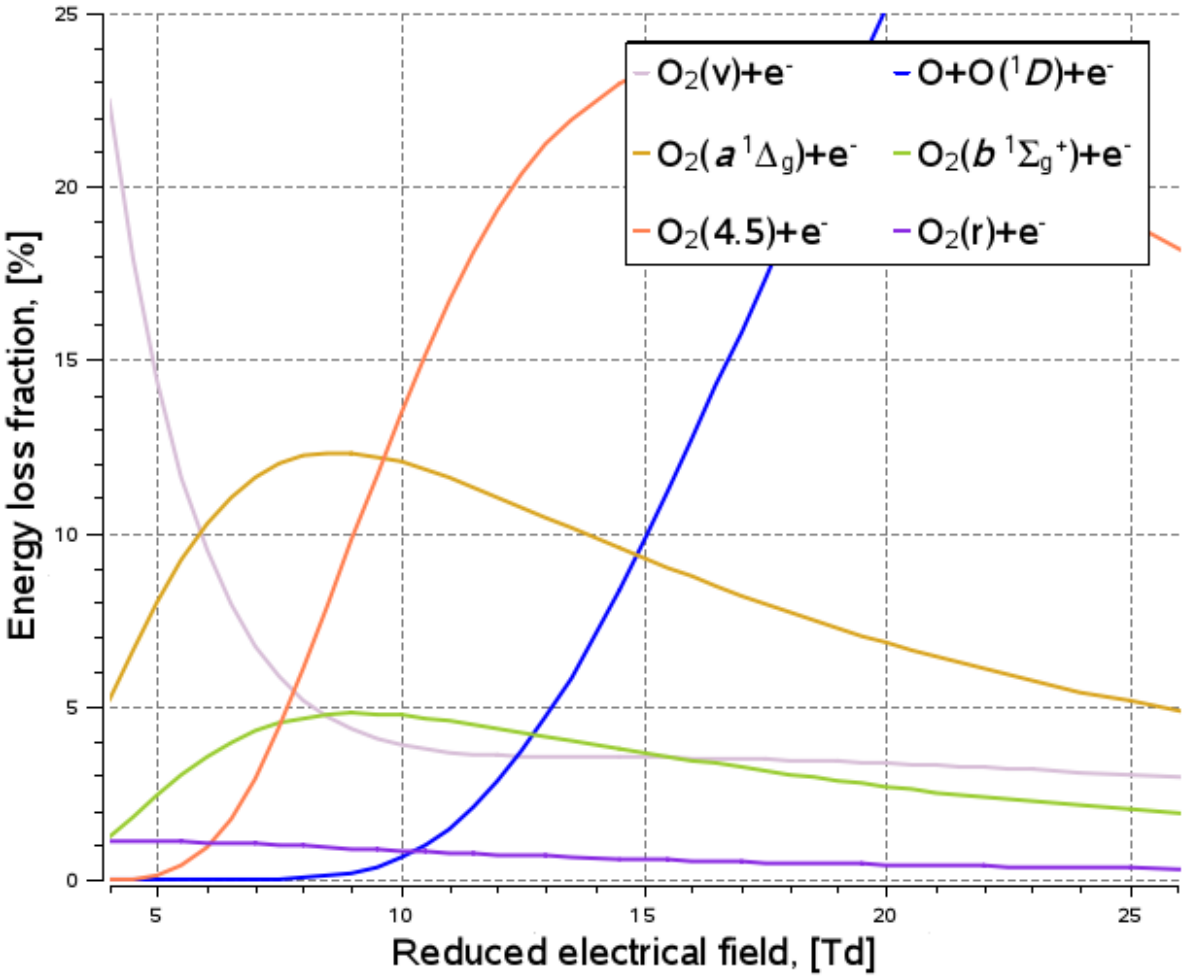


Figure 3: Energy loss fraction for an oxygen-helium mixture ($O_2 : He = 1 : 30$) vs. constant reduced electrical field strengths at one nanosecond - this system is discussed in more detail in subsection 8.6; The dissociation process presented here (dark blue line) must be understood as production of the dissociative intermediate $O_2(B^3\Sigma_u^-)$; The largest electron energy fraction is transferred in elastic collisions with helium in $He + e^- \rightarrow He + e^-$ and is not shown in the graph; The energy fractions for ionization by electron impact, e.g. $O_2 + e^- \rightarrow O_2^+ + e^- + e^-$, are also not shown.

The energy loss fraction depends on the overall gas composition, i.e. dilution of $O_2$, as well as pressure. The possibility to create a suitable field also depends on parameters such as pressure. For low pressures of 1 to 50 Torr self-sustained discharges (no voltage regulation post breakdown) can be used. See Pliavaka et al. [67] for the history of maximal yields at various pressures up to 2006 and [95] for a more recent discussion of the pressure parameter in the context of hydrogen combustion. The state of the art density of singlet oxygen production is $\approx 10^{16}\,\mathrm{cm}^{-3}$ [104]. This concentration in the cited study amounts to a species ratio of $[O_2(a^1\Delta_g)]/n \approx 4 \cdot 10^{-4}$ or 0.4%.

### 4.1.2 On diluents

From the discussion of the interaction between molecular oxygen and the electrical field it is clear that a change in $O_2$ concentration will modulate the discharge behavior, and this can by done be diluting the mixture.

The chemistry of noble gases is relatively simple and affects the gas dynamics mostly indirectly, by redistributing energy in collision processes with oxygen. Both helium and argon have repeatedly been considered for various other parameter settings and the optimal initial $O_2$ fraction seems to never exceed a one-digit percentage. See Vasiljeva et al. [105] for argon and helium experiments at low energy inputs and also Stadler et al. [89] for a study of air in helium, at $p = 1\,\text{bar}$ and $T_{\text{gas}} = 345\,\text{K}$. The energy transfer in fact improves the uniformity of the discharge: Helium has a high thermal conductivity, which can also be used to keep gas temperatures in applications close to room temperatures, stabilizing the system and reducing the minimal required field $E/n$, [59, 101].

Excitation energy of He to the highest metastable state (19.8 eV) is high compared to that of Ar (11.5 eV). A discussion of the difference between dilution by helium, argon and neon is given in [13]. The result is that Ar absorbs more energy from excited oxygen states than He. Since the oxygen plasma chemistry is so complex, experiments using the dilution technique generally adjust the $O_2$ inflow so as to optimize $O_2(a^1\Delta_g, b^1\Sigma_g^+)$ yield vs. input power.

The reason why nitrogen $N_2$ is not suitable for the type of discharge we are concerned with is its much higher energy loss fraction combined with quenching effect, both of which work against a high $O_2^*$ yield. This is true in the broad range of reduced electrical field values ($4\,\text{Td} - 110\,\text{Td}$, as discussed in the overview by Starikovskiy [98]). For a recent comparison of excitation levels vs. $E/n$, considering $O_2$, $O_2/N_2$- as well as $O_2/CH_4$-mixtures, see [96]. One type of energy loss is through vibrational excitation of $N_2$. It should be noted, however, that reactions of oxygen with excited nitrogen also produce atomic oxygen, possibly in an excited state such as $O(^1D)$, which also enhances combustion. At higher electrical fields ($\geq 20\,\text{Td}$), the energy loss fraction for nitrogen excitation is significant. On the other hand, it is also worth mentioning that some experimenters purposely add small amounts of $NO_2$ to the system. The reaction $NO_2 + O \rightarrow NO + O_2$, in particular, effectively removes atomic oxygen and this is desirable in some studies [14, 42].

### 4.1.3 Validation experiment

The following is an overview of a project on atmospheric pressure $O_2$/He-plasma generation, which in recent years has been performed by the university of Bochum, see [25,26] and [46,47], as well as [61,62,80]. Its goal is the investigation of reactive oxygen species for the purpose of surface modifications and deactivation of bacteria/sterilization. Many of the parameters of this experiment match those of the experiment in Magdeburg (see below), while its usability for computer simulation actually exceeds the latter: The geometry of the discharge zone is very simple and quantitative concentration measurements of atomic oxygen and ozone have been performed. This setup has conseqeuntly also been subject of higher dimensional computer simulations in [34, 43, 44] as well as [107]. It will thus also function as a validation

experiment for our spatially zero dimensional simulation model and aid our mechanism development.

The setup of the project at Bochum University consists of a $O_2$/He-flow in a tube at 950 mbar between two electrodes, operated in a sinodial *AC* mode with 13.54 MHz, see figure 4. The flow direction is from the left to the right in the picture, i.e. orthogonal to the electrodes. The generated plasma has been characterized as a micro-atmospheric pressure plasma jet. Variations of several system parameters have been studied over the years, in particular the flow rate (1 slpm to 4.5 slpm), the gas composition (molecular oxygen admixture in helium of up to 1.6%) the tube length (30 mm or 40 mm) and discharge gap (0.5 mm to 2 mm), as well as the voltage (180 V to 340 V) resp. input power (up to 65 W). It must be noted that the reported power consumption is small compared to the corresponding values of the Magdeburg study (several hundred Watts, see below). The applied voltage and the discharge gap both differ to those of the Magdeburg experiment by a factor of roughly 10, so that the fields $E \approx U_d/d$ are comparable. Possible working conditions for the discharge at a He-flow are discussed and suggested in [47], see figure 5.

The efficiency of power transferred to the gas is estimated to be $\frac{1}{20}$, so that e.g. $12\,W$ of electrical power consumption amounts a maximum of 0.6 W for plasma generation. In Ellerweg et al. [26] it is stated that the power provided for plasma generation is lower than 0.7 W. The following is noted by Waskoenig [107] : *"Only a small fraction of the generator is actually coupled into the connecting cables, matching network and heating of the electrodes, as well as by RF-radiation of the jet device acting as an antenna."*

Figure 6 shows the [O] measurement along the tube for a flow of 4.5 slm He and 27 sccm $O_2$ and at a power of $P_{inp} = 12$ W. For various configurations, results in the range up to $5 \times 10^{15}$ cm$^{-3}$ at the outlet area are typical, figure 5. In one of their early studies, the authors measure [O] at a distance of 3 mm from the effluent for different $O_2$-admixtures and establish a sweet-spot for O generation at 0.6% [25].

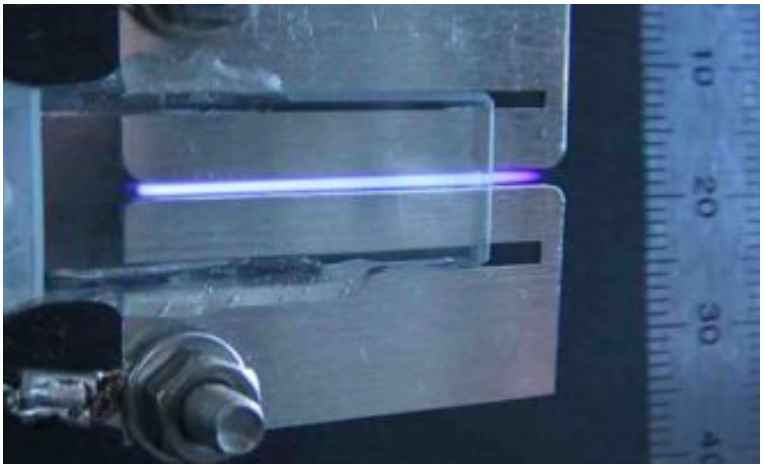


Figure 4: Discharge gap in the experiment performed at Bochum University [34].

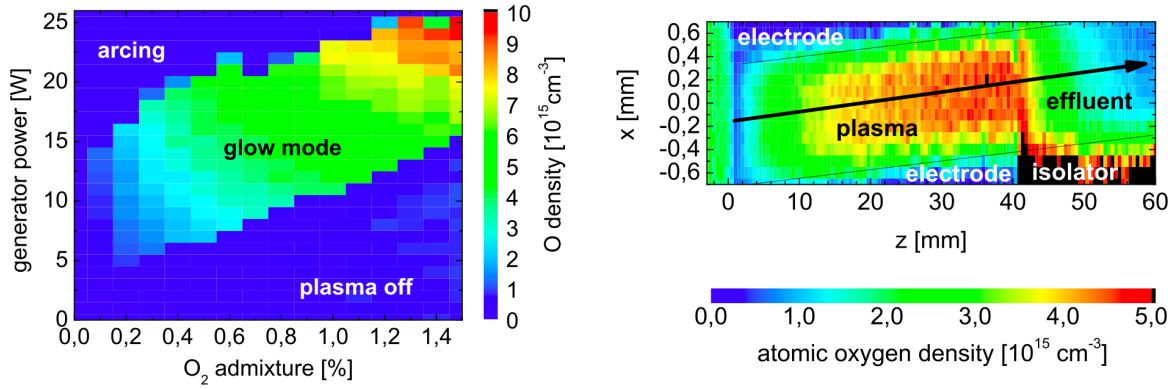


Figure 5: Working conditions without arcing established for the He-flow of 1.5 *slpm* [47].

Temperature field measurements in the discharge and outlet zone have been obtained for certain configurations. In Knake et al. [46], the authors report of a temperature of +14 K to +20 K above room temperature for a position 2 mm in front of the discharge outlet. These values are obtained for a 3 slpm flow at a power input of about 10 W and for $O_2$ admixtures in helium of 0 sccm to 40 sccm. The simulation presented in the follow-up [43], albeit done for a slightly different configuration, agrees well with this value. The accuracy of the TALIF measurement is estimated to be 50% by the authors. And while qualitatively similar, the [O]-results of both measurement techniques quantitatively disagree, as pointed out in [25]: The TALIF concentration results are higher than those of the MBMS measurement, by a factor of 0.27. Finally, the authors report of the seemingly paradoxical effect of [O]-increase with lowering of the flow rate/gas velocity. One would expect [O] to grow as the residence time in the field of the discharge becomes longer. In the paper, the suggested explanation is that for lower flow rates, nitrogen particles from the outside can more easily diffuse into the discharge system and consume atomic oxygen. If this is correct, then the concentration results under-predict the possible production, if compared to a better isolated setup.

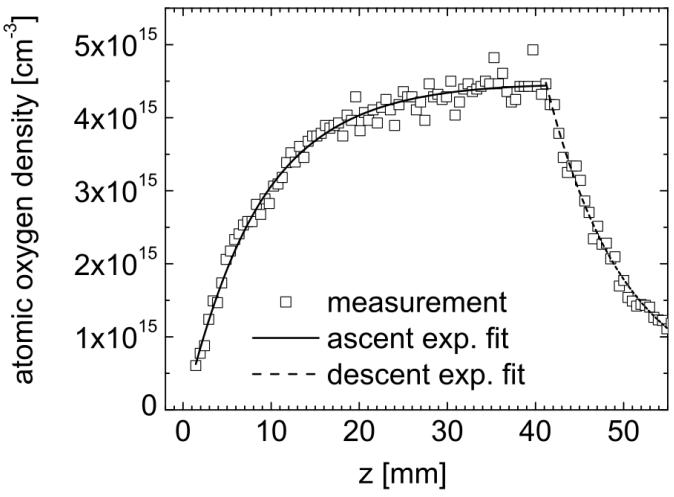


Figure 6: The concentrations of O for 0.6% oxygen in helium, graphic from [47]. [O] has been obtained by TALIF and MBMS measurements, inside the tube as well as at the effluent.

### 4.1.4 Other notable oxygen discharge studies

In this short subsection, we classify a variety of further works on oxygen plasma, which will be of relevance to the discussion of the reaction mechanisms in the second part of the present work.

**Experiments:** The work by Sousa et al. involving an atmospheric $O_2$/He flow manages to produce excited oxygen concentrations that are similar to ones obtained in the experiment performed in Bochum. Values between $10^{15}\,\mathrm{cm}^{-3}$ and $6 \times 10^{15}\,\mathrm{cm}^{-3}$ are achieved, which correspond to yields up to 5%, see [87, 88]. In this case, concentrations are measured at positions in some distance of the discharge. Due to quenching effects, when measured in the afterglow, $[O_2(a^1\Delta_g)]$ strongly depends on the flow velocity. A slow flow leads to more quenching. The "ozone quenching effects"-problem is discussed and it is found that raising initial $O_2$ levels in He is detrimental to the yield. The difference between two different discharge frequencies is discussed.

In "Singlet oxygen production and quenching mechanisms in traveling microwave discharges" [79], Savin et al. discuss $O_2$/He at very low pressures of only a few Torr. Hicks et al. [36] consider a fast $O_2$/He flow at lower pressures ($p = 120\,\mathrm{Torr}$ at Mach number $M = 0.1 - 0.2$). The $O_2(a^1\Delta_g)$ stream is stable up to 15 cm in the afterglow, i.e. at least for several milliseconds.

**Kinetics:** The second chapter of this thesis is concerned with an investigation of the details of plasma reaction mechanisms involving oxygen and helium. We will compare possible temperature dependent reaction rates, but not discuss electron collision cross section data. The discussion is performed by an analysis on an excited oxygen mechanism by Chernysheva et al. [18], which encompasses 162 processes with oxygen particles, 47 of which are non-equilibrium processes. The scheme was established for low pressure systems, but will be considered in a form extended by over twenty reactions to account for the physics and chemistry of helium diluents, that quickly mediate energy through the plasma (see next subsection). Among others, the result is compared against the $O_2$/He-mechanism proposed in Waskoenig et al. [107], which neglects $O_2(a^1\Delta_g, b^1\Sigma_g^+)$. The above two mechanisms are of interest to us in that they focus on the helium-oxygen interactions and the $O_2(b^1\Sigma_g^+)$ chemistry, respectively.

The following articles by several research teams present and study different plasma mechanisms for a variety of applications. The series of experiments around the year 2004 by Vasiljeva et al. have been mentioned above. Their paper [105] contains a scheme of 72 processes for modeling excited oxygen excitation in non-equilibrium plasmas, 13 of which describing interactions of oxygen- and argon species. A related study on RF-discharges with a special focus on the second oxygen molecule state $O_2(b^1\Sigma_g^+)$ is presented by Kovalev et al. [49]. Stafford et al. discuss a full kinetic scheme for $O_2$/He mixtures at low pressures in [90]. This text is followed up in [1, 91]. The work by Stadler et al. [89] contains a mechanism for oxygen, plasma and hydrocarbons in a discharge. A team of researchers including Vagin, Ionin, Napartovich et al. published oxygen plasma mechanisms with electronically excited species, for example in [41, 103].

As has been pointed out many works on singlet delta oxygen in the literature concern a context with oxygen in the presence of nitrogen. However, this does not mean that those texts may not also contain crucial data of interest to us. The book "Plasma Kinetics in Atmospheric Gases" by Capitelli et al. [15] is a thorough textbook that focuses on theory and contains many reaction rates for mechanisms of air-plasma. Here, the Italian author is working in cooperation with Russian scientists, and there are other prominent Russians one often encounters in plasma kinetics theory.

Popov formulated a well known $O_2/H_2$ scheme for the discharge zone [74], although the mechanism comprises many reactions only involving charged fuel species. Next to atoms $O(^3P)$, $O(^1D)$, $O(^1S)$, $H_2(^2S)$ and $N(^4S)$, $N(^2D)$, $N(^2P)$, $H(^2S)$ and molecules $O_2(a^1\Delta_g)$, $O_2(b^1\Sigma_g^+)$, $H_2(a^3\Sigma_g^+)$, $H_2(b^3\Sigma_u^+, c^3\Pi_u, e^3\Sigma_u^+)$ and $N_2(A^3\Sigma_u^+)$, $N_2(B^3\Pi_g, B'^3\Sigma_u^-, W^3\Delta_u)$, we find $O_2^+$, $O_4^+$, $HO_2^+$, $H_2^+$, $H_3^+$, $O_2^-$, $O_3^-$, $O_2^-$, as well as $N_2^+$, $N_4^+$, and $HN_2^+$. The triples denote three different states at once, that are lumped together in the simulation. The chemical kinetics of $O_2/N_2$-plasmas is much more complicated than that of $O_2$/He-plasmas: Next to a wider variety of excited states, the former should involve the species NO, $NO_2$, $NO_3$, $NO^-$, $NO^+$, $NO_2^-$, NO2+, $NO_3^-$, $N_2O$, $N_2O^+$, $N_2O^-$, and $N_2O_5$. For example, the "Discharge in dry and humid air" mechanism compiled by Adamson et al. [17] involves 223 reactions, only about 50 of which are not describing the direct interaction of oxygen and nitrogen species.

Interaction between various helium and nitrogen plasma species are discussed in [109]. Ionin et al. as well as Uddi et al. also present oxygen plasma mechanisms containing nitrogen for different systems [41, 102]. Tailored for particular applications with given parameters, possible temperature dependencies in chemical reactions are often neglected. The later mechanism contains 97 reactions, considers excited species such as two atomic oxygen species and the associated $N_2$ chemistry in good detail. Finally, the mechanism presented by Ombrello et al. [64] contains many $O_2(a^1\Delta_g, b^1\Sigma_g^+)$ reactions in the context of the combustion mechanism they present.

## 4.2 On plasma assisted combustion

We report of experiments and theoretical research into plasma assisted combustion for the various motivations described in the introduction chapter, e.g. the possibility of flammability limit extension. For an investigation of the applicability of plasma effects on exhaust gases, see Orlandini [66] and references therein.

### 4.2.1 Hydrogen gas studies

A good summary of advantages of plasma treatment for hydrogen combustion is given in Starik's paper "Numerical study of the enhancement of combustion performance in a scramjet combustor due to injection of electric-discharge-activated oxygen molecules" [95]. Regarding the effect on flame speed and flammability limits, the theoretical analysis in [92] suggested that the influence of excited oxygen is strongest for lean mixtures. Numerical simulations [96] predict stronger reduction of ignition delay time for $H_2$-systems with growing electrical field value.

See Smirnov et al. [86] for the effects on laminar flames and also Bourig [13] for a long discussion of oxygen hydrogen flames with and without oxidizer excitation.

The latter also contains a full reaction mechanism involving one excited molecular and one excited atomic oxygen species [13]. The simulations in that work were built on the scheme described in Ibraguimova et al. [40] and Smekhov et al. [84]. The works by Popov et al. on plasma-assisted combustion kinetics have been mentioned in the preceding section [73–75]. See also [45] for an earlier investigation of excited oxygen quenching in $H_2$ mixtures. Another important contribution in form of a full reaction mechanism is also provided by Starik in [94]. Theoretical investigations are continued and validated in [83, 96].

### 4.2.2 Methane gas studies

Mirroring the hydrogen case, experiments (as well as theoretical analysis) of plasma assisted methane combustion are also performed in Starik's work, see e.g. "On the influence of singlet oxygen molecules on the speed of flame propagation in methane-air mixture" [93]. Here the result is that flame speed can be raised using excited oxygen, in particular for lean CH4-mixtures. Addition of $O_2(a^1\Delta_g)$ is shown to extend lean and rich flammability thresholds and is more effective than mere heating. However, it is reported that this only works well if the excitation is done close enough to the flame zone. The discussion is continued in [94, 96]. Reduction of ignition delay times for fields around 11 Td are predicted.

At the same time, the team at the Russian company *Kintech* has been working on low $T$ / high $p$ mechanisms for $CH_4$/Air with plasma for some time now [24, 54]. The latter is a recent paper containing detailed investigation of methane chain initiation reactions.

Sun et al. [101] emphasise a point on low temperature chemical kinetics. Such chemistry, if too slow, can and is often neglected in usual applications. However, in a plasma system setting such as discussed here, these reactions may become relevant.

Quenching by methane is discussed in [5]. See also Ombrello et al. [64,65], for a discussion on the modern singlet oxygen literature, including a discussion of the papers by Popov, Starik, Titova, among others.

### 4.2.3 Syngas studies

For completeness, it is worth noting that in recent years a theoretical model of the effect of $O_2(a^1\Delta_g)$ and $O_2(b^1\Sigma_g^+)$ on syngas (mixtures of hydrogen and carbon monoxide) mixtures has also been developed, see [82, 96].

# 5 Experiment and results at Magdeburg University

Below we describe the setup and results of the recent plasma assisted combustion experiments at Magdeburg University [6, 52, 55] and also [69–72]. This project is a follow-up to previous studies [9–13] performed before 2010. Those experiments concerned the generation of excited oxygen for plasma assisted combustion at $p = 100\,\mathrm{Torr}$ and using various discharges, which are also elaborated on in [67, 68]. A central aspect is $O_2(b^1\Sigma_g^+)$ spectroscopy experiments. The new experiment is designed to test the feasibility of excited oxygen generation and its subsequent combustion at atmospheric pressures. We now present a description of the experimental apparatus, followed by the obtained results. A table summarizing all available data specifying the system is given in the modeling subsection 8.1.

Note that, for example, compared to simulations performed in [13], the EEDF calculations performed in the present work are not merely done prior to the chemical kinetics simulation, but instead in parallel. This enables a more accurate simulation of the different interactions present in the system. As such, the accuracy of the discharge computations below, used to characterize the radical pool and eventual composition of the oxidizer stream is more advanced than in previous studies.

## 5.1 Description of the discharge and burner setup

The combustion experiments are performed using a helium diluted, premixed methane or hydrogen fuel, at room temperature. The discharge device can be divided into two parts, namely the discharge generator and the burner volume, which are connected by a tube of 1.4 cm in length.
The photograph in figure 1 shows the discharge in operating mode, but with the burner on top removed. The discharge area is the volume encapsulated by a transparent quartz tube containing two electrodes, see the computer graphic in figure 7 on the left. In the same figure on the right we see the scheme of the golden burner head. The photographs in figure 8 depict those two parts in full.

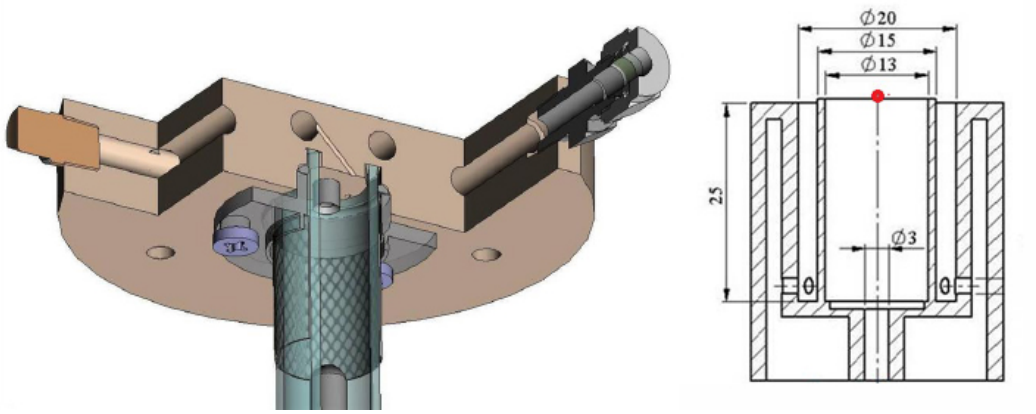


Figure 7: Left: Computer generated design of the discharge zone, also depicted in figure 8; Right: Cross section of the burner module on top of the discharge outlet.

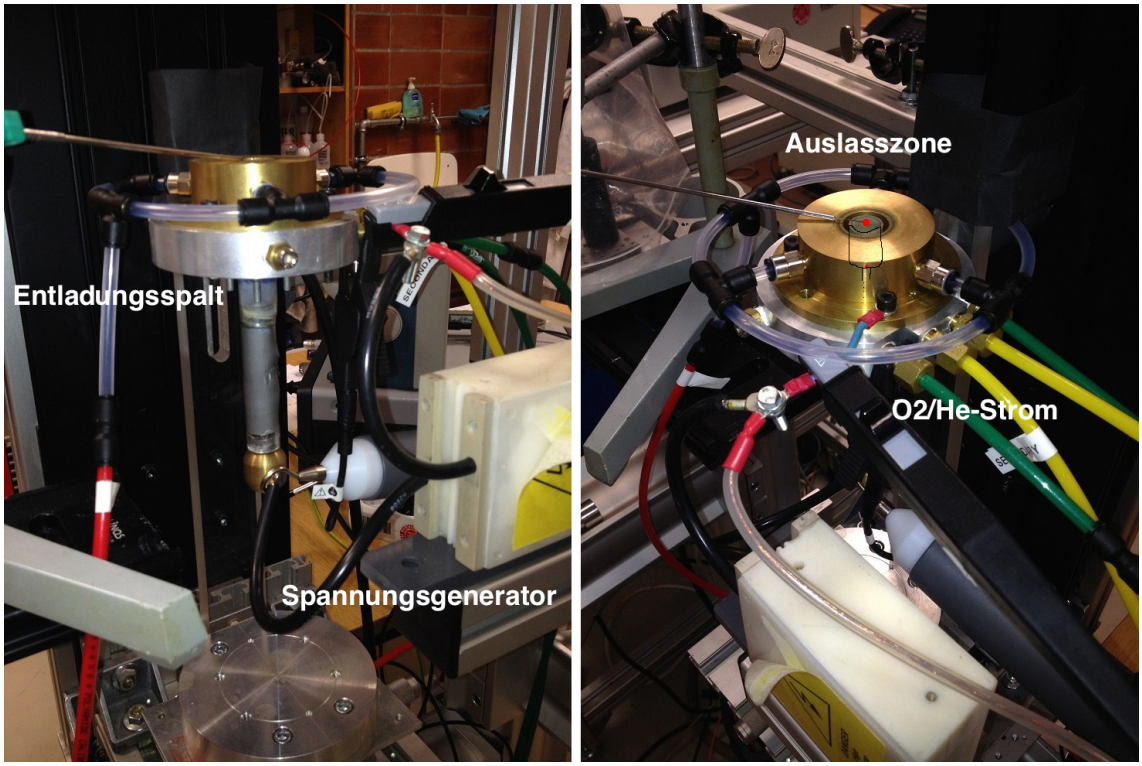


Figure 8: Full plasma assisted combustion setup; Right: Differently colored cables provide oxidizer, fuel and cooling gas; Left: The voltage cables on both ends of the discharge are black.

The total encapsulated volume is approximately 4.5 $cm^3$ and the discharge geometry cross section is smaller than 5 $cm^2$. Also note that the quartz tube is surrounded by a metal grid, simply to ease breakdown. The electrical field is generated between those unshielded metals, as opposed to a dielectrical barrier discharge configuration. One must keep in mind that there is also an electrical field inside the tube and so the effective discharge volume may be longer than the 1.1 cm long electrode gap inside this volume.

Upon turning on the discharge, physiochemical processes are initiated inside the volume. Here, as described in the introductory section, the electron density suddenly rises due to ionizations through particle collisions of the incoming oxidizer and initial electrons escaping the electrodes. The upper electrode is the first point where excited particles will quench on the wall. The lower electrode is a thick pin, while the whole upper metal complex may be thought of as the opposite electrode. Given the overall complex geometry, even if the applied voltage was static, the spatial form of the electrical field is hard to predict. The voltage field can be assumed to be linearly growing in the center, i.e. rise moderately. This is where most of the power transfer takes place. It is not quantitatively known where the electrical current attaches or what its effective diameter is. The experimenters estimate that it may enter partially, up to 3 mm and attach one-sidedly. The discharge has previously been described as an arc, although one must refrain from stating that the plasma is in "arcing mode", as this expression is generally reserved for high temperature plasmas.

## 5.2 Description of the voltage generator

The RF power generator (figure 1) generates the electrical field necessary to create the plasma in the discharge zone. It first translates the AC voltage $U_{\text{ext}}$ from a common socket to a 400 V DC voltage. This, in turn, is used to produce a series of more complicated voltage oscillations of varying amplitude at the discharge gap. Heuristically, the electrical field $E$ can be estimated as $E = \frac{U_d}{d}$, where $d$ is the discharge gap. Notice, however, that the formula is only strictly valid for DC systems. The circuit configuration employs the resonance phenomenon to produce a high voltage of $\approx 12\,\text{kV}$ at the discharge gap, which is sufficient for breakdown. In the so-called *working mode*, which is established after the voltage breakdown in the previously insulating gap, the generator works as a current generator to produce a stable voltage and current $I_d$, which are both measurable in principle. The voltage is measured to be $U_d \approx 1\,\text{kV}$ in working mode. The current is measured to be $I_d \approx 0.7\,\text{A}$ or higher. All these values slightly depend on the species concentrations in the gap, which influence its resistance $R_d$.

The generator has an adjustable *duty cycle*, which is defined as the fraction of time it is effectively turned on. The frequency is $f_0 \approx 1.176\,\text{MHz}$, so that one pulse duration is $T = \frac{1}{f_0} \approx 1\,\mu\text{s} = 10^{-6}\,\text{s}$. This is in the so-called medium frequency range of electromagnetic radiation (300-3000 kHz, $100-1000\,\text{m}$), i.e. lower than microwaves (300-3000 MHz, $0.1-1\,\text{m}$). Moreover, the device has a repetition frequency of 20 kHz corresponding to $50\,\mu\text{s}$ and an adjustable duty cycle that takes values of $10, 15, 25, 40, 50, 75$ and 100 percent. For example, this means that it can only be run at the first $\frac{3}{4}$ of the $50\,\mu\text{s}$-circle and start a new breakdown after that time.

The device is built to provide a power of up to 450 W and is typically ran around 150 W. Effective energy consumption depends on the characteristics of the plasma: Gas flowing through a discharge consumes as much energy as the chemistry allows. For an oxygen flow, electrical energy translates into various excitations and so, for example, a $O_2$/He mixture consumes more than pure He, and a $O_2/N_2$ mixture such as air can consume even more. This effect has also been observed in the experiment by intercepting the generator current outlet with an Amperometer. For constant 400 V DC, the current can change from 400 mA to 500 mA when about 3% of $O_2$ is added to helium. This also has the negative implication for different flow rates and concentrations. The energy input can not be kept at a fixed value. And in general, higher flow rates imply less coupling time of the gas to electrical energy sources and hence a smaller temperature rise. The heat capacities of these substances are different and so the temperature rise also slightly depends on the flow.

## 5.3 Experimental results

### 5.3.1 Plasma generation

Oxidizer and fuel flow rates in the experiments are varied for equivalence ratios from 0.54 to 1. As a main success of the experiment, it can be noted that excited molecular oxygen in the $O_2(b^1\Sigma_g^+)$ state are detected up to 5 cm above the discharge outlet, i.e. 3 cm above the mixing zone outlet. The sweet spot for $O_2(b^1\Sigma_g^+)$ yield is established as 3.2% $O_2$ in He at a flow rate of $q = 0.31\,\mathrm{m}^3/\mathrm{h}$. With increase of the oxidizer flow rate, excited oxygen molecules are also detected higher upstream. The measured power $P = U \cdot I$ grows linearly with higher duty cycle. Higher powers, in turn, are found to lead to higher excited particle generation. Here, voltage and current are measured at the generator, not at the gap. We are interested in the situation for 100% duty cycle. The pure helium flow consumes about 190 W, while a mixture of 3.2% oxygen in helium already draws 270 W. Those values don't take into account the effective efficiency $\eta_P$ of the device, which the producers of the generator estimate to be $\frac{3}{4}$, [70].

### 5.3.2 Flame

The main optical results are obtained via $O_2(b^1\Sigma_g^+)$ spectroscopy at 762 $nm$ at various heights after the discharge outlet, figure 8. These are relative intensity measurements. Modifications of the flame structure when the discharge generator is turned on are analyzed by planar laser induced flourescence of OH, as well as by Raman scattering and spontaneous emission of OH, CH and $C_2$. Finally, particle imaging velocimetry has been used to characterize the flow geometry. Absolute species concentrations are not measured. Temperature measurements are obtained via "type-K" thermocouple at the discharge outlet (after the tube, i.e. 1.1 cm past the discharge zone) as well as at the burner module outlet (1.1 cm + 2.5 cm past the discharge zone), as shown in figure 8. Note that metal parts of the discharge and burner also absorb heat.

When adding premixed fuel, the mixing temperatures are nevertheless too low for auto-ignition. This holds for any parameter configuration and so the mixture must be ignited manually. But even without flame, small quantities of combustion products are detected when the discharge is turned on. In working mode at high power input, a modification of the flame geometry is visible for all flames: The flame tilts inwards, toward the plasma outlet. However, the changes of OH data do not noticeably differ with respect to the oxidizer concentration, suggesting that the changes are brought about by thermal means. The maximal thermal flame power is 2.87 kW.

### 5.3.3 Temperature development

A problematic issue arises with regard to the discharge temperature. Despite the initial planning for the construction of the discharge device, the temperature of the oxidizer flow does not stay low. The flow enters the discharge zone at a temperature of about $T = 300\,\mathrm{K}$

and depending on substance fractions and discharge setting, the corresponding temperature at the burner outlet is measured to have risen by up to 800 K. In figure 9 we see the temperature differences as measured between the oxidizer injection and the burner outlet, plotted against the high temperature at the burner outlet, for various duty cycles. For each duty cycle, a gray line connects the values for pure helium (left) and a mixture with 3.2% oxygen addition (right). For those pairs, temperature at the outlet differs by a factor of about 0.86 and this value is largely independent of duty cycle.

A related inconvenient feature of the experimental application is the transition to the so-called arcing mode. At 75% and 100% duty cycle and when considering an oxygen containing mixture, one observes a sudden change of the current: it glows whiter, the sound changes and a local overheating of the electrode occurs, so that the discharge has to be stopped. This implies that for these parameter ranges, the output flow never reaches a stable configuration and no final temperature or optical measurements can be made. Optical experiments counting incidents of excited particles are averages over a certain time span, and for these regimes in which the system never reaches steady state, their value is questionable. For experiments performed in Bochum, the parameter space leading to arcing are established in figure 5.

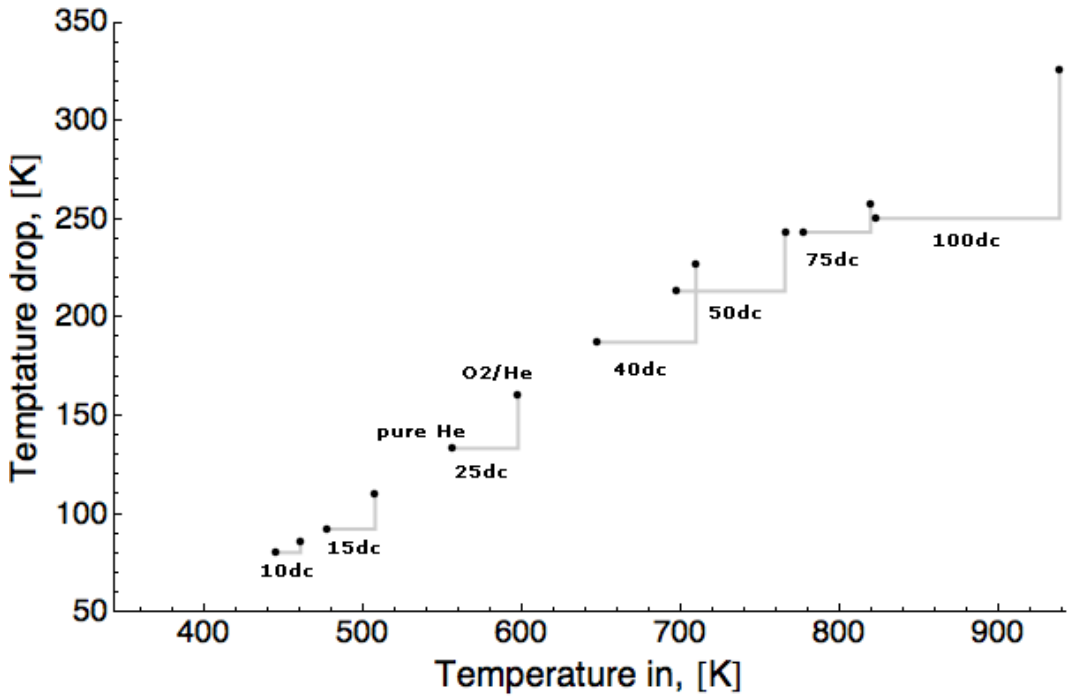


Figure 9: Temperature differences between the injection and the burner outlet, vs. temperature at the burner outlet. For each duty cycle, a gray line connects the values for pure helium (left) and a mixture with 3.2% oxygen addition (right). For those pairs, temperature at the outlet differs by a factor of about 0.86 and this value is largely independent of duty cycle.

# Part II

# Oxygen-helium discharges and combustion mechanisms

This chapter is a study of reaction mechanisms of oxygen-helium plasmas, as well as their combustion with hydrogen and methane fuel. Firstly, the principal types of reactions that we can expect are listed. Then literature regarding reaction mechanisms as well as explicit reaction rate coefficients $k(T)$ is compared. Particular attention is given to the excited states of oxygen.

Note that in the following, not all reactions can be assigned to one of the classification categories. For example, a reaction such as $AB^+ + e^- \rightarrow A + B$, where A, B denote any molecule, is both a recombination of charged particles and an electron impact dissociation.

## 6 Rates for discharge zone mechanisms

We start with a discussion of reaction mechanisms suitable for chemical kinetics simulations of a $O_2$/He system in the discharge zone at atmospheric pressures coupled to a non-equilibrium Boltzmann solver. The investigation is performed by contrasting the reactions of a mechanism [18] involving several electronically excited oxygen species and extended by processes modeling helium species interactions (this is a scheme with thermodynamical data adapted from the oxygen sub-mechanism of the "$CH_4/Air$ plasma mechanism" [24] from the *Chemical Workbench* library, anno 2012), against other proposals encountered in the literature. In total, this oxygen/helium plasma mechanism is given by a list of 185 reactions, many of which are unidirectional. Of those, 23 contain helium species and 70 contain electrons. Formally, it contains the electron and the following 37 species:

- $6 + 2 + 1$ neutral oxygen species: $O_2$, $O_2(r)$, $O_2(v)$ $O_2(a^1\Delta_g)$, $O_2(b^1\Sigma_g^+)$, $O_2(4.5)$, as well as O, $O(^1D)$ and $O_3$.
- $7 + 2 + 1$ charged species: $O^-$, $O^+$, $O_2^-$, $O_2^+$, $O_3^-$, $O_4^-$, $O_4^+$ and $He^+$, $He_2^+$ and $e^-$.
- Several states leading to a molecule dissociation are lumped together to the following 6 states: $O_2(B^3\Sigma_u^-)$ as well as $O_2(dis)$, $O_2(disreg)$, $O_2^-(dis)$, $O_2^+(dis)$ and $O_3^-(dis)$.
- There are 9 atomic oxygen states, used for the implementation of diffusive losses at the wall: $O(^3P)$ (representing atomic oxygen in the ground state) as well as $O(^1S)$, $O(^5P)$, $O(5S3s)$, $O(3S3s)$, $O(5S4s)$, $O(3D3d)$, $O(5D3d)$ and $O(3S4s)$. The species names here are those from the Chemical Workbench software package.
- Finally, there are 3 neutral helium species: He, $He^*$, $He(met)$. The tables in this chapter contain several helium processes, which together comprise a simple pure helium plasma sub-mechanism, that is later also used in the modeling and simulation sections.

To get a feeling for the apparent differences of approaches in the literature, compare this setup to the very different mechanism used by Waskoenig et al. [107]. It comprises "only" 116 unidirectional reactions, about 60 of which are nevertheless different from the reactions in [18]. While the bulk of the non-equilibrium reactions is part of both mechanisms (about 25 reactions), the Waskoenig mechanism lacks higher excited molecular oxygen species (27 reactions involving $O_2(b^1\Sigma_g^+)$ and 10 more involving $O_2(4.5)$), while including a more detailed oxygen-helium interaction chemistry (about 20 additional reactions). Waskoenig lacks some species of smaller relevance for our purposes, such as $O_4^-, O_4^+$ and also vibrational as well as exotic excited atomic oxygen particles, while incorporating $He_2(met)$.

Because of the broad variety of parameters and applications, the oxygen plasma mechanisms in the literuature have differences in their implementation of charge transfer, recombination and electron attachment and detachment processes. And even when reactions do match, the rate coefficients are often different.

Some of the dissociation states above are mere auxiliary species in the sense that their dissociation rate is artificially set to be extremely high. The same is true for rotational and vibrational relaxation of molecules: If the relaxation rate coefficients of some processes $O_2^* \to O_2$ are much larger than others processes, then setting them to infinity does not affect the effective macroscopic chemistry.

For readability, the bimolecular, unimolecular and third body reactions of a class will be presented separately. The majority of process rates are represented as Arrhenius rates

$$k = A\,T^n\,\mathrm{e}^{-E/k_BT}.$$

Unless otherwise noted, the energies are stated in units of kcal. The units of reaction rate coefficients is $\mathrm{cm}^{3n}/\mathrm{s}$, where $n$ is 0, 1 or 2, depending on the reaction order.

The uncertainty for cross section data for $O_2$/He plasma processes often lies in the range of 30% [107].

About 60 of the electron reactions in [18] are of "electronical type", meaning they are associated with lists of cross section data $\sigma(\varepsilon)$ and so their process rates

$$k = \int f(\varepsilon)\,\varepsilon^{1/2}\,\sigma(\varepsilon)\,\mathrm{d}\varepsilon$$

depend on the electron energy distribution function $f$, i.e. the solution of the Boltzmann equation. See Eliasson [27] for modeling data in the context of oxygen systems as well as the standard reference [8]. Data from the latter source are also integrated in the presently discussed mechanism. As is common practice, we will use the abbreviation "EEDF" in place of numerical values for the energy dependent cross sections.

## 6.1 Oxygen plasma

### 6.1.1 Bimolecular reactions of neutral molecules

To understand the scheme in table 4, we list the main reaction types that we can expect from a mechanism aimed at describing excited oxygen production. The first such types are oxygen species excitations and quenching:

- $O_2 + A \leftrightarrow O_2(a^1\Delta_g, b^1\Sigma_g^+, 4.5) + A.$
- $O_2(a^1\Delta_g) + A \leftrightarrow O_2(b^1\Sigma_g^+, 4.5) + A.$
- $O_2(b^1\Sigma_g^+) + A \leftrightarrow O_2(4.5) + A.$

Note that unless the energy in the system is very high, the radicals and excited species concentrations will always stay small compared to the concentrations of the corresponding ground state molecule. Hence, as far as the coefficients for quenching *by* excited particles are comparable to those of quenching by ground state species, the former are less relevant for an accurate description. This is particularly true for the discharge zone. The difference of quenching rates for hydrogen and hydrocarbon fuels will be discussed below. The largest representative of excited oxygen reactions employed are in fact the quenching reactions for $O_2(a^1\Delta_g)$, i.e.

$$O_2(a^1\Delta_g) + M \leftrightarrow O_2 + M.$$

Starikovskiy [98] discusses reactions for systems of such high temperatures, in which $O_2(a^1\Delta_g)$ and $O_2(b^1\Sigma_g^+)$ are neglected for being "low" energy states. As such, the scheme includes direct $O_2(4.5)$ quenching by $O_2$ and O with rates of $k = 3.3\times10^{-13}\,\mathrm{cm}^3/\mathrm{s}$ and $k = 9.0\times10^{-12}\,\mathrm{cm}^3/\mathrm{s}$, respectively.
An important source of $O_2(a^1\Delta_g)$ is simply $O_2(b^1\Sigma_g^+)$ quenching, also-called "cascade deactivation" [79]. In the afterglow, $O_2(b^1\Sigma_g^+)$ will decay, but at the same time a production channel for it is the so-called pooling reaction

$$O_2(a^1\Delta_g) + O_2(a^1\Delta_g) \rightarrow O_2(b^1\Sigma_g^+) + O_2.$$

Kovalev [49] finds O to be the most important particle for the deactivation of $O_2(b^1\Sigma_g^+)$. Cascading processes from higher so-called Herzberg electronic states contribute to a lower degree in populating the $O_2(b^1\Sigma_g^+)$ state. We will later discuss this topic in the context of our system. Finally, atomic oxygen O will always be present in an oxygen containing plasma and can also notably quench excited oxygen states.

The obvious dissociation reaction candidates are of the form

$$O_2 + A \leftrightarrow O + O + A,$$

$$O_3 + A \leftrightarrow O_2 + O + A.$$

One must also take excited oxygen dissociation reactions into account. In this case, due to the surplus of energy, we can expect more and possibly faster reaction pathways. As prototypes, consider the following:

- $O_2(a^1\Delta_g, b^1\Sigma_g^+) + A \leftrightarrow O + O + A$.
- $O_2(a^1\Delta_g, b^1\Sigma_g^+) + A \leftrightarrow O + AO$.
- $O_2(a^1\Delta_g, b^1\Sigma_g^+) + AO \leftrightarrow O_3 + A$.

Variations of those reactions, where ground state atomic oxygen O is replaced by its main electronically excited pendant $O(^1D)$ [93], are also important. This particle is also an important ingredient in several reaction mechanisms, see e.g. Uddi et al. [102]. A thorough discussion on $O_2$-dissociation is found in the textbook of Capitelli et al. [15]. Kovalev et al. [49] also discuss dissociation reactions in the context of discharges.

| **Reaction** | **Rate coefficient**, $[\mathrm{cm}^{-3}/\mathrm{s}]$ |
|---|---|
| $O_2(a^1\Delta_g) + O \rightarrow O + O_2$ | $1.288 \times 10^{-16}$ |
| $O_2(a^1\Delta_g) + O_2 \rightarrow O_2 + O_2$ | $2.188 \times 10^{-18}$ |
| $O_2(a^1\Delta_g) + O_3 \rightarrow O_2 + O_2 + O$ | $5.012 \times 10^{-11}\ \mathrm{e}^{-5.66/RT_\mathrm{g}}$ |
| $O_2(a^1\Delta_g) + O_2 + O \rightarrow O_2 + O_2 + O$ | $2.512 \times 10^{-32}$ |
| $O_2(a^1\Delta_g) + O_2(a^1\Delta_g) \rightarrow O_2(b^1\Sigma_g^+) + O_2$ | $2.188 \times 10^{-18}$ |
| $O_2(b^1\Sigma_g^+) + O \rightarrow O_2 + O$ | $3.981 \times 10^{-14}$ |
| $O_2(b^1\Sigma_g^+) + O \rightarrow O_2(a^1\Delta_g) + O$ | $3.981 \times 10^{-14}$ |
| $O_2(b^1\Sigma_g^+) + O_2 \rightarrow O_2 + O_2$ | $1.514 \times 10^{-16}$ |
| $O_2(b^1\Sigma_g^+) + O_2 \rightarrow O_2(a^1\Delta_g) + O_2$ | $3.981 \times 10^{-17}$ |
| $O_2(b^1\Sigma_g^+) + O_3 \rightarrow O_2 + O_2 + O$ | $1.514 \times 10^{-11}$ |
| $O_2(b^1\Sigma_g^+) + O_3 \rightarrow O_2(a^1\Delta_g) + O_2 + O$ | $7.079 \times 10^{-12}$ |
| $O_2(4.5) + M \rightarrow O_2 + M$ | $2.291 \times 10^{-14}$ |
| $O_2(4.5) + M \rightarrow O_2(a^1\Delta_g) + M$ | $1.862 \times 10^{-13}$ |
| $O_2(4.5) + M \rightarrow O_2(b^1\Sigma_g^+) + M$ | $8.128 \times 10^{-14}$ |
| $O_2(4.5) + O_2 \rightarrow O_2(a^1\Delta_g) + O_2$ | $1.000 \times 10^{-13}$ |
| $O_2(4.5) + O_2 \rightarrow O_2(b^1\Sigma_g^+) + O_2$ | $8.913 \times 10^{-13}$ |
| $O_2(4.5) + O \rightarrow O_2(a^1\Delta_g) + O$ | $1.000 \times 10^{-13}$ |
| $O_2(4.5) + O \rightarrow O_2(b^1\Sigma_g^+) + O$ | $8.913 \times 10^{-13}$ |
| $O(^1D) + O \rightarrow O + O$ | $7.413 \times 10^{-11}$ |
| $O(^1D) + O_2 \rightarrow O + O_2(b^1\Sigma_g^+)$ | $2.570 \times 10^{-11}\ \mathrm{e}^{0.134/RT_\mathrm{g}}$ |
| $O(^1D) + O_2 \rightarrow O + O_2$ | $7.586 \times 10^{-12}\ \mathrm{e}^{0.134/RT_\mathrm{g}}$ |
| $O(^1D) + O_3 \rightarrow O + O_3$ | $2.399 \times 10^{-10}$ |
| $O(^1D) + O_3 \rightarrow O_2 + O + O$ | $1.202 \times 10^{-10}$ |
| $O(^1D) + O_3 \rightarrow O_2 + O_2$ | $2.291 \times 10^{-11}$ |
| $O(^1D) + O_3 \rightarrow O_2(a^1\Delta_g) + O_2$ | $1.514 \times 10^{-11}$ |
| $O(^1D) + O_3 \rightarrow O_2(b^1\Sigma_g^+) + O_2$ | $7.762 \times 10^{-12}$ |
| $O(^1D) + O_3 \rightarrow O_2(4.5) + O_2$ | $7.413 \times 10^{-11}$ |
| $O + O_2 + O_2 \leftrightarrow O_3 + O_2$ | $8.603 \times 10^{-31}\ (T_\mathrm{g}/\mathrm{K})^{-1.3}$ |
| $O + O_3 \leftrightarrow O_2 + O_2$ | $9.550 \times 10^{-12}\ \mathrm{e}^{-4.6/RT_\mathrm{g}}$ |
| $O + O_3 \leftrightarrow O_2(a^1\Delta_g) + O_2$ | $6.310 \times 10^{-12}\ \mathrm{e}^{-4.6/RT_\mathrm{g}}$ |
| $O + O_3 \leftrightarrow O_2(b^1\Sigma_g^+) + O_2$ | $3.163 \times 10^{-12}\ \mathrm{e}^{-4.6/RT_\mathrm{g}}$ |

Table 4: Reactions of neutral oxygen species [18].

In the combustion zone, the reaction $O(^1D) + H_2 \rightarrow OH + H$ can be expected to be more efficient to "trigger the chain reactions of the transformation of $H_2$ to $H_2O$" than its unexcited counterpart, affecting ignition delay times. However, while $O(^1D)$ is extremely reactive, for the simulations performed later it will turn out that its quenching is too strong for it to be relevant in the combustion zone. Notably, table 4 already contains most reactions involving $O(^1D)$ and $O_2(4.5)$ in the mechanism [18].

There is much dispute about rates of specific quenching reactions in the literature. The bimolecular quenching rate coefficients of the order of $10^{-18}\,\mathrm{cm}^3/\mathrm{s}$ are characteristic for $O_2(a^1\Delta_g)$. The quenching coefficients of $O_2(b^1\Sigma_g^+, 4.5)$ down to $O_2$ and $O_2(a^1\Delta_g)$ are higher, but the overall concentration of higher excited states, out of the discharge, will typically be smaller than that of $O_2(a^1\Delta_g)$. For example, the reaction $O_2(a^1\Delta_g) + He \rightarrow O_2 + He$, which a priori could be relevant, does not appear in table 4. However, in the literature we find values in the range of only $k = 8 \cdot 10^{-27}(300/T_g)^{0.5}\,\mathrm{cm}^3/\mathrm{s}$, see [14, 107]. Hence $k \ll 10^{-18}\,\mathrm{cm}^3/\mathrm{s}$ for the considered purposes and this process does not have an impact on the simulation. The quenching rate of $O_2(a^1\Delta_g)$ by $O_2$ in the low pressure simulations performed by Bourig [13], $k = (4.0 \pm 0.4) \times 10^{-17}\,\mathrm{cm}^3/\mathrm{s}$, lies an order of magnitude above the value in the list above. The combustion mechanisms by Starik [93, 95] contain a whole range of excited oxygen reactions with other oxygen species akin to the ones discussed.

The neutral molecule interactions between oxygen and helium particles will be described in detail in subsection 6.2. In [107], from their simulation of an oxygen-helium system at atmospheric pressures, Waskoenig et al. report the following reactions to be of primary importance for excited oxygen production and destruction:

$O_2(a^1\Delta_g)$ **production:**

- $O_2 + e^- \rightarrow O_2(a^1\Delta_g) + e^-$.
- $O(^1D) + O_2 \rightarrow O + O_2(a^1\Delta_g)$.
- $O + O + He \rightarrow O_2(a^1\Delta_g) + He$.

$O_2(a^1\Delta_g)$ **destruction:**

- $O_2(a^1\Delta_g) + O_3 \rightarrow O_2 + O_2 + O(^1D)$.

The second production reaction here is not part of table 4 above. This is because it contains the excitation to $O_2(b^1\Sigma_g^+)$ (R19 in table 4), while the distinction between electronically excited oxygen states is neglected by the Waskoenig mechanism. Conversely, the latter mechanism has very rich $O(^1D)$ chemistry, which we will not discuss in more detail here.

### 6.1.2 Third body reactions of neutral species

The most relevant reaction for excitation of electronic oxygen states inside plasma discharges are naturally the electron impact ionizations [41] and to a lesser extent also excitations by collisions with neutral collision partners. Excited species can moreover be the result of recombination of atomic oxygen, tables 5 and 6.

Excitation is often described as a stepwise process through $O(^1D)$, i.e.

$$O(^1D) + O_2(X^3\Sigma_g^-) \rightarrow O(^3P) + O_2(b^1\Sigma_g^+),$$

despite the fact that production processes data, e.g. for $O + e^- \rightarrow O(^1D) + e^-$, are not well known [79]. For growing pressures, $O_3$ production is favored and the O-absorption reaction $O_2 + O + M \rightarrow O_3 + M$ naturally works against the above process. Ozone itself is a strong quencher as well.

Quenching may also occur as three body reaction, such as

$$O_2(a^1\Delta_g, b^1\Sigma_g^+) + A + B \leftrightarrow O_2 + A + B.$$

Sousa et al. [87] expects

$$O_2(a^1\Delta_g) + O + He \rightarrow O_2 + O + He$$

to be important for the oxygen-helium system, at least in the afterglow. Hicks et al. [36] suggest

$$O_2(a^1\Delta_g) + O + M \rightarrow O_2 + O + M$$

with $k_{O_2} = 10^{-32}\,\mathrm{cm^6 s^{-1}}$ for $M = O_2$, and $k_{Ar} = 0.63 \times k_{O_2}$ for $M = Ar$. The value of the oxygen molecule is highly debated in the community and the value for helium ought to be close to the value for argon.

| **Reaction** | **Rate coefficient**, $[\mathrm{cm^{-3}/s}]$ |
|---|---|
| $O + O + M \leftrightarrow O_2(a^1\Delta_g) + M$ | $1.318 \times 10^{-30}\ (T_g/\mathrm{K})^{-1}\ e^{-0.34/RT_g}$ |
| $O + O + M \leftrightarrow O_2(b^1\Sigma_g^+) + M$ | $6.026 \times 10^{-31}\ (T_g/\mathrm{K})^{-1}\ e^{-0.34/RT_g}$ |
| $O + O + M \leftrightarrow O_2(4.5) + M$ | $1.202 \times 10^{-34}$ |
| $O + O + M \leftrightarrow O_2 + M$ | $3.309 \times 10^{-31}\ (T_g/\mathrm{K})^{-1}$ |
| $O + O_2 + M \leftrightarrow O_3 + M$ | $6.918 \times 10^{-34}$ |

Table 5: Trimolecular reactions of neutral species [18].

| **Species** | $H_2$ | $H_2O$ | $CH_4$ | CO | $CO_2$ | $C_2H_6$ | Ar |
|---|---|---|---|---|---|---|---|
| **Efficiencies** | 2.4 | 15.4 | 2.0 | 1.75 | 3.6 | 3.0 | 0.83 |

Table 6: Collision efficiency parameters of the third body reactions in table 5.

### 6.1.3 Elastic electron-atom and electron-molecule collisions

Tables 7-12 present processes involving electrons. Ordered by the quantity of energy involved, we expect elastic scattering, inelastic scattering, ionization and finally dissociation. A general reference for cross section data can be found at the webpage of the *Plasma Data Exchange Project* [53] and for a topical summary, see "Physics and engineering of singlet delta oxygen production in low-temperature plasma" by Ionin et al. [41]. Improvements of many of the listed data for processes in this chapter are also listed in the *Chemical Workbench* reaction database [17].

Elastic scattering of electrons, table 7, is very important for energy transfer through the discharge. For a helium mixture with only a small oxygen fraction, the process

$$\mathrm{He} + \mathrm{e}^- \leftrightarrow \mathrm{He} + \mathrm{e}^-$$

affects the gas temperature the strongest.

| **Reaction** | **Cross section data** |
|---|---|
| $\mathrm{O_2} + \mathrm{e}^- \leftrightarrow \mathrm{O_2} + \mathrm{e}^-$ | EEDF |
| $\mathrm{O_2}(v) + \mathrm{e}^- \leftrightarrow \mathrm{O_2}(v) + \mathrm{e}^-$ | EEDF |
| $\mathrm{O_2}(a^1\Delta_g) + \mathrm{e}^- \leftrightarrow \mathrm{O_2}(a^1\Delta_g) + \mathrm{e}^-$ | EEDF |
| $\mathrm{O_2}(b^1\Sigma_g^+) + \mathrm{e}^- \leftrightarrow \mathrm{O_2}(b^1\Sigma_g^+) + \mathrm{e}^-$ | EEDF |
| $\mathrm{O} + \mathrm{e}^- \leftrightarrow \mathrm{O} + \mathrm{e}^-$ | EEDF |

Table 7: Elastic electron atom- and electron-molecule collisions [18].

### 6.1.4 Electron impact excitation of molecules and atoms

A few points can be noted about the electron impact excitation of molecules and atoms presented in table 8:

• Near the end of the table we find various exotic excitations of atomic oxygen. Those are, however, of no real significance for the outcome of our high pressure simulations.

• Note that if vibrational excitations are relaxing fast, releasing energy to the surroundings, the excitation to $\mathrm{O_2}(v)$ particles merely amounts to a temperature rise.

• The table includes a bidirectional process between $\mathrm{O_2}(v)$ and $\mathrm{O_2}(4.5)$, but no other excited state. In Capitelli's book [15], on the other hand, we moreover find reactions of the type

$$\mathrm{O_2}(v) + \mathrm{e}^- \leftrightarrow \mathrm{O_2}(b^1\Sigma_g^+) + \mathrm{e}^-.$$

Lastly, regarding non-equilibrium processes, the following commonly used estimation [103] should be mentioned. Given a process

$$\mathrm{A} + \mathrm{e}^- \rightarrow \mathrm{B} + \mathrm{e}^-,$$

with cross section $\sigma_{\mathrm{A}\rightarrow\mathrm{B}}(E)$, a cross section $\sigma_{\mathrm{A}\rightarrow\mathrm{B}^*}(E)$ to a higher state $\mathrm{B}^*$ may be estimated by $\sigma_{\mathrm{A}\rightarrow\mathrm{B}}(E - \Delta E)$, where $\Delta E$ is the internal energy difference of $\mathrm{B}^*$ and B. This is often employed for the excited oxygen states.

| Reaction | Cross section data |
|---|---|
| $O_2 + e^- \leftrightarrow O_2(r) + e^-$ | EEDF |
| $O_2 + e^- \leftrightarrow O_2(v) + e^-$ | EEDF |
| $O_2 + e^- \leftrightarrow O_2(a^1\Delta_g) + e^-$ | EEDF |
| $O_2 + e^- \leftrightarrow O_2(b^1\Sigma_g^+) + e^-$ | EEDF |
| $O_2 + e^- \leftrightarrow O_2(4.5) + e^-$ | EEDF |
| $O_2(v) + e^- \leftrightarrow O_2(4.5) + e^-$ | EEDF |
| $O_2(a^1\Delta_g) + e^- \leftrightarrow O_2(b^1\Sigma_g^+) + e^-$ | EEDF |
| $O_2(a^1\Delta_g) + e^- \leftrightarrow O_2(4.5) + e^-$ | EEDF |
| $O_2(b^1\Sigma_g^+) + e^- \leftrightarrow O_2(4.5) + e^-$ | EEDF |
| $O + e^- \leftrightarrow O(^1D) + e^-$ | EEDF |
| $O + e^- \leftrightarrow O(^3P) + e^-$ | EEDF |
| $O + e^- \leftrightarrow O(^1S) + e^-$ | EEDF |
| $O + e^- \leftrightarrow O(5S3s) + e^-$ | EEDF |
| $O + e^- \leftrightarrow O(3S3s) + e^-$ | EEDF |
| $O + e^- \leftrightarrow O(^5P) + e^-$ | EEDF |
| $O + e^- \leftrightarrow O(5S4s) + e^-$ | EEDF |
| $O + e^- \leftrightarrow O(3D3d) + e^-$ | EEDF |
| $O + e^- \leftrightarrow O(3S4s) + e^-$ | EEDF |
| $O + e^- \leftrightarrow O(5D3d) + e^-$ | EEDF |

Table 8: Electron impact excitation of molecules and atoms [18].

### 6.1.5 Ionization processes

| Reaction | Cross section data |
|---|---|
| $O_2 + e^- \leftrightarrow O_2^+ + e^- + e^-$ | EEDF |
| $O_2(v) + e^- \leftrightarrow O_2^+ + e^- + e^-$ | EEDF |
| $O_2(a^1\Delta_g) + e^- \leftrightarrow O_2^+ + e^- + e^-$ | EEDF |
| $O_2(b^1\Sigma_g^+) + e^- \leftrightarrow O_2^+ + e^- + e^-$ | EEDF |
| $O_2 + e^- \leftrightarrow O_2^+(dis) + e^- + e^-$ | EEDF |
| $O_2(v) + e^- \leftrightarrow O_2^+(dis) + e^- + e^-$ | EEDF |
| $O_2(a^1\Delta_g) + e^- \leftrightarrow O_2^+(dis) + e^- + e^-$ | EEDF |
| $O_2(b^1\Sigma_g^+) + e^- \leftrightarrow O_2^+(dis) + e^- + e^-$ | EEDF |
| $O + e^- \leftrightarrow O^+ + e^- + e^-$ | EEDF |
| $O(^1D) + e^- \leftrightarrow O^+ + e^- + e^-$ | EEDF |

Table 9: Ionization processes [18].

### 6.1.6 Electron impact dissociation of a molecule

In reference to the previous block of electron impact ionization reactions resulting in positive ions and more electrons, table 9, note that the state $O_2(dis)$ acts as placeholder for immediately dissociating molecules. The states which dissociate into O + O are $O_2(c^1\Sigma_u^-, A'^3\Delta_u, A^3\Delta_u^+)$ and tagged by such a "dis" keyword. The state dissociating into $O + O(^1D)$ is $O_2(B^3\Sigma_u^-)$. Table 10 is a very elaborate list of possible electron impact dissociations. Observe that those can also give rise to charged atomic oxygen particles. The energetically low vibrational excitations are neglected in the mechanism in the sense that they immediately decay as well. Ozone dissociations are included as well.

Inside the discharge zone, Sun et al. [101] report that the following three reactions contribute most to atomic oxygen formation in their low pressure system:

- $O_2 + e^- \leftrightarrow O + O(^1D) + e^-$.
- $O_2 + e^- \leftrightarrow O + O + e^-$.
- $O_2 + e^- \leftrightarrow O + O^+ + e^- + e^-$.

Those three processes are all included in the following scheme.

| **Reaction** | **Cross section data** |
|---|---|
| $O_2 + e^- \leftrightarrow O_2(dis) + e^-$ | EEDF |
| $O_2(v) + e^- \leftrightarrow O_2(dis) + e^-$ | EEDF |
| $O_2(a^1\Delta_g) + e^- \leftrightarrow O_2(dis) + e^-$ | EEDF |
| $O_2(b^1\Sigma_g^+) + e^- \leftrightarrow O_2(dis) + e^-$ | EEDF |
| $O_2 + e^- \leftrightarrow O_2(B^3\Sigma_u^-) + e^-$ | EEDF |
| $O_2(v) + e^- \leftrightarrow O_2(B^3\Sigma_u^-) + e^-$ | EEDF |
| $O_2(a^1\Delta_g) + e^- \leftrightarrow O_2(B^3\Sigma_u^-) + e^-$ | EEDF |
| $O_2(b^1\Sigma_g^+) + e^- \leftrightarrow O_2(B^3\Sigma_u^-) + e^-$ | EEDF |
| $O_2^+ + e^- \leftrightarrow O_2(disrec)$ | EEDF |
| $O_2 + e^- \leftrightarrow O_2^-(dis)$ | EEDF |
| $O_2(v) + e^- \leftrightarrow O_2^-(dis)$ | EEDF |
| $O_2(a^1\Delta_g) + e^- \leftrightarrow O_2^-(dis)$ | EEDF |
| $O_2(b^1\Sigma_g^+) + e^- \leftrightarrow O_2^-(dis)$ | EEDF |
| $O_2^-(dis) \rightarrow O^- + O$ | $\infty$ |
| $O_2^+(dis) \rightarrow O^+ + O$ | $\infty$ |
| $O_3^-(dis) \rightarrow O^- + O_2$ | $\infty$ |
| $O_2(dis) \rightarrow O + O$ | $\infty$ |
| $O_2(B^3\Sigma_u^-) \rightarrow O + O(^1D)$ | $\infty$ |
| $O_2(disrec) \rightarrow O + O$ | $\infty$ |
| $O_3 + e^- \rightarrow O_3^-(dis)$ | $3.0 \times 10^{-10}\,\mathrm{cm}^{-3}/\mathrm{s}$ |
| $O_3 + e^- \rightarrow O + O_2 + e^-$ | $1.0 \times 10^{-8}\,\mathrm{cm}^{-3}/\mathrm{s}$ |

Table 10: Electron impact dissociation of a molecule [18].

### 6.1.7 Electron attachment

The mechanism notably does not include the electron attachment process $O_2 + e^- + M \rightarrow O_2^- + M$, for $M = \mathrm{He}$. Among the three body reactions involving electrons, this one will be the most relevant to consider, because all the relevant mixtures to be looked at are comprised of over 90% helium. In an experiment discussed in the general plasma chemistry overview Starikovskiy [98] this reaction $O_2 + e^- + M \rightarrow O_2^- + M$ is found to be significant.

The $O_2^-$ particles are commonly destroyed in recombination with $O_2^+$, which affects the action of the electrical field on the oxidizer mixture. However, if the oxygen dissociation is high, then collisional electron detachment $O_2^- + O \rightarrow O_3 + e^-$ becomes the main destruction channel for $O_2^-$.

| **Reaction** | **Rate coefficient**, $[\mathrm{cm}^{-3}/\mathrm{s}]$ |
|---|---|
| $O_2 + O_2 + e^- \rightarrow O_2 + O_2^-$ | $3.981 \times 10^{-27}\ (T_\mathrm{g}/\mathrm{K})^{-1}\ \mathrm{e}^{-1.2/RT_\mathrm{g}}$ |
| $O_2 + O + e^- \rightarrow O_2 + O^-$ | $1.000 \times 10^{-31}$ |
| $O_2 + O_3 + e^- \rightarrow O_2 + O_3^-$ | $5.012 \times 10^{-29}$ |

Table 11: Electron attachment [18].

### 6.1.8 Electron detachment

The following reactions are secondary electron emission processes.

As the oxidizer dilution in our study case is high, the excited oxygen mole fraction is comparatively low. Thus, detailed analyses of particular processes, such as detachment by $O_2(a^1\Delta_g)$ impact $O_2^- + O_2(a^1\Delta_g) \rightarrow O_2 + O_2 + e^-$ discussed in Vagin et al. [103], are of small relevance for us.

We find a similar but less detailed list of detachments in [15]. A minor difference is that instead of the process from $O^- + O_2(b^1\Sigma_g^+)$ to $O_2 + O + e^-$, the authors consider the process that goes directly to $O_3 + e^-$. Moreover, the small rate coefficient for $O_3^- + O_2 \rightarrow O_2 + O_3 + e^-$ is implemented in a way that depends on the gas temperature.

| **Reaction** | **Rate coefficient**, $[\mathrm{cm}^{-3}/\mathrm{s}]$ |
|---|---|
| $O^- + O \rightarrow O_2 + e^-$ | $1.905 \times 10^{-10}$ |
| $O^- + O_2 \rightarrow O_3 + e^-$ | $5.012 \times 10^{-15}$ |
| $O^- + O_3 \rightarrow O_2 + O_2 + e^-$ | $3.020 \times 10^{-10}$ |
| $O^- + O_2(a^1\Delta_g) \rightarrow O_3 + e^-$ | $3.020 \times 10^{-10}$ |
| $O^- + O_2(b^1\Sigma_g^+) \rightarrow O_2 + O + e^-$ | $7.079 \times 10^{-10}$ |
| $O^- + e^- \rightarrow O + e^- + e^-$ | $3.981 \times 10^{-8}$ |
| $O_2^- + O \rightarrow O_3 + e^-$ | $3.020 \times 10^{-10}$ |
| $O_2^- + O_2 \rightarrow O_2 + O_2 + e^-$ | $3.020 \times 10^{-14}$ |
| $O_2^- + O_2(a^1\Delta_g) \rightarrow O_2 + O_2 + e^-$ | $1.995 \times 10^{-10}$ |
| $O_2^- + O_2(b^1\Sigma_g^+) \rightarrow O_2 + O_2 + e^-$ | $3.631 \times 10^{-10}$ |
| $O_3^- + O \rightarrow O_2 + O_2 + e^-$ | $1.000 \times 10^{-13}$ |
| $O_3^- + O_2 \rightarrow O_2 + O_3 + e^-$ | $1.000 \times 10^{-14}$ |
| $O_3^- + O_3 \rightarrow O_2 + O_2 + O_2 + e^-$ | $1.000 \times 10^{-12}$ |

Table 12: Electron detachment [18].

### 6.1.9 Ion-molecule reactions

Bimolecular reactions with negatively/positively charged species and third body reactions are presented in tables 13 and 14. In comparison to plasma mechanisms with fuel within the discharge zone, these schemes contain only relatively few simple charge transfer reactions. Some reactions of this type for the relevant species $O, O_2, O_3$ are listed below.

| **Reaction** | **Rate coefficient**, $[cm^{-3}/s]$ |
|---|---|
| $O^- + O_2 \rightarrow O + O_2^-$ | $1.000 \times 10^{-12}$ |
| $O^- + O_3 \rightarrow O_2 + O_2^-$ | $1.000 \times 10^{-11}$ |
| $O^- + O_3 \rightarrow O + O_3^-$ | $1.905 \times 10^{-10}$ |
| $O_2^- + O \rightarrow O_2 + O^-$ | $3.311 \times 10^{-10}$ |
| $O_2^- + O_3 \rightarrow O_2 + O_3^-$ | $3.981 \times 10^{-10}$ |
| $O_3^- + O \rightarrow O_3 + O^-$ | $1.000 \times 10^{-13}$ |
| $O_3^- + O \rightarrow O_2 + O_2^-$ | $3.236 \times 10^{-10}$ |
| $O_3^- + O_2 \rightarrow O + O_4^-$ | $3.981 \times 10^{-10}\ \mathrm{e}^{-52.0/RT_\mathrm{g}}$ |
| $O^+ + O_2 \rightarrow O + O_2^+$ | $1.905 \times 10^{-11}$ |
| $O^+ + O_3 \rightarrow O_2 + O_2^+$ | $1.096 \times 10^{-10}$ |
| $O_4^+ + O \rightarrow O_2^+ + O_3$ | $3.020 \times 10^{-10}$ |
| $O_4^+ + O_2 \rightarrow O_2^+ + O_2 + O_2$ | $1.585 \times 10^{-13}$ |
| $O_4^+ + O_2(a^1\Delta_g) \rightarrow O_2^+ + O_2 + O_2$ | $1.000 \times 10^{-10}$ |
| $O_4^+ + O_2(b^1\Sigma_g^+) \rightarrow O_2^+ + O_2 + O_2$ | $1.000 \times 10^{-10}$ |

Table 13: Ion-molecule reactions [18].

| **Reaction** | **Rate coefficient**, $[cm^{-3}/s]$ |
|---|---|
| $O^+ + O + M \rightarrow O_2^+ + M$ | $1.000 \times 10^{-30}$ |
| $O_2^+ + O_2 + O_2 \rightarrow O_4^+ + O_2$ | $2.399 \times 10^{-30}\ (T_\mathrm{g}/\mathrm{K})^{-1}$ |

Table 14: Ion-molecule reactions, third body reactions [18].

Comparing with Capitelli et al. [15], the authors implement this class of reactions in a very similar fashion. Notably, they moreover include reactions in table 15 as well as four processes with $O_4^-$ reactants.

| **Reaction** | **Rate coefficient**, $[cm^{-3}/s]$ |
|---|---|
| $O^- + O_2(a^1\Delta_g) \rightarrow O_2^- + O$ | $1.0 \times 10^{-10}$ |
| $O^- + O_2 + O_2 \rightarrow O_3^- + O_2$ | $1.1 \times (300\,\mathrm{K}/T)$ |
| $O_2^- + O_2 + O_2 \rightarrow O_4^- + O_2$ | $3.5 \times 10^{-30}(300\,\mathrm{K}/T)$ |

Table 15: Bi- and trimolecular ion-molecule reactions [15].

### 6.1.10 Recombination of charged particles

Recombination of oxygen species are given in tables 16 and 17.

| **Reaction** | **Rate coefficient**, $[\mathrm{cm}^{-3}/\mathrm{s}]$ |
|---|---|
| $O^- + O^+ \to O + O$ | $3.162 \times 10^{-7}$ |
| $O^- + O_2^+ \to O + O_2$ | $1.995 \times 10^{-7}$ |
| $O^- + O_4^+ \to O + O_2 + O_2$ | $1.000 \times 10^{-7}$ |
| $O^- + O_4^+ \to O_2 + O_3$ | $3.981 \times 10^{-7}$ |
| $O_2^- + O^+ \to O_2 + O$ | $7.079 \times 10^{-6}\ (T_\mathrm{g}/\mathrm{K})^{-0.5}$ |
| $O_2^- + O_2^+ \to O_2 + O_2$ | $4.266 \times 10^{-7}$ |
| $O_2^- + O_2^+ \to O_2 + O + O$ | $1.000 \times 10^{-7}$ |
| $O_2^- + O_4^+ \to O_2 + O_2 + O + O$ | $3.981 \times 10^{-7}$ |
| $O_3^- + O^+ \to O_3 + O$ | $1.995 \times 10^{-7}$ |
| $O_3^- + O^+ \to O_2 + O_2$ | $7.079 \times 10^{-6}\ (T_\mathrm{g}/\mathrm{K})^{-0.5}$ |
| $O_3^- + O_2^+ \to O + O + O_3$ | $1.000 \times 10^{-7}$ |
| $O_3^- + O_2^+ \to O_3 + O_2$ | $1.995 \times 10^{-7}$ |
| $O_3^- + O_2^+ \to O_2 + O_2 + O$ | $7.079 \times 10^{-6}\ (T_\mathrm{g}/\mathrm{K})^{-0.5}$ |
| $O_3^- + O_4^+ \to O_2 + O_2 + O_3$ | $3.981 \times 10^{-7}$ |
| $O_4^- + O^+ \to O_2 + O_2 + O$ | $1.000 \times 10^{-7}$ |
| $O_4^- + O_2^+ \to O_2 + O_2 + O_2$ | $1.000 \times 10^{-7}$ |
| $O_4^- + O_4^+ \to O_2 + O_2 + O_2 + O_2$ | $1.000 \times 10^{-7}$ |
| $O_4^+ + e^- \to O_2 + O_2$ | $1.000 \times 10^{-7}$ |

Table 16: Recombination of charged particles [18].

The recombination products of large species are generally not well understood, see Starikovskiy et al. [98]. Beyond the above list, we may consider the direct recombination dissociation process $O_2^+ + e^- \to O + O$, which is listed in [98] with a rate of $k = 2 \times 10^{-7}\,(300\,K/T)\,\mathrm{cm}^3/\mathrm{s}$.

| **Reaction** | **Rate coefficient**, $[\mathrm{cm}^{-3}/\mathrm{s}]$ |
|---|---|
| $O^+ + O_2 + e^- \to O + O_2$ | $1 \times 10^{-26}$ |
| $O^+ + e^- + M \to O + M$ | $9.333 \times 10^{-21}\ (T_\mathrm{g}/\mathrm{K})^{-2.5}$ |
| $O_2^+ + e^- + M \to O_2 + M$ | $9.550 \times 10^{-21}\ (T_\mathrm{g}/\mathrm{K})^{-2.5}$ |

Table 17: Recombination with electrons [18].

### 6.1.11 Diffusion to the wall and photoprocesses

For all excited species besides the dissociation intermediates, there are processes modeling diffusion to the walls. These are of the form

$$A^* + wall \to A + wall$$

and are discussed, for example, in [15]. In [13], it is argued that the diffusion losses of $O_2(b^1\Sigma_g^+)$ to the wall are expected to be weaker at low temperatures.

## 6.2 Helium and oxygen-helium plasma processes

The relevance of individual electron-oxygen reactions varies with the percentage of $O_2$ in the He mixture. In their paper "*Main Species and Physicochemical Processes in Cold Atmospheric-pressure* $He + O_2$ *Plasmas*" [59], Liu et al. distinguish between three parameter classes, depending on the initial oxygen concentration in a $He/O_2$ plasma system:

- 1-10 ppm oxygen: Helium species dominate the discharge, which is electropositive.
- 10-5000 ppm oxygen: Oxygen derived species dominate the discharge, which becomes increasingly electronegative.
- 0.5-10% oxygen: Exotic helium species are negligible, the discharge is electronegative.

Our concern is with a discharge falling in the last class. At percentages under 10%, elastic electron collisions are the most relevant processes to accurately describe the plasma chemistry. Here, the role of helium is thermal energy redistribution. Dissociative excitation and electron attachment become indispensable only for higher values [59], where heavier positively charged particles should be included in the reaction mechanism. The requirements for an accurate description also depend on the energy input. Adding many of the helium states is only necessary for low energy systems, where ionization can only occur stepwise. At the energies we consider, excited He states can be lumped together. At the least, the helium submechanism must describe the ionization and the interaction with the second most prevalent molecule, namely molecular oxygen. The species $He^*$ and $He(met)$ notably play the role of offering alternative channels for helium ionization. Those play a significant role in bridging the ionization energy barrier, see subsection 9.3, *Simulation of the pure helium system*. Due to the higher energy cost, the concentration of helium ions will generally be much lower than that of excited helium states. Due to the high helium mole fraction in our dilution, processes involving $He^+$ and $He_2^+$ together with $O_2$ appear to be of more immanent relevance than processes of charged oxygen with helium. Quenching by $O_2(a^1\Delta_g)$ should be less relevant within the zone of plasma generation, than in the post-discharge zone [105]. Meanwhile, the table of neutral molecule reaction 4 merely contains $O_2$ impact-dissociations by of helium species which in an energetically elevated state and the mechanism could be improved by considering reactions with excited species other than helium.

| **Reaction** | **Rate data** | **Type** |
|---|---|---|
| $He + e^- \leftrightarrow He + e^-$ | EEDF | elastic collisions |
| $He + e^- \leftrightarrow He^* + e^-$ | EEDF | excitation |
| $He + e^- \leftrightarrow He(met) + e^-$ | EEDF | excitation |
| $He + e^- \rightarrow He^+ + e^- + e^-$ | EEDF | ionization |
| $He(met) + e^- \rightarrow He^+ + e^- + e^-$ | EEDF | ionization |
| $He^* + e^- \rightarrow He^+ + e^- + e^-$ | EEDF | ionization |
| $He^* \rightarrow He + h\nu$ | $50\,s^{-1}$ \| 625 Å | photoprocesses |
| $He(met) \rightarrow He + h\nu$ | $78000\,s^{-1}$ \| 10828 Å | photoprocesses |
| $He^+ + He + He \rightarrow He_2^+ + He$ | $1.08 \times 10^{-31}\,cm^6 s^{-1}$ | attachment |

Table 18: Pure helium processes. [18].

| **Reaction** | **Rate coefficient**, $[\mathrm{cm}^3/\mathrm{s}]$ |
|---|---|
| $\mathrm{He}^* + \mathrm{O}_2 \rightarrow \mathrm{He} + \mathrm{O}_2$ | $5.8 \times 10^{-11}$ |
| $\mathrm{He}^* + \mathrm{O}_2 \rightarrow \mathrm{He} + \mathrm{O}(^1D) + \mathrm{O}$ | $4.0 \times 10^{-11}$ |
| $\mathrm{He}(met) + \mathrm{O}_2 \rightarrow \mathrm{He} + \mathrm{O}_2$ | $2.3 \times 10^{-10}$ |
| $\mathrm{He}(met) + \mathrm{O}_2 \rightarrow \mathrm{He} + \mathrm{O}(^1D) + \mathrm{O}$ | $3.4 \times 10^{-11}$ |
| $\mathrm{He}^* + \mathrm{O}_2 \rightarrow \mathrm{He} + \mathrm{O}_2^+ + \mathrm{e}^-$ | $2.7 \times 10^{-10}$ |
| $\mathrm{He}^* + \mathrm{O}_2 \rightarrow \mathrm{He} + \mathrm{O}^+ + \mathrm{O} + \mathrm{e}^-$ | $2.7 \times 10^{-10}$ |
| $\mathrm{He}(met) + \mathrm{O}_2 \rightarrow \mathrm{He} + \mathrm{O}_2^+ + \mathrm{e}^-$ | $1.1 \times 10^{-10}$ |
| $\mathrm{He}(met) + \mathrm{O}_2 \rightarrow \mathrm{He} + \mathrm{O}^+ + \mathrm{O} + \mathrm{e}^-$ | $1.1 \times 10^{-10}$ |
| $\mathrm{He}^+ + \mathrm{O}_2 \rightarrow \mathrm{He} + \mathrm{O}_2^+$ | $3.8 \times 10^{-10}$ |
| $\mathrm{He}^+ + \mathrm{O}_2 \rightarrow \mathrm{He} + \mathrm{O}^+ + \mathrm{O}$ | $6.2 \times 10^{-10}$ |
| $\mathrm{He}_2^+ + \mathrm{O}_2 \rightarrow \mathrm{He} + \mathrm{He} + \mathrm{O}_2^+$ | $3.9 \times 10^{-10}$ |
| $\mathrm{He}_2^+ + \mathrm{O}_2 \rightarrow \mathrm{He} + \mathrm{He} + \mathrm{O}^+ + \mathrm{O}$ | $6.2 \times 10^{-10}$ |

Table 19: Oxygen-helium interaction processes [18].

The plasma chemical kinetics of pure helium is presented in table 18. This scheme, together with table 19 of electron impact and photoprocesses as well as bimolecular and third body reactions, is an extension of the oxygen plasma scheme described in the previous subsection. It incorporates helium, excited helium states, as well as positively charged ions and photons. Associated cross section data is also found in [18]. The rates of the spontaneous radiation processes in table 18 were estimated using the *Kintech Khimera* software [17]. Those are determined by two values, namely the radiation coefficient $A$ and the wavelength $\lambda$, which are given in units of $\mathrm{s}^{-1}$ and Angstroms, respectively.

We are going to compare this list to the mechanism presented by Waskoenig et al. [107], which comprises 29 chemical reactions involving helium species in total, including some estimates concerning collision and production with $\mathrm{O}_2(a^1\Delta_g)$.

In reference to the simulation performed in [107], the O destruction processes presented in table 20 are emphasized and should be considered in the validation of $\mathrm{O}_2$/He mechanisms. Addition of the first reaction to our simulation will indeed turn out to be very significant for the atomic oxygen behavior in the helium bath. At $T_\mathrm{g} = 300\,\mathrm{K}$, the rate of $3.4 \times 10^{-46}\,\mathrm{m}^6\mathrm{s}^{-1}$ is twice as large as the rate of $\mathrm{O} + \mathrm{O}_2 + M \rightarrow \mathrm{O}_3 + M$ in the initial mechanism.

Table 19 does not contain so-called Penning ionization reactions $\mathrm{O}_2 + \mathrm{He}^* \rightarrow \mathrm{O}_2^+ + \mathrm{He} + \mathrm{e}^-$, in which excited heavy particles provide energy for creation of a pair of charged particles. In [43], the authors discuss how "helium meta-stables are predominantly quenched by Penning ionization with $\mathrm{O}_2$ over $\mathrm{O}_2(a^1\Delta_g)$, $\mathrm{O}_3$ and O interaction." The corresponding processes by Waskoenig et al. are given in tables 20 and 21.

| **Reaction** | **Rate coefficient** |
|---|---|
| $\mathrm{O} + \mathrm{O}_2 + \mathrm{He} \rightarrow \mathrm{O}_3 + \mathrm{He}$ | $3.4 \times 10^{-46}\,(300\,\mathrm{K}/T_\mathrm{g})^{1.2}\,\mathrm{m}^6\mathrm{s}^{-1}$ |
| $\mathrm{O} + \mathrm{O} + \mathrm{He} \rightarrow \mathrm{O}_2 + \mathrm{He}$ | $1.0 \times 10^{-45}\,\mathrm{m}^6\mathrm{s}^{-1}$ |
| $\mathrm{O} + \mathrm{O}_3 \rightarrow \mathrm{O}_2 + \mathrm{O}_2$ | $1.5 \times 10^{-17}\mathrm{e}^{-2250\,\mathrm{K}/T_\mathrm{g}}\,\mathrm{m}^6\mathrm{s}^{-1}$ |

Table 20: O destruction processes, [107].

| **Penning ionization with helium** | **Rate coefficient**, $[m^3/s]$ |
|---|---|
| $He^* + O_3 \rightarrow O_2^+ + O + He + e^-$ | $2.5 \cdot 10^{-16} \, (300\,K/T_g)^{-1/2}$ |
| $He^* + O_2 \rightarrow O_2^+ + He + e^-$ | $2.5 \cdot 10^{-16} \, (300\,K/T_g)^{-1/2}$ |
| $He^* + O \rightarrow O^+ + He + e^-$ | $2.5 \cdot 10^{-16} \, (300\,K/T_g)^{-1/2}$ |
| $He^* + O(^1D) \rightarrow O^+ + He + e^-$ | $2.5 \cdot 10^{-16} \, (300\,K/T_g)^{-1/2}$ |
| $He^* + He^* \rightarrow He_2^+ + e^-$ | $1.5 \cdot 10^{-15}$ |
| $He_2^* + He_2^* \rightarrow He + He + He_2^+ + e^-$ | $1.5 \cdot 10^{-15}$ |

Table 21: Possible Penning ionization reactions with gas temperature $T_g$ [107].

Waskoenig et al. [107] moreover include the following recombination and photon emission processes, in table 22.
Recombination reactions of the form $He^+ + e^- + M \rightarrow He + M$ are absent from the Waskoenig scheme.

| **Process** | **Rate coefficient**, $[m^3/s]$ |
|---|---|
| $He^+ + e^- \rightarrow He^* + h\nu$ | $8.9 \times 10^{-15} \, (T_g/T_e)^{-3/2}$ |
| $O^+ + e^- \rightarrow O(^1D) + h\nu$ | $4.7 \times 10^{-17} \, (T_e/K)^{-1/2}$ |

Table 22: Photoprocesses, [107]. Here $T_e$ denotes the electron temperature of the system.

# 7 Mechanisms for plasma assisted combustion

This work is about the effect of plasma treated $O_2$/He-mixtures on the combustion chemistry of hydrogen and methane. Due to quenching before mixing with the fuel (previously discussed in section 5), one cannot expect charged particles or very exotic particles in the combustion zone. More concretely, next to $O_2$ and He in the ground state, the species which survive in possibly relevant amounts are:

- Atomic oxygen (O) and ozone ($O_3$), which is formed in recombination processes.
- Electronically excited oxygen molecules $O_2(a^1\Delta_g), O_2(b^1\Sigma_g^+)$ and $O_2(4.5)$.
- Possibly electronically excited atomic oxygen $O(^1D)$.

We are particularly interested to know how the chemical reaction paths change when $O_2(a^1\Delta_g)$ and $O_2(b^1\Sigma_g^+)$ are involved. The atomic oxygen development is also crucial for plasma assisted combustion.

Since reactions involving $O_2$ and $H_2$ are also necessary for every combustion process involving methane or longer hydrocarbons, those combustion mechanism for plasma treated species can include reactions describing the interaction of excited oxygen with hydrogen. This is why, after some general remarks, we will start with a discussion of oxygen-hydrogen reaction mechanisms first and consider reactions with $CH_4$ in the following section 7.4.

## 7.1 Principal effect of plasma species on combustion kinetics

Additional net energy is stored and transferred spatially by excited states, which are generated in a discharge. Macroscopically, we understand how energy, inserted into the system, can simply thermalize and heat up the mixture. There are several plasma processes, which the zones involved in a setup for plasma assisted combustion can share. In our case, these are reactions involving only oxygen molecules, oxygen atoms as well as energy transfer processes like quenching, etc. Most have already been discussed in the previous sections. Here, we discuss the schemes of reactions that must be considered in the combustion zone.

To see a modification of chemical combustion pathways, we certainly want to investigate the reactions of type

$$O_2(a^1\Delta_g, b^1\Sigma_g^+) + A \leftrightarrow O_2 + A^*.$$

In this section, "A" shall denote any species or chemical group. Considering a reaction involving only oxygen species, an example of this scheme is the pooling reaction

$$O_2(a^1\Delta_g) + O_2(a^1\Delta_g) \leftrightarrow O_2 + O_2(b^1\Sigma_g^+),$$

which can give rise to $O_2(b^1\Sigma_g^+)$ whenever the lower states $O_2(a^1\Delta_g)$ are present. As has been noted, many reaction mechanisms in the literature actually do not employ $O_2(b^1\Sigma_g^+)$ at all. This can also be said about ozone and reactions such as

$$O_2(b^1\Sigma_g^+) + O_3 \leftrightarrow O_2(a^1\Delta_g) + O_2 + O.$$

A more general variation of the above scheme is

$$O_2(a^1\Delta_g, b^1\Sigma_g^+) + A \leftrightarrow A' + A''.$$

Many basic combustion processes, to be discussed below, have a pendant where oxygen in the ground state, $O_2$, is simply replaced by $O_2(a^1\Delta_g, b^1\Sigma_g^+)$. For example, the O-radical producing reaction

$$O_2(a^1\Delta_g, b^1\Sigma_g^+) + H_2 \leftrightarrow O + H_2O$$

is of this type.

As a first broad classification, the chemical chain reactions making up the combustion can be grouped into *initiation*, *branching* and *propagation* reactions. Any possible enhancement will have the most profound impact if it is concerned with rate limiting reactions and those are generally these involving stable species. The behavior of chain *termination* will also look different. *Quenching* and *recombination* processes are also still present in the fuel-oxidizer mixture and crucially affect the detailed chemistry. While quenching species with excited energy levels lead to a global temperature rise, they narrow the possibility for sophisticated flame enhancement by reactions involving excited species.

In the computational study of the effect of $O_2(a^1\Delta_g, b^1\Sigma_g^+)$ addition, one takes crucial reactions for the combustion mechanisms and compares the rates when $O_2$ is substituted by its electronically excited analogues. So for example, an important question is how the rate for the *initiation* reactions

$$O_2(X^3\Sigma_g^-, a^1\Delta_g, b^1\Sigma_g^+) + AH \rightarrow HO_2 + A$$

differ with respect to the $O_2$ state. Similarly, a dissociation or a process of the form

$$O_2(X^3\Sigma_g^-, a^1\Delta_g, b^1\Sigma_g^+) + A \rightarrow AO + O$$

generates reactive atomic oxygen and the rate of this reaction depends on the electronic energy level of the oxygen molecule. Other relevant reaction processes are discussed below, after a short review of the principles of the general combustion process. It should be noted that reactions with electronically excited reactants do not necessarily have a higher rate than their unexcited counterparts. For example, due to a different (higher) energy barrier, the rate of production of nitric oxide and atomic oxygen from reactants $O_2 + N$ exceeds the one from reactants $O_2(a^1\Delta_g) + N$ by a factor of $10^5$ [96].

## 7.2 Temperature rise in discharge- and combustion zone

If the discharge heats the gas significantly, much of the electric energy is not used for particle excitation and/or dissociation. The desired electrical energy fraction that goes into heating depends on the substances at hand, because a higher temperature accelerates combustion, while quenching rates are typically not strongly affected. For the present study, and for experiments on microscopic chemistry in general, excited particles are prefered over mere heat.
We are eventually interested in how the generated particles affect combustion in general

and must therefore also take a quantitative look on how the energy of the plasma species is actually converted when being mixed with the fuel. For this, it is necessary to keep in mind that in the combustion zone, particles resulting from excitation or dissociation might just as well "only" end up heating the gas and not enhance the flame by affecting specific pathways. Consider a process of production of radicals, as in

$$O + CH_4 \rightarrow CH_3 + OH$$

and an O-quenching reaction such as

$$O + O + M \rightarrow O_2 + M.$$

The design of a combustion system may take advantage of processes like the first, which generate reaction partners supporting particularly chosen reaction paths. The second reaction process is typically found in plasmas that in fact also support combustion. It is, however, less selective. In the latter case all reaction rates change due to a global parameter change. If the latter case dominates the system, one speaks of an improvement of the combustion "only via temperature effects." Again, note that this is an effect in the combustion zone and to be distinguished from the direct heating of the plasma in the electrical field.

## 7.3 Hydrogen combustion

### 7.3.1 On basic combustion mechanisms

Effectively, hydrogen combustion takes $H_2 + O_2$ to $H_2O$. Hence, in the ideal stoichiometric process each oxygen molecule is split into atomic oxygen, then reacts with hydrogen and forms water. However, in reality this is not as straight forward and the process only terminates with e.g. $H + OH + M \leftrightarrow H_2O + M$: In an initiation reaction, H is produced via $H_2 + O_2 \rightarrow H + HO_2$ and/or $H_2 + M \rightarrow H + H + M$ at high temperatures and this opens up the possibility for the branching $H + O_2 \rightarrow O + OH$. In this chain reaction step, the H radical is absorbed and two more radicals, O and OH, are produced. Further reactions are involved, such as $O + H_2 \leftrightarrow H + OH$ and $O + H_2O \leftrightarrow OH + OH$. At higher pressures, third partner reactions such as the chain terminating $H + O_2 + M \leftrightarrow HO_2 + M$ become relevant. Eventually, any reaction of the standard mechanism with $H_2O$ on one side has either H or OH on the other, see table 23. The OH radical is a main player in the propagation of the chain oxidation leading to ignition and is hence also the main indicator for the development of the flame. The path $H_2 + O_2 \leftrightarrow OH + OH$ followed by $H_2 + OH \leftrightarrow H_2O + H$ is also possible and emphasized in [74]. There, it is reported that the first reaction is the main channel for production of radicals at low temperatures.

Many accurate hydrogen combustion mechanisms exist. Two extensive comparative studies were performed very recently by Olm et al. [63] (2014) and Bezgin et al. [7] (2013). Further literature is provided by Gerasimov et al. [31] (2013). Table 23 provides the foundation for a hydrogen combustion mechanism and serves as background to understand the influence of plasma treatment of the oxidizer [106]. Small common additions to the reactions listed include $H + O + M \leftrightarrow OH + M$ or $H_2 + O_2 \leftrightarrow OH + OH$, among others. So for example,

we are going to study the proposed hydrogen combustion mechanism by Starik [95]. When comparing its non-excited base mechanism, we find that it consists exactly of the reactions presented above.

| Reactions without $HO_2$, $H_2O_2$ | Reactions without $H_2O_2$ | Other reactions |
|---|---|---|
| $O_2 + H \leftrightarrow OH + O$ | $H + O_2 + M \leftrightarrow HO_2 + M$ | $HO_2 + HO_2 \leftrightarrow H_2O_2 + O_2$ |
| $H_2 + O \leftrightarrow OH + H$ | $HO_2 + H \leftrightarrow OH + OH$ | $HO + HO + M \leftrightarrow H_2O_2 + M$ |
| $H_2 + OH \leftrightarrow H_2O + H$ | $HO_2 + H \leftrightarrow H_2 + O_2$ | $H_2O_2 + H \leftrightarrow H_2 + HO_2$ |
| $OH + OH \leftrightarrow H_2O + O$ | $HO_2 + H \leftrightarrow H_2O + O$ | $H_2O_2 + H \leftrightarrow H_2O + OH$ |
| $H + H + M \leftrightarrow H_2 + M$ | $HO_2 + O \leftrightarrow OH + O_2$ | $H_2O_2 + O \leftrightarrow OH + HO_2$ |
| $O + O + M \leftrightarrow O_2 + M$ | $HO_2 + OH \leftrightarrow H_2O + O_2$ | $H_2O_2 + OH \leftrightarrow H_2O + HO_2$ |
| $H + OH + M \leftrightarrow H_2O + M$ | | |

Table 23: Basic hydrogen combustion scheme.

### 7.3.2 Excited oxidizer effect on hydrogen combustion pathways

The important H-radical producing chain initiation reaction and its excited analogues

$$O_2(X^3\Sigma_g^-, a^1\Delta_g) + H_2 \rightarrow HO_2 + H$$

have been mentioned above (see also Bowman [14]). Then, the branching reactions

$$O_2(X^3\Sigma_g^-, a^1\Delta_g, b^1\Sigma_g^+) + H \rightarrow OH + O$$

are the next sensitive processes in the chain [65, 98]. As a quantitative example, let us consider the rates $k = A\,\mathrm{e}^{-E_a/T}$ of the above reaction for the ground state vs. the first excited state, as given by Popov [74]. With $A = 6.50 \times 10^{-11}\,\mathrm{cm^3 s^{-1}}, E_a = 2530\,\mathrm{K}$ and $A = 1.62 \times 10^{-10}\,\mathrm{cm^3 s^{-1}}, E_a = 7470\,\mathrm{K}$, respectively, we find the reaction of excited oxygen is faster by a factor of $0.4\,\mathrm{e}^{4940\,\mathrm{K}/T}$, which at $T = 300\,\mathrm{K}$ amounts to six orders of magnitude. In setting up a reaction scheme for the mentioned processes including electronically excited oxygen, one is also led to take variations into account in which excited species are amongst the reactants. Whether such new paths are possible depend on the energies of the reacting partners. The examples corresponding to the reactions above are

$$O_2(b^1\Sigma_g^+) + H_2 \leftrightarrow H + HO_2(A')$$

and

$$O_2(b^1\Sigma_g^+) + H \leftrightarrow OH + O(^1D).$$

The hydroperoxyl ground state $HO_2(X^2A'')$ (or $HO_2$ for short) and the electronically excited doublet $HO_2(A^2A')$ (or $HO_2(A')$) may also take part in electronic-electronic exchange with excited oxygen as well as further quenching. Reaction rates of those are studied and compared in [83, 94, 96] and the references therein.

Due to the different energies of the first two excited oxygen molecule levels, one must also take a look at channels that were of smaller importance before. Dissociative scattering processes with $O_2$ or $O_3$ generate more O-radicals, which enhance the chain. Moreover,

$$O_2(a^1\Delta_g, b^1\Sigma_g^+) + H_2 \rightarrow OH + OH$$

will have a higher rate than its common counterpart, see [14, 98]. The same can be true for $O(^1D)$, e.g. Popov [74] considers $O(^1D) + H_2 \rightarrow OH + H$.

The subtle interplay of chain branching reactions and the chain terminating reaction

$$H + O_2 + M \leftrightarrow HO_2 + M$$

in the context of singlet oxygen combustion is explained in a more recent paper by Starik [95]. Here, a full hydrogen mechanism incorporating plasma treated oxidizer species is presented and subsequently applied to the simulation of a $H_2$-air scramjet combustion experiment at a pressure of $p = 0.3$ bar, an air temperature of $T = 300$ K and a discharge with an $E/n$ of 50 to 100 Td. The mechanism contains a total of 58 bidirectional reactions, 20 of which form the basic $H_2$-combustion core described above, and 32 containing $O_2(a^1\Delta_g), O_2(b^1\Sigma_g^+), O(^1D)$ or several of those at once, and possibly involving $O_3$. There are finally 6 reactions describing dissociative reactions of ozone $O_3$ with ground state species having low or no barrier. It includes quenching reactions, from $O_2(b^1\Sigma_g^+)$ down to $O_2(a^1\Delta_g)$ and also from $O_2(a^1\Delta_g)$ down to $O_2$, with all unexcited species.
Smirnov et al. [84] discuss a reaction mechanism in the context of an experiment on excited hydroxyl detection. The hydrogen-oxygen scheme contains $O_2(a^1\Delta_g)$, $O(^1D)$ and the $OH^*(A^2\Sigma^+)$ particle (9 reactions). Even $O_2(a^1\Delta_g) + H_2 \rightarrow H_2O + O(^1D)$ made it into these schemes. This hydrogen-oxygen system, also used by Bourig for the previous experiments in Magdeburg [13], generally differs significantly from the mechanisms found in Starik's more recent work, for example.

Above, we have now described complicated reactions, which are not mere quenching reactions or energy transfer processes between. The ratios of quenching rates and the rates of reactions taking part in combustion initiation and branching are of utmost importance and still in discussion for many reactants. The $O_2$-$H_2$ system presented by Starik [95] extends a basic scheme (see previous subsection) with about 45 reactions, half of which are quenching processes $A^* + B \rightarrow A + B$ where $A^*$ is $O_2(a^1\Delta_g)$, $O_2(b^1\Sigma_g^+)$ or $O(^1D)$. This particular paper discusses $O_2(b^1\Sigma_g^+) + H_2 \leftrightarrow O_2(a^1\Delta_g) + H_2$ in detail. Besides quenching reactions among oxygen species, Bowman [14] emphasizes $O_2(a^1\Delta_g) + H \rightarrow O_2 + H$ and $O_2(a^1\Delta_g) + HO_2 \rightarrow O_2 + HO_2$. In the high pressure limit, one can compare the quenching rates for different species in oxygen [65] and they are, from strongest to weakest, $O, O(^1D), O_2(v), O_2(b^1\Sigma_g^+), O_2(a^1\Delta_g)$. In this work, O and $O_3$ are cited to be particularly strong quenchers of $O_2(a^1\Delta_g)$.

## 7.4 Methane combustion

### 7.4.1 On basic combustion mechanisms

In comparison with the ignition process of the hydrogen system, for methane the longer reaction chains soon become much more complicated e.g. from $CH_4$ down to CH or up to $C_2H_6$. While the standard hydrogen oxidation mechanisms hardly ever exceed a few dozen reactions, a standard scheme capable of describing methane combustion contains several hundred (GRI-Mech 3.0, [32]: *53 species, 325 reactions*, mechanism by Konnov [48]: *127 species, 1207 reactions*, mechanism by Curran et al. [23]: *118 species, 1302 reactions*).

Let us mention a few initial processes involving molecular oxygen: The obvious sensitive initiation reaction for the system is

$$CH_4 + O_2 \rightarrow CH_3 + HO_2,$$

and this will be followed by

$$CH_3 + HO_2 \rightarrow CH_3O + OH.$$

Furthermore $CH_3$ can also react with $O_2$ again, to form either $CH_3O + O$, $CH_2O + OH$ or $CH_4O_2$. All of these reactions have analogues involving $O_2(a^1\Delta_g, b^1\Sigma_g^+)$. For the methane fuel, the species $H, OH, HO_2, H_2O_2$ play an important role in the combustion chain. Larger species can be produced in $CH_3 + CH_3 + M = C_2H_6 + M$, which raises the temperature, but effectively delays ignition. For a more elaborated treatment of this standard system without nitrogen and at pressures above one atmosphere, see Curran [23].

### 7.4.2 Excited oxidizer effect on methane combustion pathways

In the recent paper, Lebedev et al. [54] review the progress on $CH_4$/air-theory with focus on $CH_3$ interaction with excited oxygen oxidation. The purpose of the publication is then to compute rates of channels for $O_2(a) + CH_3$ and to discuss their role for hydrocarbon oxidation pathways at temperatures up to 900 K. Those processes involving $O_2(a^1\Delta_g, b^1\Sigma_g^+)$ are:

- Chain propagation reaction: $CH_3 + O_2(a^1\Delta_g, b^1\Sigma_g^+) \rightarrow CH_3O + O$.
- Chain propagation reaction: $CH_3 + O_2(a^1\Delta_g) \rightarrow CH_2O + OH$.
- Chain termination reaction: $CH_3 + O_2(a^1\Delta_g) \rightarrow CH_3O_2$.
- Excited oxygen quenching reaction: $O_2(b^1\Sigma_g^+) + CH_4 \rightarrow O_2(a^1\Delta_g) + CH_4$.

The group notes that with respect of singlet oxygen combustion, especially at atmospheric pressures, the $CH_4$ mechanism for plasma assisted oxidation proposed by Starik [94] is the currently most developed and comprehensive one available. Here, again, many reactions are indeed variations of processes with $CH_3$. Broad parameter studies of a predecessor mechanism have previously been performed [93]. In another paper by Starik [94], excitations of intermediate species in the context of a supersonic atmospheric pressure combustion experiment simulations are discussed. One focus is the production of excited hydroperoxyl, as in $CH_4 + O_2(b^1\Sigma_g^+) \leftrightarrow CH_3 + HO_2(A')$, and various vibrationally excited species. However, among electronically excited species, only singlet oxygen reactions are part of the lists of reactions found most important for combustion initiation, due to quenching. Regarding collisions by $O_2$ vs. $O_2(a^1\Delta_g)$, the rates of $HO_2$ production from methane at low temperatures appear to differ by an order of 4 [96].

Lebedev et al. conclude that an inaccuracy of 5 kcal/mole in the energetic parameters for a reaction in the considered regime may change the rate by an order of magnitude. The

reaction from $CH_3$ and $O_2(X^3\Sigma_g^-, a^1\Delta_g)$ to $CH_3O_2$ or excited $CH_3O_2(A')$ is classified to be chain terminating, but note that it also comes with a high energy release, which leads to temperature increase and hence combustion intensification. Also here, the difference of rates for considering unexcited vs. excited reactants differ by orders of magnitude, especially at lower temperatures [96]. Excited particle reactions are usually much faster.
Other temperature increasing reactions are $CH_3 + H + M \rightarrow CH_4 + M$ and $CH_3 + O_2 + M \rightarrow CH_3O_2 + M$. It is concluded that flame speed and flammability can be noticeably enhanced.

In [98], the authors review plasma assisted methane combustion in a wider context (and not necessarily at elevated pressures). The possible reactions leading to $CH_2$ would be $CH_3 + M \rightarrow CH_2 + H + M$ or $CH_3 + O \rightarrow CH_2 + OH$, but they appear not as relevant as the chain propagation reaction with $CH_3$. They further state that for hydrocarbons, the quenching can be much worse than for $H_2$, especially at high temperatures. For heavier fuel species in particular, it is reported that hydrogen quenching of $O_2(a^1\Delta_g, b^1\Sigma_g^+)$ is more effective than competing reactive channels, e.g. $O_2(a^1\Delta_g) + C_2H_4 \rightarrow C_2H_3O + OH$ for ethylene.

In the study by Ombrello et al. [64], it is found that $O_2(a^1\Delta_g)$ enhances the propagation of the flame. However, it's noted that quenching $C_2H_4 + O_2(a^1\Delta_g) \rightarrow C_2H_4 + O_2$ is considerably higher than the reactive channel $C_2H_4 + O_2(a^1\Delta_g) \rightarrow C_2H_3O + OH$.

The rate of $O_2(a^1\Delta_g)$ quenching by methane at 300 K was measured [5] to be $8.4 \times 10^5\, cm^3/mol/s$. Conversely, theoretical considerations (see [96] for a summary) predict that the production channel of $H_2O_2$ for $O_2(a^1\Delta_g)$ collision with $C_2H_6$ at high temperatures actually exceeds that of the quenching channel. Little is known about reactions with $C_2H_5$.

# Part III

# Model development and simulation

## 8 Modeling approach

We are now concerned with the development of an appropriate simulation model. Based on the physical parameters of the described experimental setup, we can make several crucial approximative calculations to estimate energy and time scales. Moreover, simple preliminary simulations are performed which reflect the qualitative behavior of the system under consideration. In the next section, the chosen approach is validated against available literature experiments.

### 8.1 Available data and principal approach

The experiment is designed to generate electronically excited species $O_2(a^1\Delta_g, b^1\Sigma_g^+)$ within an oxidizer and to investigate the combustion process with a hydrogen and/or methane fuel. The setup can be divided in the following three parts:

1. The $O_2$/He-mixture at room temperature is led through a high frequency pulse discharge chamber to produce the conditions for molecular oxygen excitation at atmospheric pressures.
2. The plasma treated mixture then leaves the discharge zone through a tube, which must be constructed sufficiently short, so that a relevant $O_2(a^1\Delta_g, b^1\Sigma_g^+)$ mole fraction remains.
3. Finally, the plasma from the tube meets another unprocessed fuel-oxygen mixture (either involving $CH_4$ or $H_2$) in a co-flow configuration and the whole partially-premixed gas is burned.

Different simulations are characterized by their input species concentrations $[c_i]$, flow rates $q_i$ and, from a computational perspective are accompanied by long lists of thermodynamical data and transport data for all species and chemical kinetics data, such as cross sections and reaction rates, for all chemical processes. Given accurate reaction mechanisms, the combustion and flame simulation is well understood and thus a straight forward task. The burner zone can be split into a mixing zone and a flame zone, figure 10. A local mixing of fuel and oxidizer will be assumed in the simulations. A spatially high dimensional simulation of the non-equilibrium kinetics is computationally extremely difficult and our computational models are therefore restricted to zero dimension. The discharge geometry determines crucial quantities in the electrical circuit and the particle dynamics, as explained in subsection 2.3 on the Boltzmann equation.

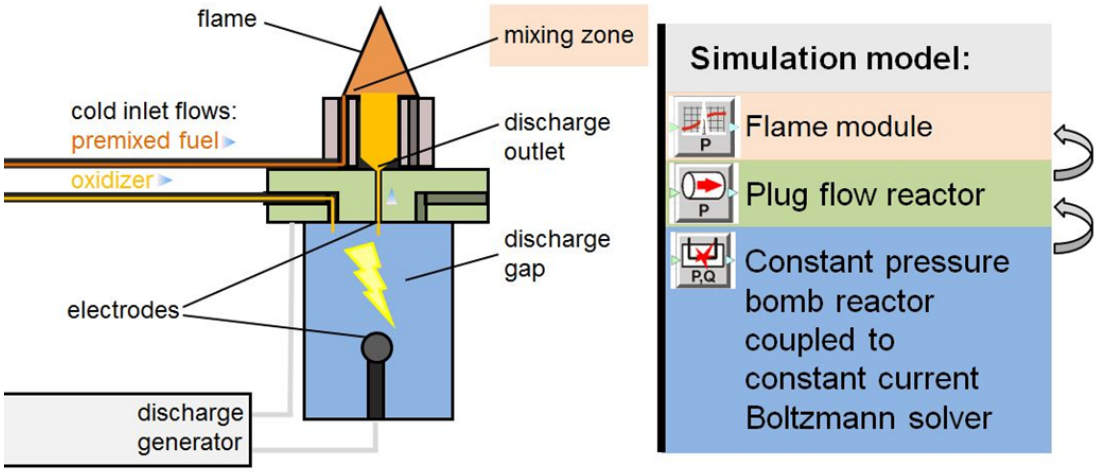


Figure 10: Experiment and associated computational model for the plasma discharge.

Table 24 is an overview of all specifications of the experiments performed in Magdeburg, which can be of relevance for the modeling. It must be noted that for this experiment, data like the discharge gap distance only provide the possibility for a simplified model of the actual discharge geometry and this will be reflected in the simulation result. The experiment at Bochum university (section 4.1.3), with its rectangular geometry, is easier to represent computationally.

| **Parameter** | **Value** |
|---|---|
| Initial temperature | $T_{\text{init}} = 300\,\text{K}$ |
| Pressure | $p = 1\,\text{atm}$ |
| Typical input concentration ratios | $O_2 : He = 1 : 30 \,\vert\, 1 : 15.\dot{6} \,\vert\, 0 : 1$ |
| Flow rate, oxidizer channel | $q \approx 0.31\,\text{m}^3/\text{h}$ |
| Temperature rise, 7 mm after tube | up to $\Delta T \approx 440\,\text{K}$ at 100% d.c. |
| Pulse frequency | $f_0 = 1.176\,\text{MHz} \approx 1\,\text{MHz}$ |
| Current, working mode | $I_d \approx 875\,\text{mA}$ |
| Voltage amplitude in limit mode | $U_d \approx 1\,\text{kV}$, sinodial |
| Voltage amplitude at breakdown | $U_d^{\max} \approx 12\,\text{kV}$ |
| Current cross section | $A_{I_d} < 2\,\text{cm}$ |
| Discharge gap | $d = 1.1\,\text{cm}$ |
| Discharge diameter | $D = 1.58\,\text{cm}$ |
| Discharge cross section | $A = (D/2)^2\,\pi \approx 2\,\text{cm}^2$ |
| Discharge volume | $V \approx 6\,\text{ml} \mathrel{\widetilde{=}} 6\,\text{cm}^3$ |
| Length of first tube (green) | $l_1 = 14\,\text{mm}$ |
| Radius of first tube (green) | $\mathfrak{r}_1 = 1.5\,\text{mm}$ |
| Length of second tube (orange) | $l_2 = 25\,\text{mm}$ |
| Radius of second tube (orange) | $\mathfrak{r}_2 = 6.5\,\text{mm}$ |

Table 24: Experimental data.

## 8.2 Power input and consumption

The heat $Q_{\text{molar}}$ of the post-discharge mixture is determined by the heat capacity and the observed temperature rise

$$Q_{\text{molar}} = C_p^{\text{He/O}_2} \cdot \Delta T.$$

For $\Delta T = 440\,\text{K}$ and after conversion of the flow rate into mol over time we find $Q_{\text{molar}} = 9\,\text{kJ/mol}$ or $0.1\,\text{eV}$ per molecule. We can estimate the power consumption by

$$P_{\text{abs}} = Q_{\text{molar}} \cdot q$$

and find

$$\frac{P_{\text{abs}}}{\Delta T} = 8 \times 10^{-2}\,\text{W/K},$$

i.e 8 Watts per temperature rise of 100 K. For $\Delta T = 440\,\text{K}$ this corresponds to

$$P_{\text{abs}} \approx 35\,\text{W}.$$

For sinodial currents and voltage in phase, we can compute the input power of the discharge as follows:

$$P_{\text{inp}} = \frac{1}{T}\int_0^T U_d(0)\cos(t) \cdot I_d(0)\cos(t)\,\mathrm{d}t = \tfrac{1}{2}\,U_d(0)\,I_d(0).$$

No significant phase shift could be observed in the Magdeburg experiment. In limit mode at full duty cycle and for 3.2% oxygen in helium, the voltage and current amplitudes are measured to be about $U_d(0) = 1000\,\text{V}$ and $I_d(0) = 875\,\text{mA}$, respectively, resulting in a power of $P_{\text{inp}} = 437.5\,\text{W} = 12.5\,P_{\text{abs}}$. In view of the study in the foregoing experimental section, such a discrepancy was to be expected. For comparison, recall that Ellerweg et al. [25] provide a loss factor estimate of $\eta = \frac{1}{20}$. As the voltage measurement is well trusted, the conclusion is that almost one Ampere is a significant overestimate for the current $I_d$ in the discharge zone. Indeed, as is explicated in [88], "it should be noted that only a small fraction of the generator power is actually coupled into the plasma, as there are losses in the connecting cables, matching network, and heating of the electrodes, as well as by RF-radiation of the jet device acting as antenna." This is also discussed in more detail by Law et al. [58].

As an aside, given the significant observed undesired temperature rise of several hundreds of Kelvin, it is clear that the actual current is still too high for the goal of delivering electrical energy mostly into particular oxygen excitation levels. Instead, the translational degrees of freedom are excited as well.

## 8.3 Residence times

For the following general considerations we assume simple pipe geometries where $V$ denotes volume, $A$ the constant cross section and $l := V/A$ is the corresponding length. As discharge geometry and real flow profile in the discharge zone are very complex, the interaction time of gas and field zone is not accurately known. The spatially zero dimensional simulation codes of the discharge zone are not sensitive to the flow velocity $v$ or the volumetric flow rate $q := v\,A$. Hence, the discharge simulation ignores physicochemical effects of flow rate variation, such as a resulting change of back diffusion rates of ambient gas into the post-discharge tube. Nevertheless, if $q_0, v_0$ are the initial flow rate resp. velocity, then $\tau_0 := l/v_0 = V/q_0$ is the first order approximation of the residence time. Table 25 provides various relevant characteristic quantities which can be computed from table 24.

The experiments are performed in the open laboratory and the relatively small flow velocities cannot affect the pressure, which is hence approximately constant at $p = 1\,atm$. We can use this to make estimates that also take the continuous temperature rise into account, which is governed by the chemical kinetics.
In the discharge zone, if the temperature rise/input power is constant, the increase of velocity is linear in time. Denote the constant acceleration by $\frac{\Delta v}{\tau}$. The traveled path of particles is given by the time-integral over their velocities and so the length interval corresponding to the residence time $\tau$ is $\int_0^\tau \left(v_0 + \frac{\Delta v}{\tau} t\right) \mathrm{d}t = \tau\, v_0\, (1 + \frac{1}{2}\Delta v/v_0)$.
The density is given by the ideal gas law $n = p/RT$ and hence fully determined by the temperature $T$. The continuity equation dictates that the mass flow rate $\dot{m} = m\,n\,v\,A$ is conserved, implying $v/T$ is constant and any temperature rise $\Delta T$ implies velocity change via $\Delta v/v_0 = \Delta T/T_0$. We find that two different temperature rises $\Delta T, \Delta T'$ lead to residence time $\tau, \tau'$, which are connected via $\tau = \tau' \cdot \frac{T_0 + \frac{1}{2}\,\Delta T'}{T_0 + \frac{1}{2}\,\Delta T}$.
The gas inlet temperature in the experiment is always $T_0 \approx 300\,\mathrm{K}$. If, for example, at 100% duty cycle we have a temperature rise of $\Delta T \approx 600\,\mathrm{K}$ in the discharge zone, the naive residence time $\tau_0$ will be shortened by a factor of $\frac{1}{2}$. In any case, the gas will witness several thousands of repetition forms. This is a comparatively big number, due to the fact that the volume is large for plasma experiments of this kind. The energy input into the system should correlate essentially linearly with the residence time. A long residence time puts emphasis on the description of the evolution of species, in the discharge gap, as opposed to the very complicated phenomenology during the short breakdown phase.

| **Characteristic quantity** | **Computed value** |
|---|---|
| Oscillation pulse duration | $\tau_{f_0} := 1/f_0 \approx 0.85 \times 10^{-6}\,\mathrm{s} \approx 1\,\mu\mathrm{s}$ |
| Repetition form duration | $\tau_{f_{\mathrm{rep}}} := 1/f_{\mathrm{rep}} = 50\,\mu\mathrm{s} = 50\,\tau_f$ |
| Naive discharge residence time | $\tau_0 := V/q_0 \approx 0.052\,\mathrm{s} = 52\,\mathrm{ms} \approx 6.12 \times 10^4\,\tau_f$ |
| Tube cross section | $A' := r^2\pi \approx 7.07\,\mathrm{mm}^2 \approx 7.07 \times 10^{-6}\,\mathrm{m}^2$ |
| Tube flow velocity | $v' := q/A = 12.18\,\mathrm{m/s}$ |
| Estimated tube residence time | $\tau_l := l/v' \approx 1.15\,\mathrm{ms}$ |
| Estimated diffusion time | $\tau_{\mathrm{diffusion}} := (q/2.4)^2/D \approx 0.1$ to $1\,\mathrm{s}$ |

Table 25: Flow data estimates.

## 8.4 Oxygen species relaxation time estimates

A bimolecular reaction of species A in a bath of species B is associated with a rate equation

$$\frac{\partial}{\partial t}[\mathrm{A}] = -k\,[\mathrm{A}]\,[\mathrm{B}] = -\frac{1}{\tau}[\mathrm{A}]$$

where $\tau := \frac{1}{k\,[\mathrm{B}]}$ is a characteristic decay time. It is useful to express the concentrations in terms of their partial mole fractions x, e.g. $[\mathrm{B}] = \mathrm{x_B} \cdot [M]$, where at standard conditions ($T = 293\,\mathrm{K}$, $p = 1\,\mathrm{atm}$) the ideal gas law predicts a mean concentration of $[M] \approx 2.5 \times 10^{19}\,\mathrm{cm}^{-3}$. So, the characteristic decay times can be written as

$$\tau(k, \mathrm{x}) := \frac{1}{k \cdot \mathrm{x} \cdot [M]}.$$

For example, consider a rate coefficient of de-excitation of $\mathrm{He}^*$ in collisions with $\mathrm{O_2}$ is given by $k \sim 4 \times 10^{-10}\,\mathrm{cm^3 s}$ and assume a mixture with a $\mathrm{O_2}$ portion of 6%, i.e. $x_{\mathrm{O_2}} = 6 \times 10^{-2}$. Then

$$\tau \approx \frac{10^{10+2-19}}{4 \times 6 \times 2.5}\,\mathrm{s} \approx 1\,\mathrm{ns}.$$

This time scale is even below that of a micro-discharge and so we cannot expect to see a relevant amount of excited helium surviving the discharge zone.

Table 26 shows several time estimates at $T = 300\,\mathrm{K}$ and using the mechanisms explicitly discussed in the second part of this work. For the discharge zone (third column) $\mathrm{O_2}$, O and $\mathrm{O_3}$ fractions of 6%, 0.5% and 1% have been used, while in the burner zone (fourth column) those numbers were 70%, 0.1% and 0.2%. It is revealed that most considered decay times are shorter than the previously estimated upper bound on the residence time of $\approx 5 \times 10^{-2}\,\mathrm{s}$. The table shows the data for the de-excitation as well as recombination of the plasma discharge. The longer characteristic times for atomic oxygen suggest that this species should dominate over generation of molecular oxygen excitation. Ozone or excited helium will play a small role in the composition of the discharge outlet. The eventual net quantities depend on the production rates, specifically $\mathrm{O_2} + \mathrm{e^-} \to \mathrm{O_2}(a^1\Delta_g, b^1\Sigma_g^+) + \mathrm{e^-}$ and $\mathrm{O_2} + \mathrm{e^-} \to \mathrm{O} + \mathrm{O} + \mathrm{e^-}$. A simple preliminary simulation of the system's response to a constant electric field pulse, taking into account the whole range of relevant $\mathrm{O_2}$/He reactions studied in the discussion of plasma discharge mechanism for our condition, will give a more accurate picture. This will be presented in the next part.

| **Process** | **Approx. rate**, [$\mathrm{cm^3/s}$] | **Char. time**, [s] | |
|---|---|---|---|
| $\mathrm{He}^* + \mathrm{O_2} \to \mathrm{O}^* + \mathrm{O} + \mathrm{He}$ | $3.4 \times 10^{-11}$ | $2.0 \times 10^{-8}$ | |
| $\mathrm{He}^* + \mathrm{O_2} \to \mathrm{He} + \mathrm{O_2^*}$ | $4.0 \times 10^{-10}$ | $1.5 \times 10^{-9}$ | |
| $\mathrm{O_2^*} + \mathrm{O_2} + \mathrm{O} \to \mathrm{O_2} + \mathrm{O_2} + \mathrm{O}$ | $1.0 \times 10^{-31}$ | $5.0 \times 10^{-5}$ | $2.0 \times 10^{-5}$ |
| $\mathrm{O_2^*} + \mathrm{O_3} \to \mathrm{O_2} + \mathrm{O_2} + \mathrm{O}$ | $5.0 \times 10^{-11}\,\mathrm{e}^{-5.7\,\mathrm{K}/T}$ | $1.0 \times 10^{-3}$ | $5.0 \times 10^{-3}$ |
| $\mathrm{O} + \mathrm{O} + M \to \mathrm{O_2} + M$ | $3.3 \times 10^{-31}\,\mathrm{K}/T$ | $2 \times 10^{-4}$ | $1.2 \times 10^{-3}$ |
| $\mathrm{O} + \mathrm{O_2} + M \to \mathrm{O_3} + M$ | $9.6 \times 10^{-34}$ | $2 \times 10^{-6}$ | $2.0 \times 10^{-6}$ |
| $\mathrm{CH_4} + \mathrm{O} \to \mathrm{CH_3} + \mathrm{OH}$ | $1.7 \times 10^{-10}\,\mathrm{e}^{-10.2\,\mathrm{K}/T}$ | | $2.0 \times 10^{-2}$ |
| $\mathrm{CH_4} + \mathrm{O_2}(a^1\Delta_g) \to \mathrm{CH_3} + \mathrm{OH}$ | $5.0 \times 10^{-18}$ | | $2.0 \times 10^{-2}$ |
| $\mathrm{CH_4} + \mathrm{O_2}(b^1\Sigma_g^+) \to \mathrm{CH_3} + \mathrm{OH}$ | $7.0 \times 10^{-14}$ | | $2.0 \times 10^{-6}$ |

Table 26: Characteristic times for discharge- and burner zone (third, resp. fourth column).

## 8.5 Physics in the post-discharge zone

A small tube of length $l_1 = 14\,\mathrm{mm}$ and radius $\mathfrak{r}_1 = 1.5\,\mathrm{mm}$ follows the discharge chamber, followed by an expansion zone into a larger second tube of length $l_2 = 25\,\mathrm{mm}$ and radius $\mathfrak{r}_1 = 6.5\,\mathrm{mm}$. Those are depicted by the green and orange area in figure 10. As the diffusion rate to the walls (table 25) is significantly smaller than the residence time, a simple plug flow reactor model is an accurate simulation tool. The sudden expansion of the cross section $A = \mathfrak{r}^2\,\pi$ along the flow direction $x$ in the second tube can be approximated by a polynomial. If $n$ is any large integer, a good fit for the radius $\mathfrak{r}(x)$, which varies from $\mathfrak{r}_1$ to $\mathfrak{r}_2$, is given by

$$\mathfrak{r}(x)^2 = (\mathfrak{r}_1^2 - \mathfrak{r}_2^2) \cdot \left(1 - \frac{x}{l_2}\right)^{2n} + \mathfrak{r}_2^2.$$

As species thermalize, the net temperature of the system in the naive simulation must go up. In reality, there are cooling effects. The plug flow cylinder surfaces differ by a factor of $(l_2\,\mathfrak{r}_2)/(l_1\,\mathfrak{r}_1) \approx 7.7$, so the heat loss rate $\dot{Q}$ in the first tube will be negligible compared to the second one. It is given by $\dot{Q} = h\,A'\,\Delta T$, so $Q = h\,A'\,\int_0^\tau \Delta T\,\mathrm{d}t$, where $h$ is a heat transfer coefficient and $A'$ is the heat transfer surface area.

## 8.6 Reduced electrical field and simulation tools

A characteristic quantity of a plasma discharge is the reduced electrical field $E/n$, which is typically given in units of Townsend $10^{17}\,\mathrm{Td} = \mathrm{V}\cdot\mathrm{cm}^2$. Its strong temperature dependence can be estimated by combining the first-order field-voltage relationship $E \approx U_d/d$ with the ideal gas law $n = p/k_B T$:

$$10^{17}\,\frac{E}{n} \approx 10^{17}\,\frac{k_B T \cdot U_d}{p \cdot d} = 1.2 \times 10^{-5}\,(T \cdot U_d)\,\mathrm{K}^{-1}\mathrm{V}^{-1}\mathrm{Td}.$$

For a voltage of thousand volts, this gives 1.2 Td per hundred Kelvin. Hence, in the range between 300 K and 900 K, we expect a field of 3.6 Td to 10.8 Td. This estimated field value in the limit mode is relatively low, but the high 12.5 kV amplitude at breakdown, corresponding to 40 Td, suffices for initiation. Recall the explanation in subsection 3.5 of how the chemical constitution of the plasma affects circuit resistance and electrical field.

The minimal required field strength for voltage breakdown can qualitatively be predicted in a very simple simulation: For this, one considers a gaseous mixture including a tiny seed of charged particles in a zero-dimensional reactor and suspends it to a constant electrical field. Breakdown is guaranteed, if the chain of ionization is observed before the charges recombine. The results of this test as shown in figure 11 for the 1 : 30 oxygen-helium mixture using the electron chemistry are discussed in the previous chapter [18]. The field at which breakdown occurs within one microsecond is found to be $E/n = 25\,Td$. When the equivalent simulation is performed for pure helium, no oxygen molecules can be ionized and the required field strength is higher. It is also customary to use the simple electrical field pulse model to probe the different electron collision channels of a fixed mixture of interest. The result for our system was already shown in figure 3. While the energy transfer into elastic collision processes (not shown) consumes the bulk of energy, a relevant amount of energy can also be

seen to be distributed into excitation of electrical particles. At about 15 Td, the energy spent for dissociation through the intermediate $O_2(B^3\Sigma_u^-)$ exceeds the excitation to $O_2(a^1\Delta_g)$.

The most elaborate Boltzmann module currently available in the *Chemical Work* software package is the realization of the *"UCLR model"*. Its input is a time dependent voltage form from which the electron energy distribution function, and in turn the electrical current, is computed. Preliminary simulation experiments have shown that this module cannot be capable of reflecting the chemistry of a current stabilized discharge. The current computed using an accurate modeling of the voltage wave forms decays exponentially. The appropriate module will hence be the *"constant current model"*, which however neglects individual oscillations. In the simulation of the discharge zone, several possible currents and their effects on the species concentrations must be considered and for each value $I_d$, the simulated temperature rise must be matched with the observation. From a computational perspective, this energy input is therefore the principal input data specifying the system, leading to computed species concentrations and, in turn, effect on flame speed.

A word of caution: Recall that change of the species ratio leads to different discharge gap resistances $R$, which are related to the electrical power via $P = R\,I^2$. Thus, in the constant current model, keeping the current (density) fixed while varying the input flow results in different power draw, affecting chemistry and temperature rise in the plasma.

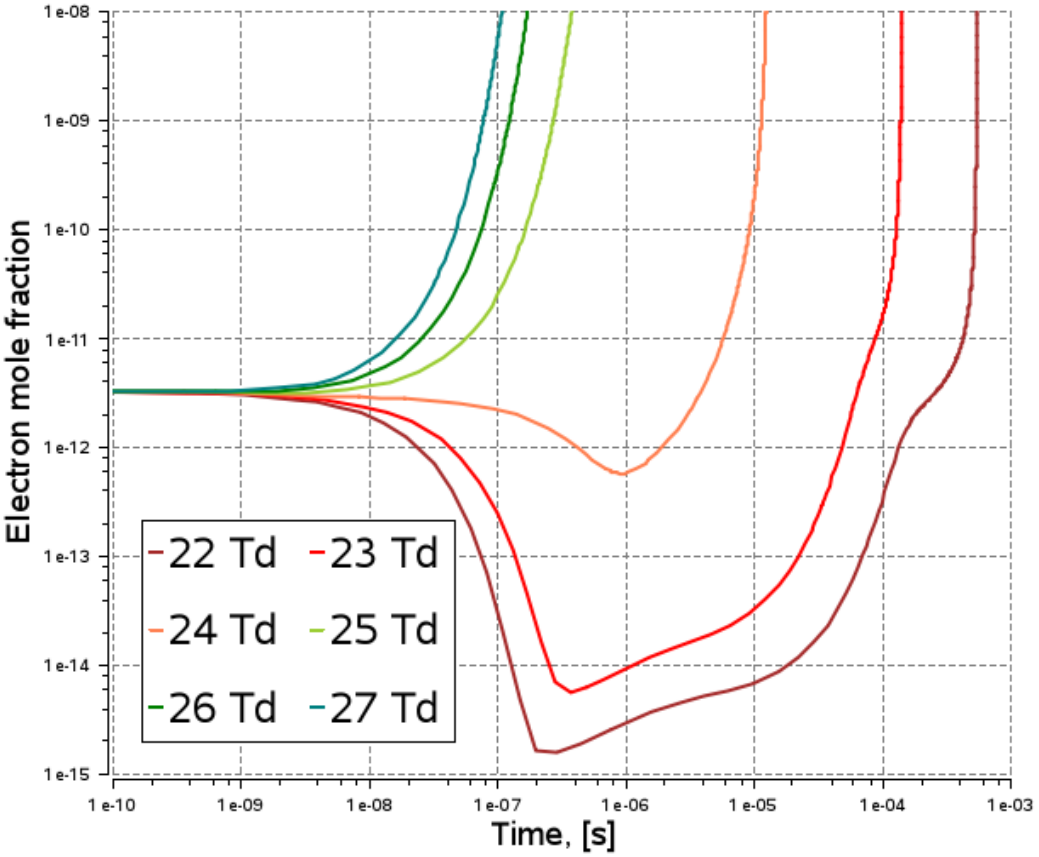


Figure 11: Varying values of $E/n$ for a species ratio of $O_2$ : He = 1 : 30.

# 9 Mechanism validation

## 9.1 Simulation approach

We are going to simulate the system [25], which has been described at length in section 4.1.3. The fixed parameter specifications for the plasma modules are summarized in table 27. The substance fraction of He : $O_2 = 100 : 0.6$ is the sweet-spot described in the paper and acts as base value for our studies. The flow rate of $\sim 0.09\,\mathrm{Nm^3/h}$ enters the simulation in terms of the residence time, which can be estimated from the other data. The discharge current $I$ is estimated to be 1.95 mA.

We will use the constant current module and do various simulations in this regime in steps of 0.25 mA. The first simulation is performed using the mechanism by Chernysheva et al. [18], in the form outlined in part two of this work, including the helium discharge processes. Then, the same simulation is done using the quite different chemical reaction scheme from the Waskoenig mechanism [107]. Here the non-equilibrium processes are the same, and the cross section data are taken from [17]. Moreover, for the second case, for all rates which explicitly depend on the electron temperature $T_e$, the value $T_e = 2.15\,eV$ has been used, i.e. $25000\,K$ which corresponds to the value obtained in the simulation described by Hemke et al. [34].

| **Parameter** | **Value** |
|---|---|
| Initial temperature | $T = 293\,\mathrm{K}$ |
| Pressure | $p = 1\,\mathrm{atm}$ |
| Discharge cross section | $A = 40\,\mathrm{mm^2}$ |
| Discharge gap | $d = 1\,\mathrm{mm}$ |
| Substance fraction | He : $O_2 = 100 : 0.6$ |
| Residence time | $\tau \approx 1.6\,\mathrm{ms}$ |
| Discharge current | $I \approx 2\,\mathrm{mA}$ |

Table 27: Experimental and calculated values of the validation experiment [25].

## 9.2 Simulation results

Figure 12 shows the results of the simulation of the reference system with the adapted Chernysheva mechanism (lines), the adapted Waskoenig mechanism (dotted) and the mechanism resulting from a modification of the Chernysheva mechanism to better describe the oxygen-helium interactions (see below). The simulation result must be compared to the experimental data presented in figure 6. This improved mechanism fits the data well.

The most significant improvement to the oxygen-helium interaction scheme presented in section 6.2 is achieved by adopting

$$\mathrm{O} + \mathrm{O_2} + \mathrm{He} \rightarrow \mathrm{O_3} + \mathrm{He}$$

with the rate of $3.4 \times 10^{-35}\,\mathrm{cm^6/s}$ at $T = 300\,\mathrm{K}$ as given by Waskoenig et al. [107].

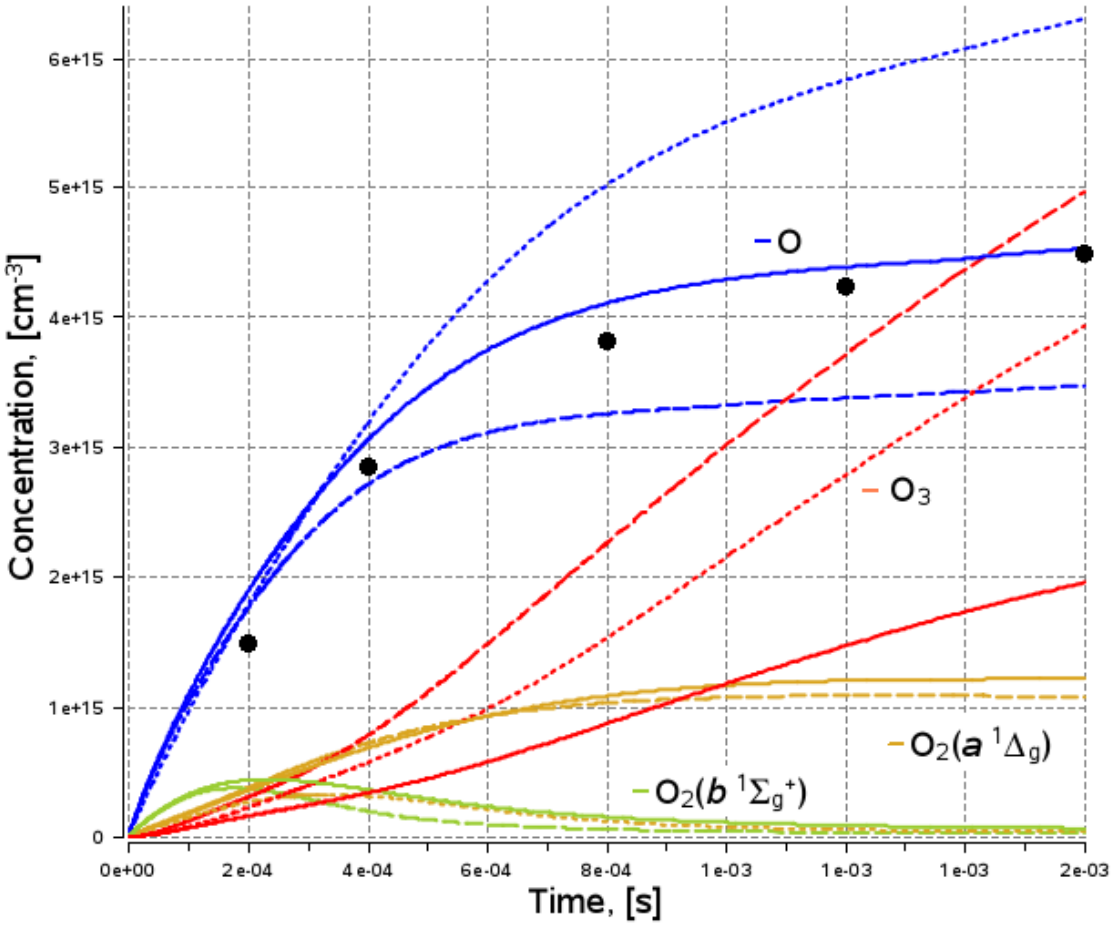


Figure 12: Development for different mechanisms for $I = 2\,\mathrm{mA}$. Low to high O concentration: variation of Chernysheva et al. [18], version of [18] augmented with oxygen-helium interaction processes, variation of Waskoenig et al. [107].

Previously, the trimolecular reaction of $O + O_2$ with helium was only incorporated via the general third partner reaction $O + O_2 + M \leftrightarrow O_3 + M$ with a rate of $6.7 \times 10^{-35}\,\mathrm{cm}^6/\mathrm{s}$ at $T = 300\,\mathrm{K}$. The computation reveals that, in turn, collisions of $O_3$ and $O_2(b^1\Sigma_g^+)$ leads to an enhanced production of $O_2(a^1\Delta_g)$ and to the formation of O. Further simulation runs, regarding a possible reduction of the mechanism, show that removing the species $O_2(r), O_2(v), O_4^+, O_4^-$, and all excited atomic oxygen species except $O(^1D)$, doesn't vary the result too much. Thus, for this simulation their effect may be neglected. On the other hand, disregarding $O_2(b^1\Sigma_g^+)$ would lead to a change of the final $O_2(a^1\Delta_g)$ concentration by a factor of two. Note that the particle $O_2(b^1\Sigma_g^+)$ is not explicitly part of the Waskoenig mechanism. A smaller but still visible effect is seen for the removal of $O_2(4.5)$. Removing the pathways through $O(^1D)$ alters the result dramatically. The end temperature $T$ depends linearly on the current $I$ and is the same for all mechanisms used. The slope of about $12\,\mathrm{K/mA}$ and a current of $2\,\mathrm{mA}$ indeed agrees well with the experimentally found temperature raise of $35\,\mathrm{K}$. The variation of predicted final species concentrations with the current in the estimated corridor from $0.001\,\mathrm{mA}$ to $0.0035\,\mathrm{mA}$ lies well within the experimental error given in [25], figure 13.

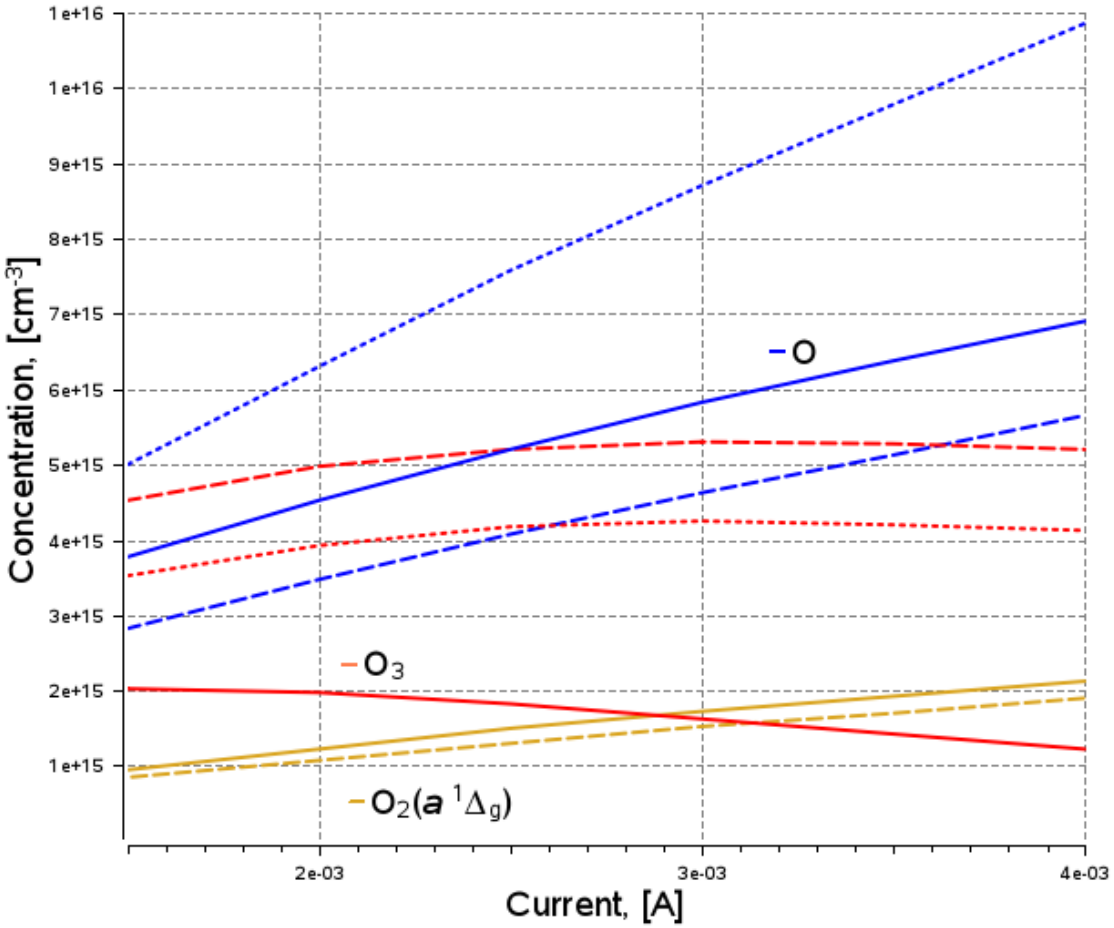


Figure 13: Comparison of the final concentrations at $t = 1.6\,\mathrm{ms}$ of the relevant species vs. current.

## 9.3 Simulation of the pure helium system

We elaborate the behavior of a helium plasma for the Magdeburg experiment parameters using the constant current model (see section 2.6) for the full estimated discharge residence time span of $5 \times 10^{-4}\,\mathrm{s}$. The experimental results provide an upper bound for current and cross section, namely roughly $I_d^{max} = 700\,\mathrm{mA}$ and $A_{I_d}^{max} = 2\,\mathrm{cm}^2$, which are combined to a naive current density estimate of

$$j = 0.35\,\mathrm{A/cm}^2 = 3.5\,\mathrm{mA/mm}^2.$$

The short mechanism used is presented in table 18. A mechanism update regarding oxygen chemistry will subsequently be performed in the context of the validation simulations in the next chapter, where the current density is known more accurately.

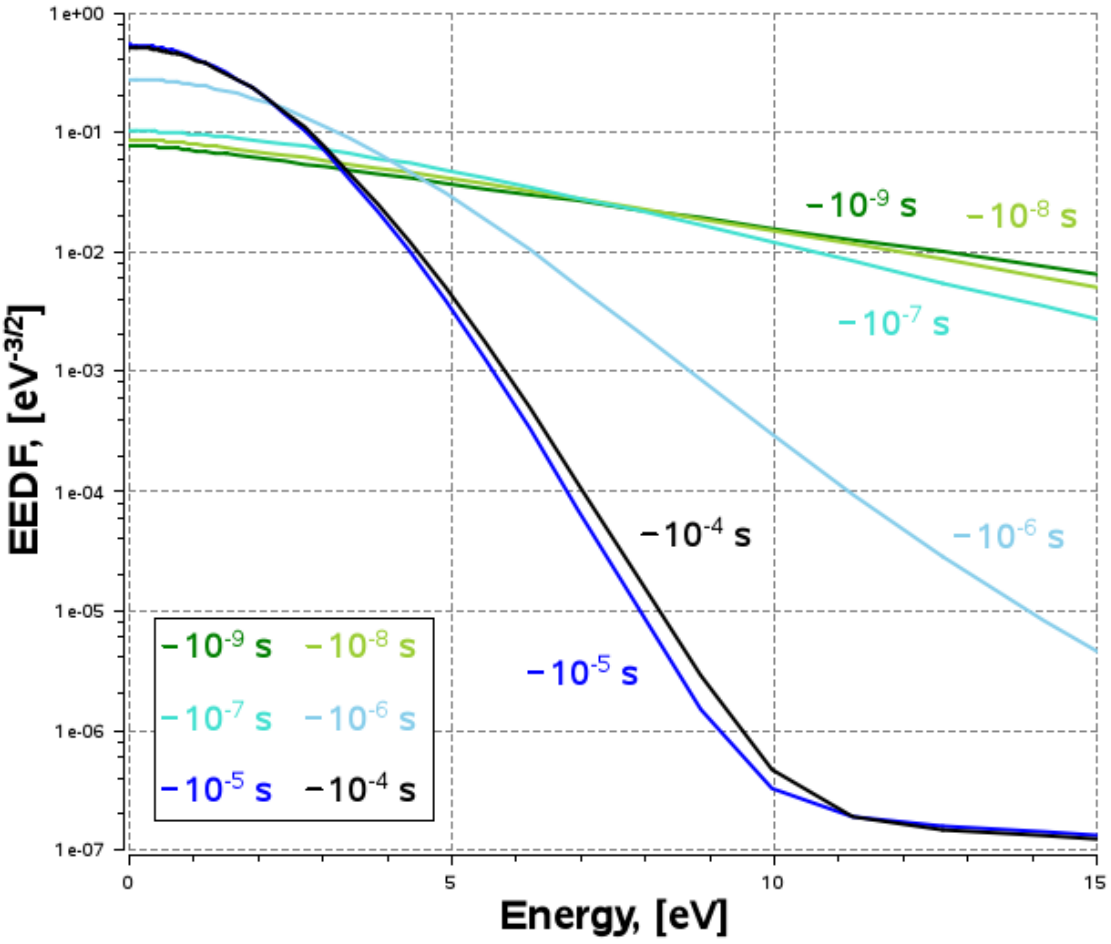


Figure 14: EEDF (log-scale) for the $j = 3.5\,\mathrm{mA/mm^2}$ simulation of the pure helium system for a broad variety of times. The almost horizontal line corresponds to the first time step at $t \leq 10^{-9}\,\mathrm{s}$.

In figure 14 we see the logarithm of the electron energy distribution function, for various times. The thick, almost flat line belongs to the initial moments of the simulation, which may be thought as the first moments after the discharge breakdown. Here, the very high initial estimated electric field $E$ leads to a significant energy transfer towards the electrons. As the current density is held constant, the electron speed $v_{\mathrm{dr}}$ falls off as the electron density rises. Effectively, this leads to a shift of the distribution function towards smaller energies.

Helium particles don't consume much, so such a discharge draws not too much energy, i.e. does not convert energy to internal degrees of freedom. For reasons of numerical convergence, around $t = 10^{-5}\,\mathrm{s}$, the field is artificially held constant at about $1\,\mathrm{kV/cm}$ or about $3\,\mathrm{Td}$, figure 15. For comparison's sake, contrast figure 15 with figure 18, where a gas mixture that consumes more electrical energy has been used. The electrical field curve always rises with the speed $v_{\mathrm{dr}} = \mu E$, where $\mu$ is the electron mobility.

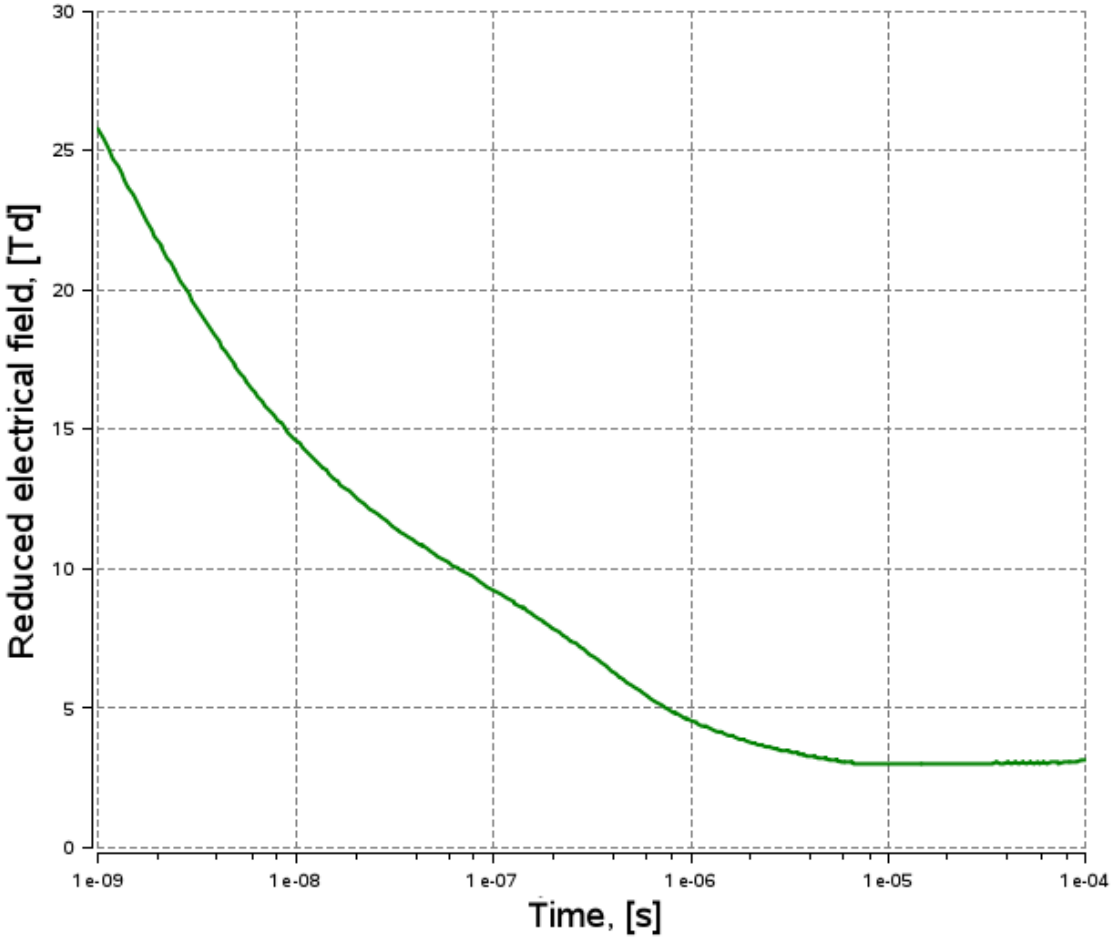


Figure 15: Electrical field for the $j = 3.5\,\mathrm{mA/mm^2}$ simulation of the pure helium system.

The microscopic dynamics can be understood from the rate data. Up to a simulation time of $t = 10^{-7}\,\mathrm{s}$, direct excitation and ionization of helium by electron impact are the most relevant processes (see gray and purple line in figure 16). Then, as soon as there are enough excited $\mathrm{He}^*$ particles in the system, ionization of $\mathrm{He}^*$ takes over instead. Over the whole simulation, elastic scattering processes

$$\mathrm{He} + \mathrm{e}^- \leftrightarrow \mathrm{He} + \mathrm{e}^-$$

have the highest rate. Indeed, it exceeds all other rates in figure 16 by a factor of four and does not vary much during the whole time interval of the simulation (green line). Those elastic scattering processes contribute to a distribution of electrical input power $P_{\mathrm{inp}} \propto E \cdot v$ towards translational degrees of freedom, i.e. steadily raise the gas temperature.

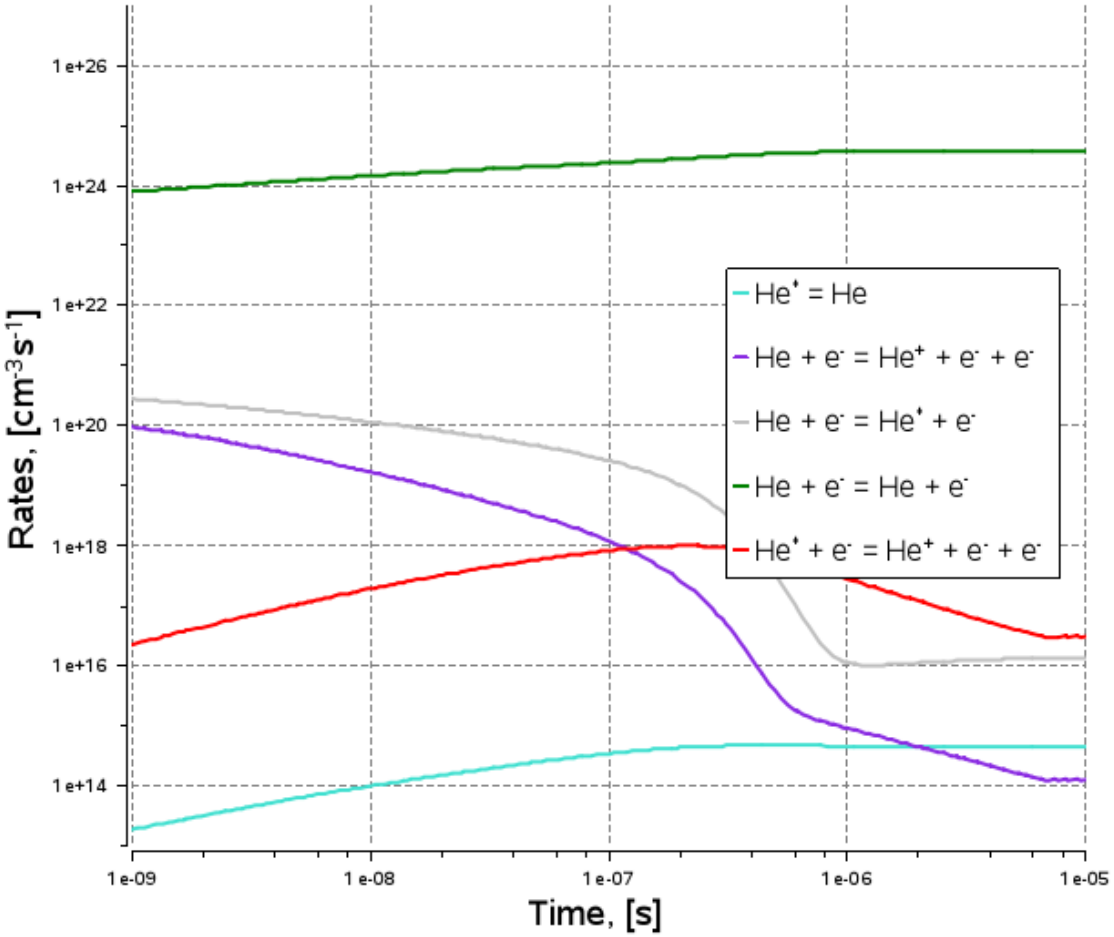


Figure 16: Selection of rates for the $j = 3.5\,\mathrm{mA/mm^2}$ simulation.

We see the corresponding rising species profiles in figure 17. The simulation starts with a tiny seed of $e^-$ and $He^+$ and the former reaches $2 \times 10^{12}\,\mathrm{cm}^{-3}$ at $t = 10^{-4}\,\mathrm{s}$. It is worth noting that the value of the initial seed of charged particles does not affect the simulation past the initial time of $10^{-8}\,\mathrm{s}$. Indeed, as the concentration of $[e^-]$ is determined by the field dependent Boltzmann equation, it eventually takes on a self-consistent value and this is also robust w.r.t. change of the mechanism. Note that $[He^+]$ must overlap with the electron concentration, due to charge conservation, but only up to the point where $He^+$ species are removed in favor of $He_2^+$. We see this transition because the mechanism only contains the process

$$He^+ + He + He \leftrightarrow He_2^+ + He,$$

but no recombination of $He_2^+$ particles.

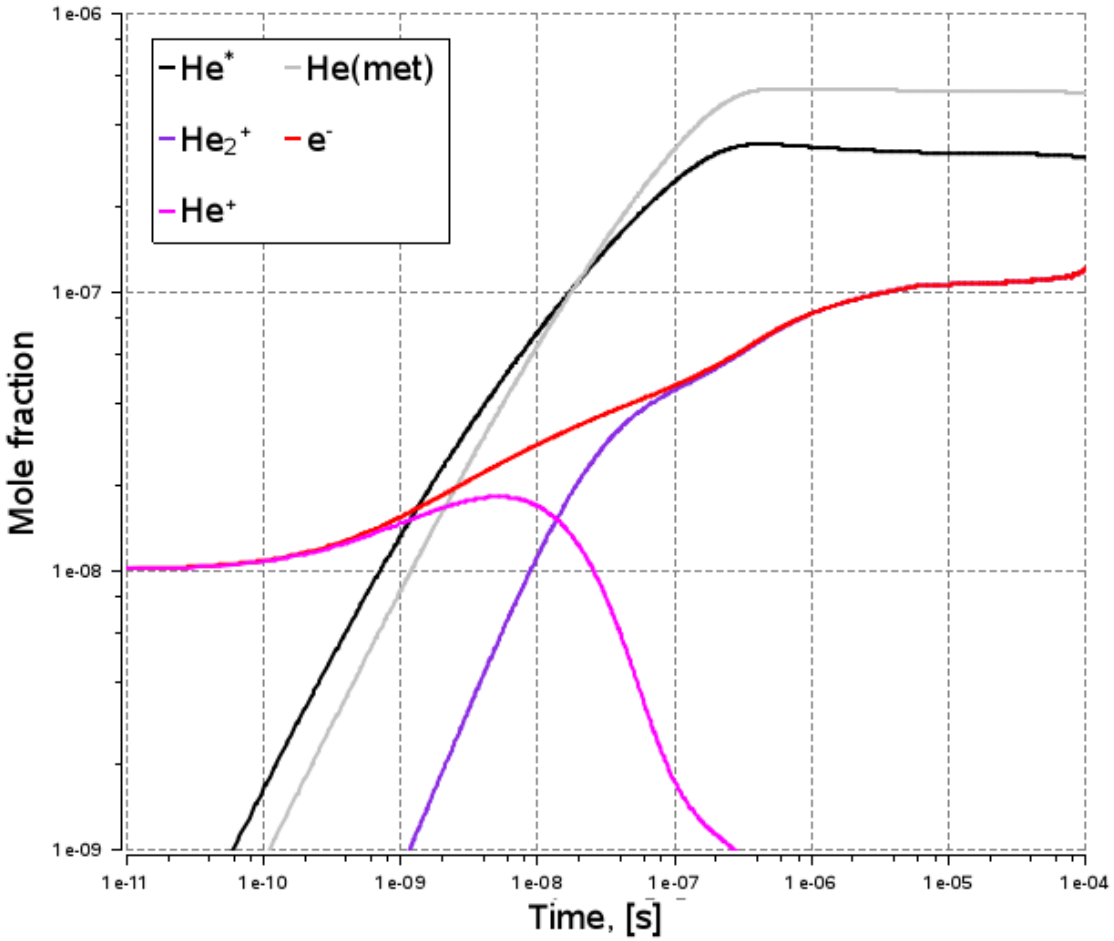


Figure 17: Selection of species concentration for the $j = 3.5\,\mathrm{mA/mm^2}$ simulation.

In the above simulation run, no significant amount of energy is stored in the helium particles $\mathrm{He}(met), \mathrm{He}^*$.

For the estimated current density, the result of the pure helium simulation shows a total temperature rise, in accordance with the experiment. The temperature development after one microsecond is linear in time.

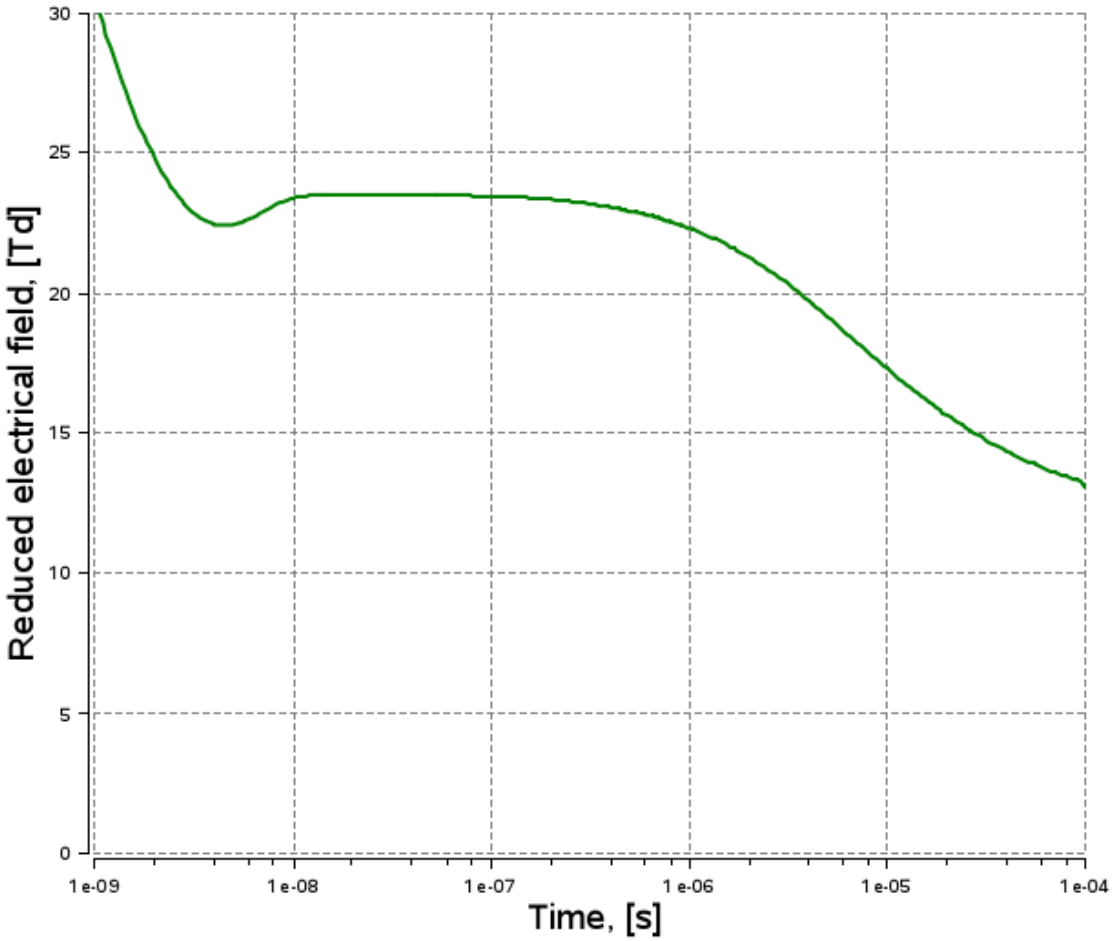


Figure 18: Electrical field for a simulation run, where 3.2% $O_2$ has been added to helium.

Below we now turn to a description of the simulation for the $O_2$/He experiment performed in Magdeburg, as described in section 5. As shown in figure 10, the next two sections concern the following zones, separately:

- Oxygen plasma in the discharge zone, followed by tubes connecting to the mixing zone.
- Mixing- and flame zone.

Here, we see that the oxygen-ion chemistry determines the dynamics. Indeed, in that case we deal with particles such as $O^+$ and $O_2^+$, but also multiple negatively charged species such as $O^-$. For this it is noteworthy to mention that the "chemical regime" in which excited molecular oxygen species accumulate really sets in only after a time of $10^{-5}$ s.

# 10 Simulation of the discharge volume

The key settings of the discharge volume can be summarized as follows: An oxygen/helium-mixture enters the discharge volume at room temperature and atmospheric pressure, where an electrical field with high oscillation frequency is applied and a plasma is thereby generated, (figure 10). The electrical energy consumed by the discharge depends on the species fractions. Experimentally, a flow rate of $q = 0.31\,\mathrm{Nm^3/h}$ and a substance fraction of $O_2 : He = 1 : 30$ has been established to give the most satisfying results with respect to optical measurements of qualitative $O_2(b^1\Sigma_g^+)$ intensities. Two other repeatedly used $He : O_2$-fractions were $15.\dot{6} : 1$ and $1 : 0$, i.e. pure helium. For higher $O_2$-fractions, the temperature rise per time becomes greater. Due to the complicated flow geometry and an unknown current cross section, the residence time can only be very roughly estimated, see table 25.

The current density and the energy input is not known, but the final temperature could be measured. At full duty cycle, the temperature at the discharge outlet (burner removed) reaches approximately 900 K.

## 10.1 Summary of approach and settings

The following is the list of parameters for the constant current model of the *Chemical Workbench* software package, which are necessary to set up the initial condition for the discharge zone simulation:

- $O_2 : He = 1 : 30$ for a cold flow with $q = 0.31\,\mathrm{m^3/h}$, i.e. $q_{O_2} = 0.01\,\mathrm{m^3/h}$.
- $e^- : He^+ = 1 : 1$ for a cold flow with $q = 10^{-10}\,\mathrm{m^3/h}$.
- Pressure $p = 1\,\mathrm{atm}$.
- Simulation end time $t_{\mathrm{end}}$.
- Current density $j$.

Here the setting for the default $O_2 : He$ ratio at room temperature is presented. Note that the only purpose of the specification of the flow rate value in this spatially zero dimensional model is to fix the ratio between charged and uncharged initial species. The reactor module also employs an ambipolar diffusion model with a discharge tube radius of 0.79 cm, see table 24. In any case, if the radius is set to half a centimeter or longer, it is observed that diffusion does not affect the simulation result. The improved reaction mechanism that is used is discussed in the preceding section 9. Apart from the basic oxidizer, the species which survive the quenching before mixing in possibly relevant amounts are:

- Electronically excited oxygen molecules $O_2(a^1\Delta_g), O_2(b^1\Sigma_g^+)$, and to a lesser extent $O_2(4.5)$.
- Electronically excited atomic oxygen $O(^1D)$.

- atomic oxygen O.
- Ozone $O_3$, which is formed in recombination processes.

As discussed, the output of the discharge zone is used as input for simple plug flow modules without electrical voltage presence, modeling the expanding tubes connecting discharge- and mixing zone. It is worth noting that the experimentally observed temperature drop between plasma outlet and mixing zone empirically corresponds to a heat loss of $2\,\mathrm{J\,cm^{-1}s^{-1}}$ in the second tube. Taking the ratio of the surfaces of the two tubes into account, this amounts to a loss of $12\,\mathrm{J\,cm^{-1}s^{-1}}$ in the first tube. In any case, the corresponding temperature drop of a few Kelvin does not noticeably affect the quenching rates of the species we are interested in.

Preliminary calculations with the naive input parameters (tables 24 and 25) show that for the fixed estimated residence time, a current density variation of $\Delta j = 0.05\,\mathrm{A/cm^2}$ leads to a significant variation of the final temperature of about $\Delta T = 40\,\mathrm{K}$. The approach taken here is therefore to perform a parameter study with respect to the unknown current density $j$, where each simulation is ended whenever the experimentally measured end temperature of approximately 900 K is reached.

## 10.2 Simulation results

We compute the species mole fractions and also predict the effective electrical energy that is provided to the burner zone.

### 10.2.1 Parameter study with respect to current density, I

Table 28 shows a selection of current density values that were used for the series of simulations, each stopped at a global gas temperature of 900 K, together with the corresponding residence time predictions.

| $j$ [A/cm$^2$] | 0.01 | 0.018 | 0.025 | 0.03 | 0.04 | 0.05 | 0.07 | 0.085 | 0.1 | 0.2 | 0.35 | 0.5 |
|---|---|---|---|---|---|---|---|---|---|---|---|---|
| $\tau$ [ms] | 24.5 | 11.0 | 8.26 | 6.92 | 5.2 | 4.2 | 3.30 | 2.5 | 2.14 | 1.08 | 0.64 | 0.44 |

Table 28: Residence times required for the $O_2$ : He = 1 : 30 mixture to reach 900 K as a function of constant discharge current

In accordance with the expectation that the residence time should go inversely to the velocity and current, which are governed by the energy input, the data permits a very accurate inverse linear fit of

$$\tau(j) = \frac{\mathrm{A/cm^2}}{j}\,0.218\,\mathrm{ms}.$$

Figure 19 shows the good accuracy of this fit for higher $j$, corresponding to the numerically more stable simulation runs.

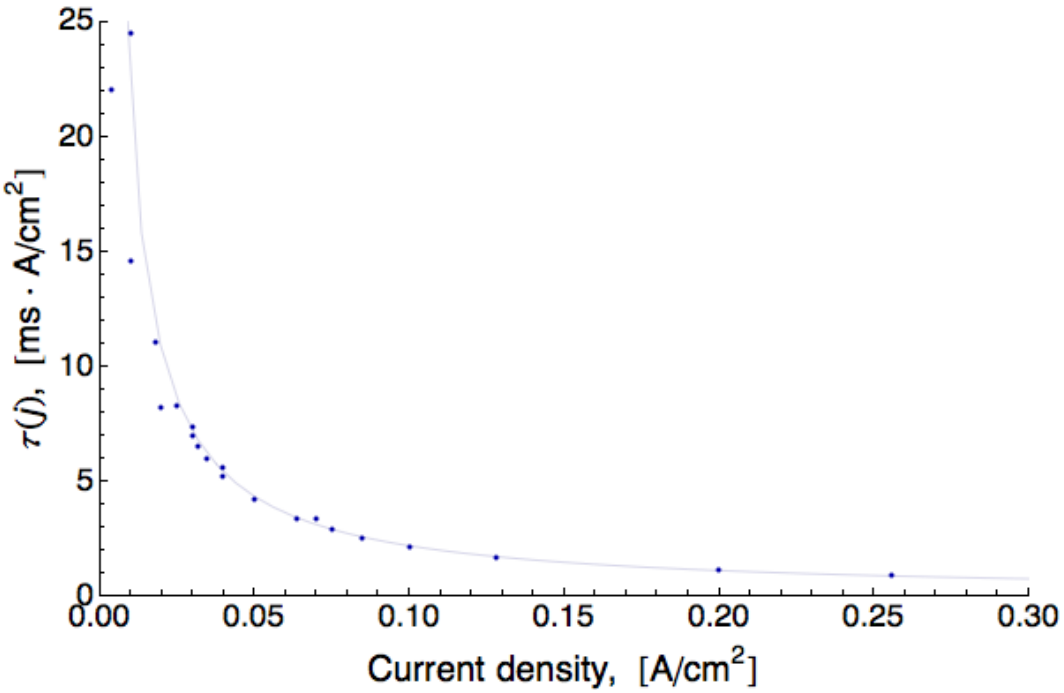


Figure 19: Predicted residence times $\tau$, using the fit $\tau(j) = \frac{\mathrm{A/cm^2}}{j}\, 0.218\,\mathrm{ms}$.
The fit of the data is more accurate for larger current densities. The least current density value which gives good convergence is $2 \times 10^{-3}\mathrm{A/cm^2}$.

Assuming a temperature rise that is linear in time, this result tells us that the 1 : 30 mixture leads to a temperature development of $(900 - 293.15)\,\mathrm{K}\,\frac{\tau(j)}{\mathrm{ms}}\frac{j}{\mathrm{A/cm^2}}$ or $2784\,\mathrm{K}$ per $\mathrm{A/cm^2}$ per ms. For a fixed residence time of hundreds of microseconds, a constant current density variation of $\Delta j = 0.1\,\mathrm{A}$ may thus already lead to a temperature change of hundreds of Kelvin.

### 10.2.2 Species evolution in the discharge zone

We discuss the typical behavior of the mixture by describing the $j = 0.5\,\mathrm{A/cm^2}$ run in detail. According to the previous subsection, this amounts to a truncation of the simulation at a residence time of about $4.4 \times 10^{-4}\,s$.

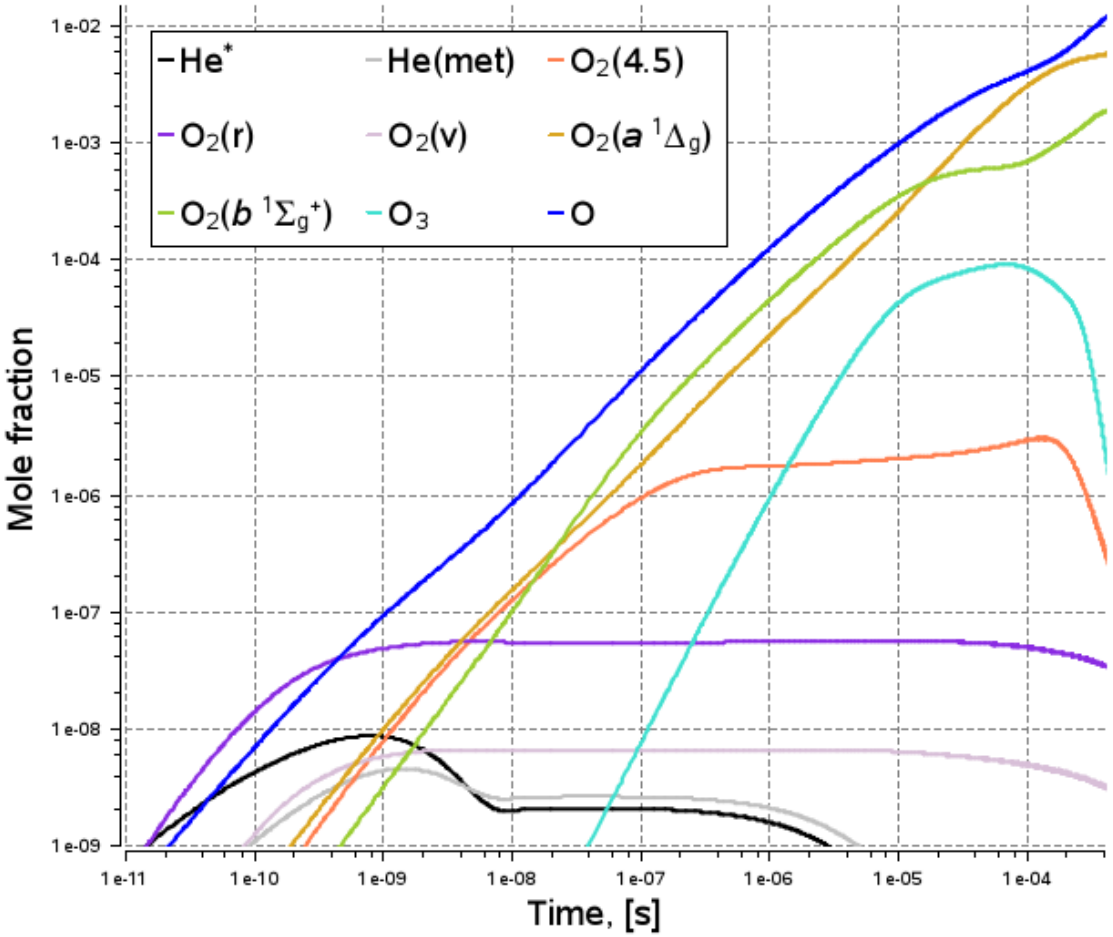


Figure 20: Excited species concentrations for the simulation with $j = 0.5\,\mathrm{A/cm^2}$.

The generation of a linear temperature rise only sets in after about $10^{-4}\,\mathrm{s}$. This is the start of the chemical regime, at which relevant macroscopic excited oxygen concentrations are generated. Irregardless of the initial numerical value, up to $10^{-6}\,\mathrm{s}$ the electrical field converges to about 23 Td and then falls off and stagnates at about 12 Td. Its evolution of the electrical field has previously been presented and compared to the pure helium mixture case, figure 18.

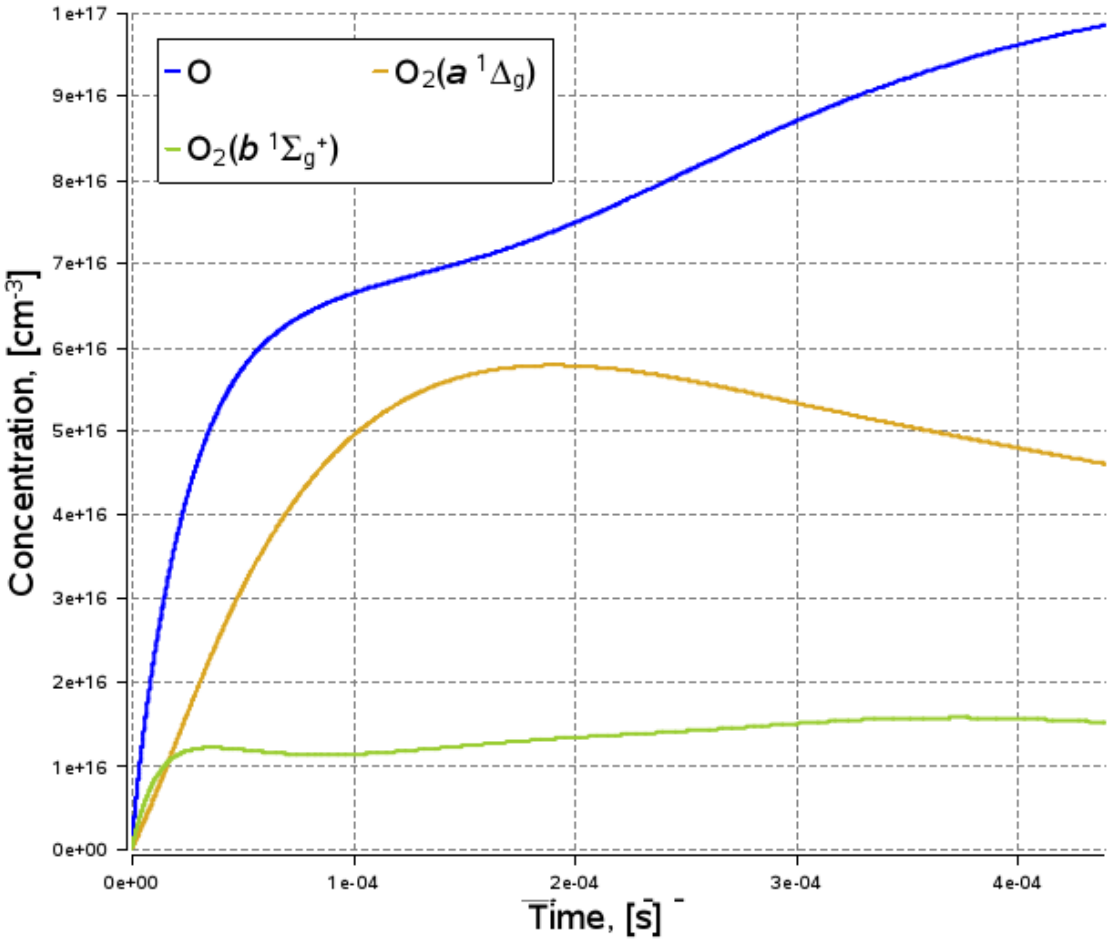


Figure 21: Relevant oxygen species concentrations (linear time axis) in the discharge zone for $j = 0.5\,\mathrm{A/cm^2}$. The species $O_2(a^1\Delta_g)$ was still growing in the last short zone 21. In contrast, now entering the large tube, the system witnesses a sudden expansion, temperature drop and decay of all excited species.

In figure 20 we see that the concentrations of excited helium species are small compared with oxygen species, even with only 3.2% oxygen in helium. These species $He^*$ and $He(met)$ enables stepwise ionization.

We are interested in the chemical regime. Figure 21 shows the evolution of $O_2(a^1\Delta_g)$, $O_2(b^1\Sigma_g^+)$, O and $O_3$ over a linear time axis. The $O_2(a^1\Delta_g, b^1\Sigma_g^+)$ concentrations lie significantly above those of $O_2(4.5)$, $O(^1D)$, which have their peak in the microsecond range and not over $10^{14}\,\mathrm{cm^{-3}}$. At the end of the discharge section, ground state molecular oxygen has dropped down to 2.4%. In contrast to the validation experiment, sections 4.1.3 and 9, ozone is not produced in significant amounts. The particle is not as stable at those higher energy input and temperatures.

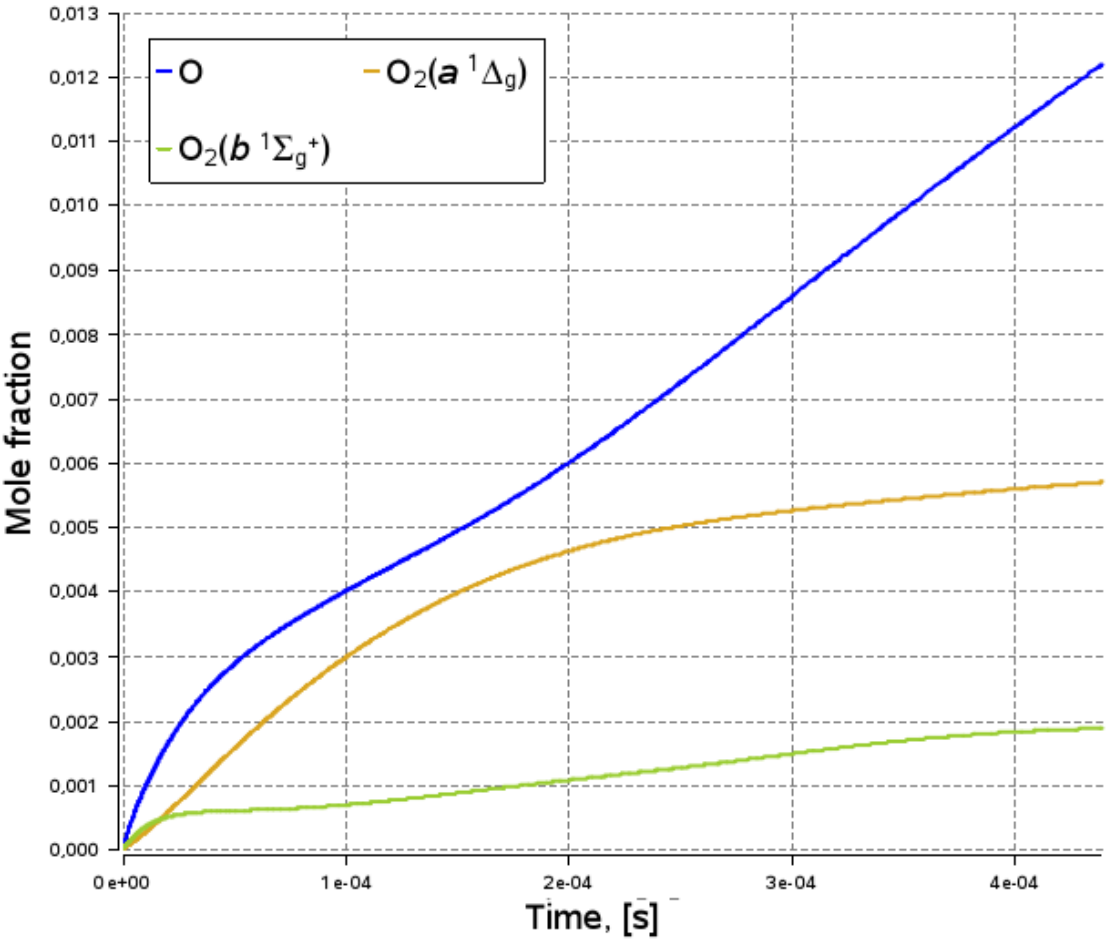


Figure 22: Oxygen species mole fractions for the simulation with $j = 0.5\,\mathrm{A/cm^2}$ The kink in the graphic is a mere artifact of few data points for simulations with small $N_2$ fractions, which require exponential computational resources.

A variation of energy input effectively impacts the growth of atomic oxygen the most. Figure 22 shows the evolution of the main species in terms of mole fractions. In this graph, in contrast to figure 21, all the species curves are monotonically increasing as the temperature rises by several hundred Kelvin. Figure 23 shows the evolution of the main species for a current density of only $j = 0.06\,\mathrm{A/cm^2}$.

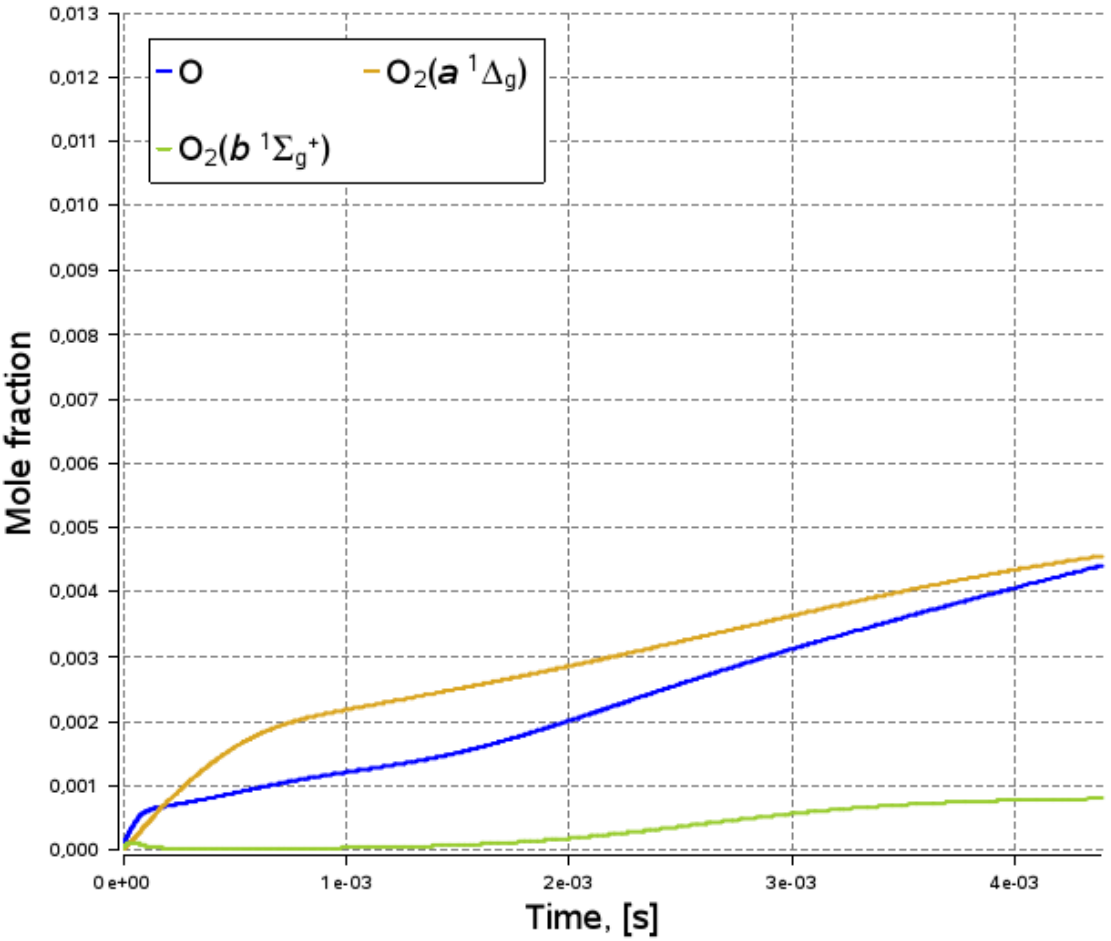


Figure 23: Oxygen species mole fractions for the simulation with $j = 0.05\,\mathrm{A/cm^2}$.

We look at the important processes and the order of magnitude of associated data, computed from the time dependent EEDF. The largest reaction rate coefficients are listed in table 29. The values are stable in the bulk of the simulation time.

| **Process** | $k$, $[\mathrm{cm^3/s}]$ |
|---|---|
| $O_2(b^1\Sigma_g^+) + e^- \rightarrow O_2(b^1\Sigma_g^+) + e^-$ | $\approx 10^{-7}$ |
| $He + e^- \rightarrow He + e^-$ | $\approx 10^{-7}$ |
| $He^* + e^- \rightarrow He^+ + e^- + e^-$ | $\approx 10^{-7}$ |
| $O + e^- \rightarrow O + e^-$ | $\approx 10^{-7}$ |

Table 29: Rate coefficients for the simulation with $j = 0.5\,\mathrm{A/cm^2}$.

Elastic processes dominate, followed by excitation of the oxygen molecule dissociation intermediate $O_2(B^3\Sigma_u^-)$. It is reached, by electron impact, not only from $O_2$, but also $O_2(a^1\Delta_g, b^1\Sigma_g^+)$ or $O_2(v)$. Corresponding rates and $\eta$-factors are presented in tables 30 and 31. Here it is revealed that production of $O_2(B^3\Sigma_u^-)$ takes a significant portion of the energy.

| **Process** | **Rate**, $[\mathrm{cm}^3/\mathrm{s}]$ |
|---|---|
| $\mathrm{He} + \mathrm{e}^- \leftrightarrow \mathrm{He} + \mathrm{e}^-$ | $\approx 10^{24}$ |
| $\mathrm{O}_2 + \mathrm{e}^- \leftrightarrow \mathrm{O}_2 + \mathrm{e}^-$ | $\approx 6 \times 10^{22}$ |
| $\mathrm{O}_2 + \mathrm{e}^- \leftrightarrow \mathrm{O}_2(r) + \mathrm{e}^-$ | $\approx 1 \times 10^{22}$ |
| $\mathrm{O} + \mathrm{e}^- \leftrightarrow \mathrm{O} + \mathrm{e}^-$ | $\approx 4 \times 10^{21}$ |
| $\mathrm{O}_2(a^1\Delta_g) + \mathrm{e}^- \leftrightarrow \mathrm{O}_2(a^1\Delta_g) + \mathrm{e}^-$ | $\approx 4 \times 10^{21}$ |
| $\mathrm{O}_2(b^1\Sigma_g^+) + \mathrm{e}^- \leftrightarrow \mathrm{O}_2(b^1\Sigma_g^+) + \mathrm{e}^-$ | $\approx 2 \times 10^{21}$ |
| $\mathrm{O}_2 + \mathrm{e}^- \leftrightarrow \mathrm{O}_2(v) + \mathrm{e}^-$ | $\approx 2 \times 10^{21}$ |
| $\mathrm{O}_2 + \mathrm{e}^- \leftrightarrow \mathrm{O}_2(B^3\Sigma_u^-) + \mathrm{e}^-$ | $\approx 1 \times 10^{21}$ |

Table 30: Electronic rates for the simulation with $j = 0.5\,\mathrm{A/cm}^2$.

Up to the chemical regime, processes such as $\mathrm{O}_2$ ionizations $\mathrm{O}_2 + \mathrm{e}^- \rightarrow \mathrm{O}_2^+ + \mathrm{e}^- + \mathrm{e}^-$ naturally play a big role. The rich chemistry of charged particles will not be described in detail here. It may be noted that the electron concentration $[\mathrm{e}^-]$ grows to and remains at $10^{12}\,\mathrm{cm}^{-3}$. At $10^{-8}\,\mathrm{s}$, $\mathrm{O}^-$ becomes the dominant negatively charged species with a peak of $10^{13}\,\mathrm{cm}^{-3}$ before $10^{-6}\,\mathrm{s}$.

| **Process** | $\eta$**-factor** |
|---|---|
| $\mathrm{O} + \mathrm{e}^- \rightarrow \mathrm{O}(^1D) + \mathrm{e}^-$ | $\approx 10\%$ |
| $\mathrm{O}_2 + \mathrm{e}^- \rightarrow \mathrm{O}_2(dis) + \mathrm{e}^-$ | $\approx 5\%$ |
| $\mathrm{O}_2 + \mathrm{e}^- \rightarrow \mathrm{O}_2(a^1\Delta_g) + \mathrm{e}^-$ | $\approx 3\%$ |
| $\mathrm{O}_2(b^1\Sigma_g^+) + \mathrm{e}^- \rightarrow \mathrm{O}_2(B^3\Sigma_u^-) + \mathrm{e}^-$ | $\approx 3\%$ |
| $\mathrm{O} + \mathrm{e}^- \rightarrow \mathrm{O}(^1D) + \mathrm{e}^-$ | $\approx 3\%$ |
| $\mathrm{O}_2(a^1\Delta_g) + \mathrm{e}^- \rightarrow \mathrm{O}_2(B^3\Sigma_u^-) + \mathrm{e}^-$ | $\approx 3\%$ |
| $\mathrm{O}_2(a^1\Delta_g) + \mathrm{e}^- \rightarrow \mathrm{O}_2(4.5) + \mathrm{e}^-$ | $\approx 3\%$ |
| $\mathrm{O}_2 + \mathrm{e}^- \rightarrow \mathrm{O}_2(b^1\Sigma_g^+) + \mathrm{e}^-$ | $\approx 2\%$ |
| $\mathrm{O}_2 + \mathrm{e}^- \rightarrow \mathrm{O}_2(v) + \mathrm{e}^-$ | $\approx 2\%$ |

Table 31: Smaller $\eta$-factor for the simuation with $j = 0.5\,\mathrm{A/cm}^2$. The $\eta$-factor for $\mathrm{O}_2 + \mathrm{e}^- \rightarrow \mathrm{O}_2(B^3\Sigma_u^-) + \mathrm{e}^-$ grows up to 60% during the whole discharge developement, followed by the factor for $\mathrm{He} + \mathrm{e}^- \rightarrow \mathrm{He} + \mathrm{e}^-$ and $\mathrm{O}_2 + \mathrm{e}^- \rightarrow \mathrm{O}_2(4.5) + \mathrm{e}^-$.

The rate of production for rotationally excited molecular oxygen is relatively large. However, the table 32 of chemical rates in the early discharge phase shows that de-excitation occurs readily. After the microsecond mark, those rates typically fall by a factor of 10. The table also shows that dissociation into $\mathrm{O}(^1D)$ indirectly enhances $\mathrm{O}_2(b^1\Sigma_g^+)$ production via the channel

$$\mathrm{O}_2 + \mathrm{O}(^1D) \leftrightarrow \mathrm{O}_2(b^1\Sigma_g^+) + \mathrm{O}.$$

| **Process** | **Rate**, $\mathrm{cm}^3/\mathrm{s}$ |
|---|---|
| $\mathrm{O}_2(r) \leftrightarrow \mathrm{O}_2$ | $\approx 10^{22}/\mathrm{s}$ |
| $\mathrm{O}_2(v) \leftrightarrow \mathrm{O}_2$ | $\approx 10^{21}/\mathrm{s}$ |
| $\mathrm{O}_2(B^3\Sigma_u^-) \leftrightarrow \mathrm{O} + \mathrm{O}(^1D)$ | $\approx 10^{21}\mathrm{cm}^3/\mathrm{s}$ |
| $\mathrm{O}_2 + \mathrm{O}(^1D) \leftrightarrow \mathrm{O}_2(b^1\Sigma_g^+) + \mathrm{O}$ | $\approx 10^{21}\mathrm{cm}^3/\mathrm{s}$ |

Table 32: Chemical rates for $j = 0.5\,\mathrm{A/cm}^2$.

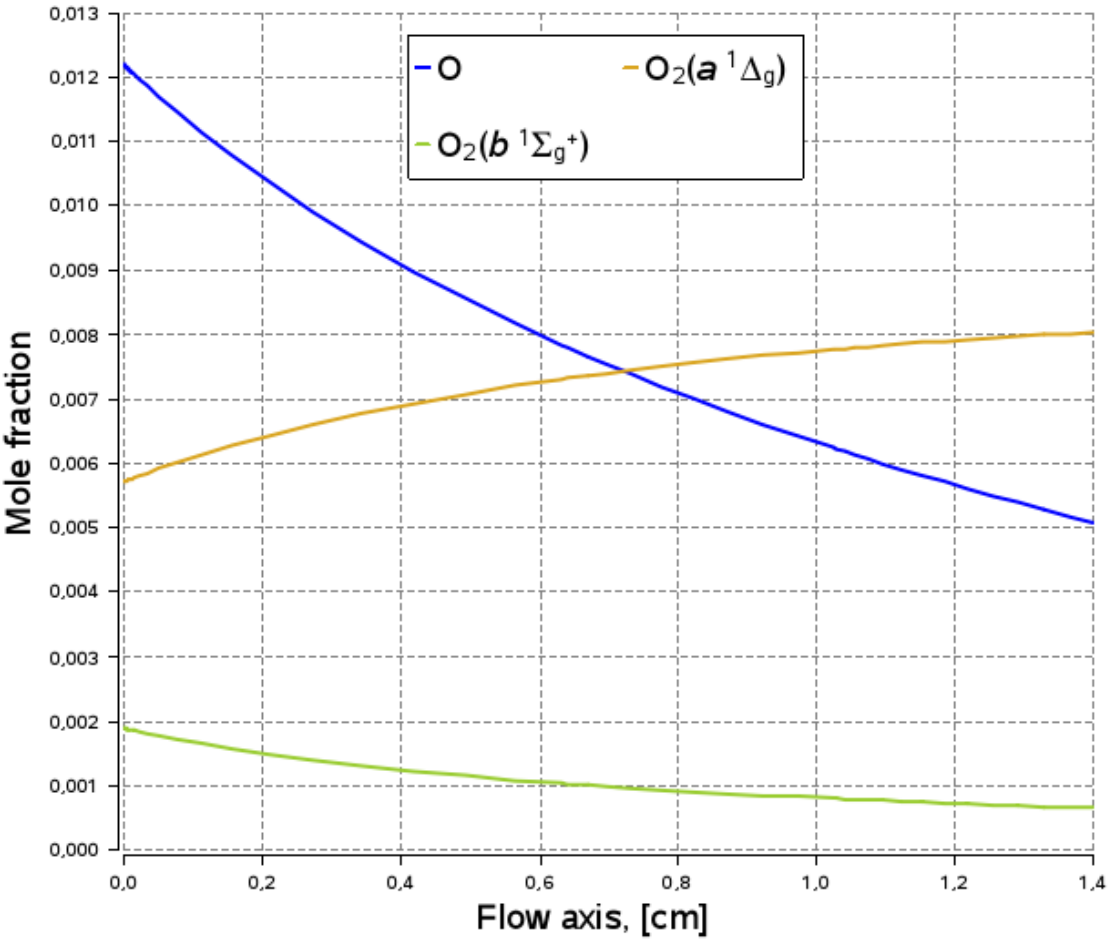


Figure 24: Oxygen species concentrations in the first tube after the discharge for $j = 0.5\,\mathrm{A/cm^2}$.

Figures 24 and 25 finally show the recombination and decay of excitation in the two consecutive tubes that follow the discharge zone. Apart from the stable $O_2(a^1\Delta_g)$ particle, all species concentrations fall below the $10^{16}\,\mathrm{cm^3}$ mark, corresponding to a mole fraction of less than $10^{-3}$.

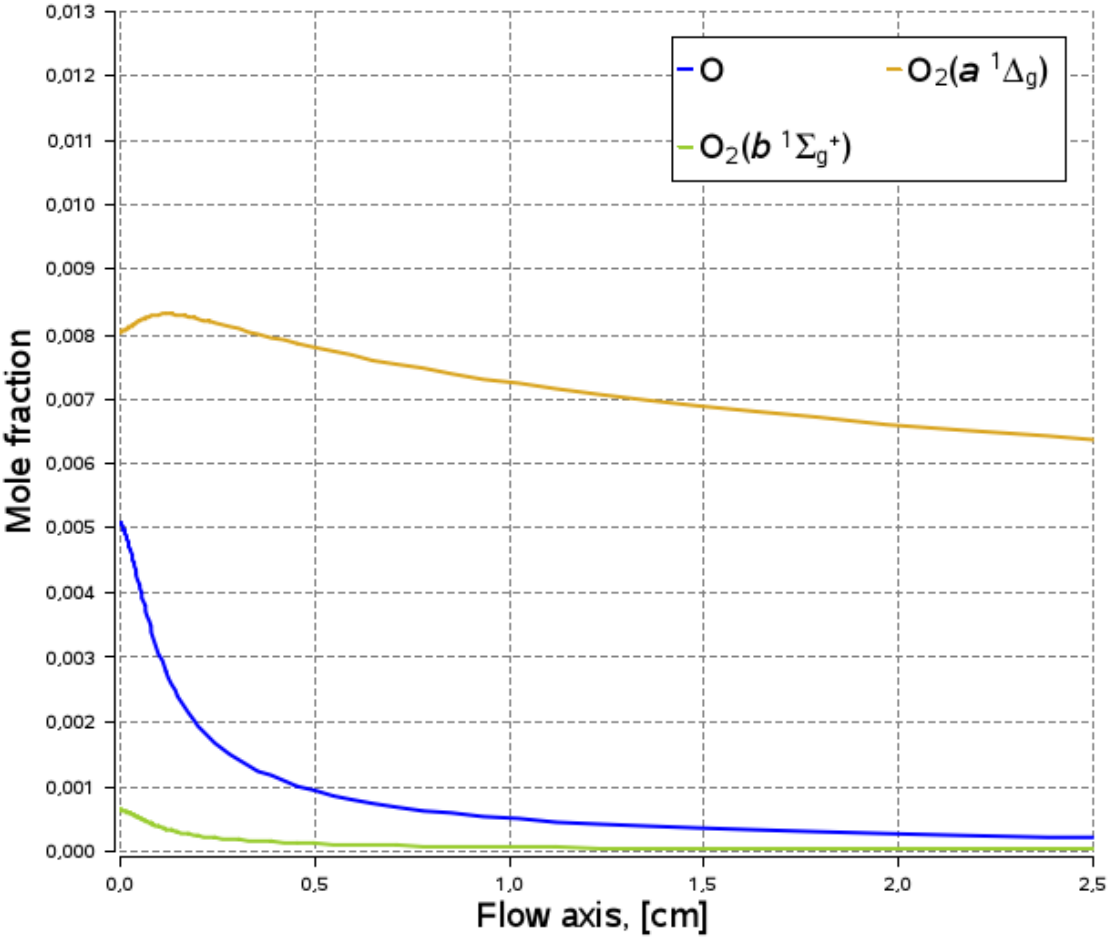


Figure 25: Oxygen species concentrations in the second tube after the discharge for $j = 0.5\,\mathrm{A/cm^2}$. The parameter change at the sudden tube expansion result in a short delay of the de-excitation of $O_2(a^1\Delta_g)$. As $O_2(b^1\Sigma_g^+)$ and O de-excitate resp. recombine, we see a peak of the $O_2(a^1\Delta_g)$ mole fraction.

### 10.2.3 Parameter study with respect to current density, II

We discuss the energy stored in the plasma state of the oxygen/helium-mixture as a function of the current density. This value can be computed by connecting the outlet of the discharge zone to an infinitely long plug flow reactor module and stop the constant current module simulations at their respective previously computed residence times. The observed total temperature rise $\Delta T(j)$, due to de-excitations and recombination reactions, can be expressed in terms of molar energy by multiplying the temperature by the heat capacity of the mixture, $C_{T=900\,\mathrm{K}} \approx 20.5\,\frac{\mathrm{J}}{\mathrm{mol}}/\mathrm{K}$. For example, $\Delta T(j = 0.5\,\mathrm{A/cm^2}) \approx 160\,\mathrm{K}$ corresponds to $\approx 3.3\,\mathrm{kJ/mol}$.

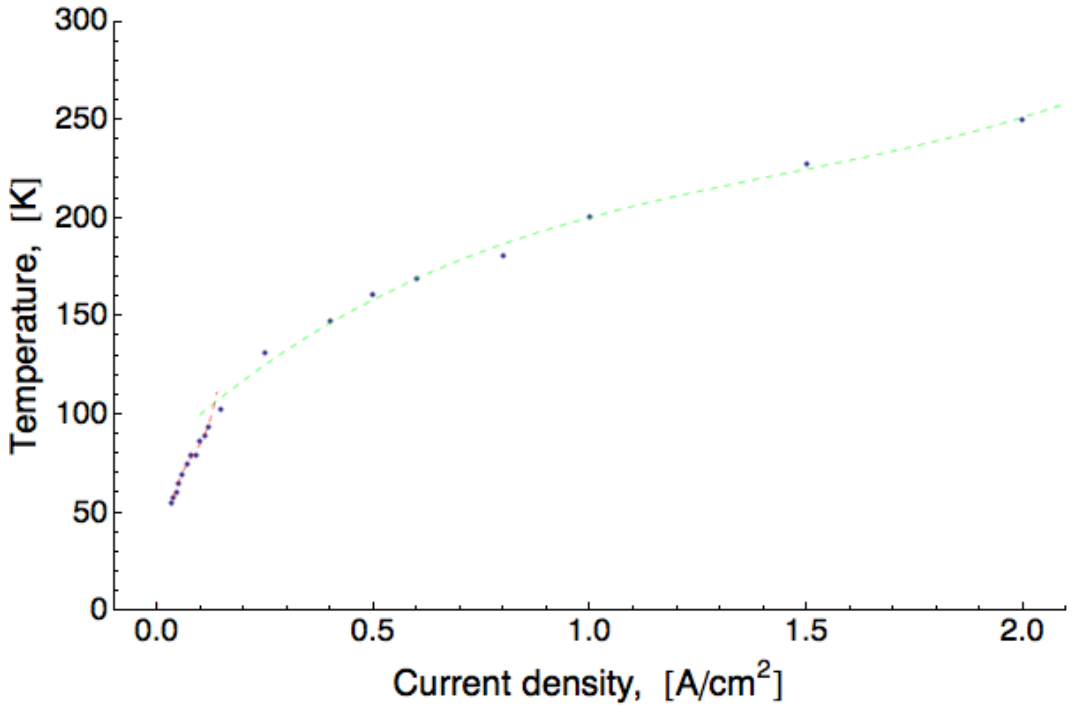


Figure 26: Energy as temperature difference over heat capacity stored in plasma vs. current density $j$, displayed using polynomial fits for two regimes

All simulations correspond to a fixed final gas temperature of 900 K, but various current densities $j$. The concavity of figure 26 tells us that the rise of stored energy with respect to $j$ slows down. We can understand this behavior by the observation that the yield of electronically excited oxygen $O_2(a^1\Delta_g, b^1\Sigma_g^+)$ quickly saturates. Simulations using initial oxygen fractions in helium larger than 1 : 30 lead to higher $O_2(a^1\Delta_g, b^1\Sigma_g^+)$ yields, suggesting the actual experimental current (for which, on the other hand, the fraction 1 : 30 was found to be the optimum), was performed at a low effective current density. We thus focus on the lower end of currents. Figure 27 shows the final species mole fractions at the end of the discharge zone (solid lines), as well as the mole fractions at the beginning for the mixing zone (dashed lines). This graph moreover shows the significant recombination of O-particles in the expanding tubes.

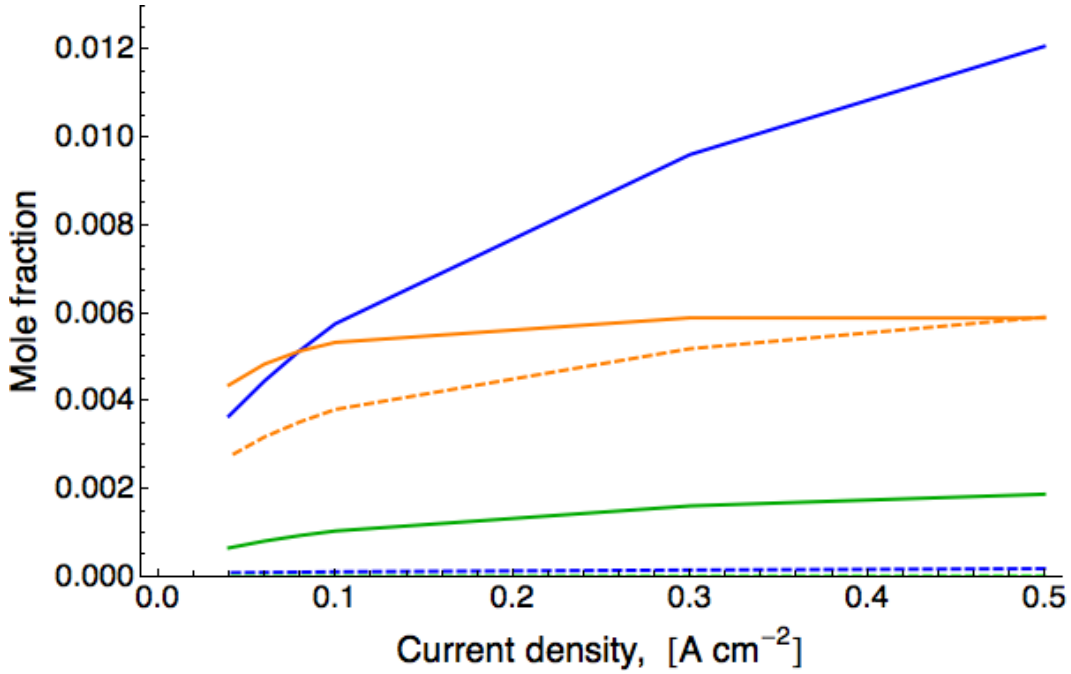


Figure 27: Final species concentrations for $O_2(a^1\Delta_g)$ (gold), $O_2(b^1\Sigma_g^+)$ (green) and O (blue) vs. constant current value at the end of the discharge zone (solid lines), and beginning for the mixing zone (dashed lines).

The mole fractions of the initial and outgoing flow, which finally enters the fuel mixing zone, for the simulation with the highest $O_2(a^1\Delta_g)$ yield is presented in table 33. For this simulation using the highest current density $j = 0.5\,\mathrm{A/cm^2}$, we find

$$\frac{[O_2(a^1\Delta_g)]}{[O_2] + [O_2(a^1\Delta_g)]} = \frac{0.026}{0.026 + 5.90 \times 10^{-3}} \approx 0.185,$$

i.e. a maximum yield of about 18.5%. According to figure 27, for the simulation using one tenth of the $j$ value, the yield is halfed and falls below 10%. Note that the effective mole fraction of excited species is further reduced when combustion with premixed fuels (which themselves also contain oxygen) is considered.

| **Species** | He | $O_2$ | $O_2(a^1\Delta_g)$ | O | $O_2(b^1\Sigma_g^+)$ | $O_3$ |
|---|---|---|---|---|---|---|
| **Input flow** | 0.968 | 0.032 | / | / | / | / |
| **Mixing zone** | 0.968 | 0.026 | $5.90 \times 10^{-3}$ | $1.70 \times 10^{-4}$ | $1.05 \times 10^{-5}$ | $1.61 \times 10^{-6}$ |

Table 33: Mole fractions entering the mixing zone for $j = 0.5\,\mathrm{A/cm^2}$.

Finally, figure 28 shows the remaining energy stored in particle excitations that the plasma provides for the burner zone.

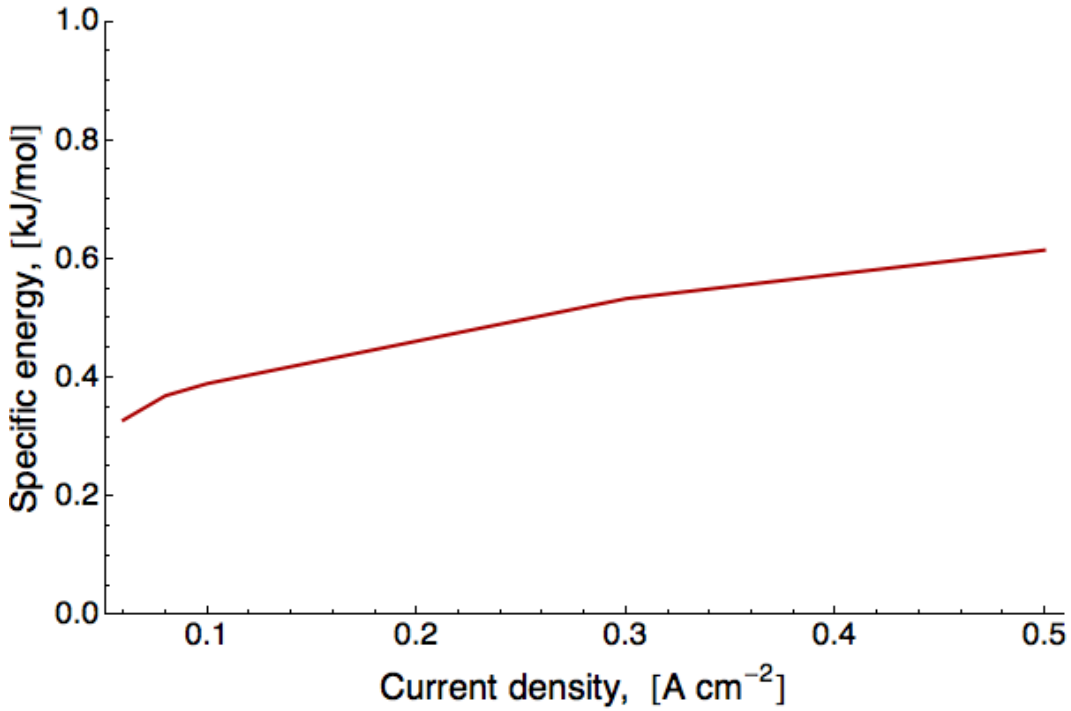


Figure 28: Energy stored in the mixtures vs. constant current value.

### 10.2.4 Yield for nitrogen containing mixtures

The devastating effect of nitrogen on $O_2(a^1\Delta_g, b^1\Sigma_g^+)$ production has been discussed in the literature overview, subsection 4.1.2. The chemistry of $O_2/N_2$ discharges is vastly more complicated than that of $O_2$/He, and, in particular, nitrogen has many excited states that can be activated by a conventional discharge itself. More particles drawing energy leads to different required powers. Thus, the behavior of a plasma depends very strongly on the initial flow mixture. It is therefore difficult to compare a $O_2/N_2$ discharge flow to that of a constant current simulation of a small fraction of oxygen in nitrogen. In figure 29 we compare the previously described species evolution, figure 21, to the simulation results of the same parameters except the initial species fraction $O_2$ : He = 1 : 30 has been replaced with $O_2$ : He : $N_2$ = 1 : 20 : 10. For this, the full nitrogen plasma reaction scheme from the *ChemicalWorkbench* reaction library has been added to the oxygen helium plasma mechanism, making for a total of 68 species and 408 processes.

We see that all excited oxygen mole fractions drop below 0.0015. At the same time, we witness the production NO close to the toxic threshold of 100 ppm [76].
Figure 30 shows the results at $t = 50\,\text{ms}$ of a computation with $j = 0.2\,\text{A/cm}^2$ for the described $O_2$/He mixture with a gradually larger additional $N_2$ mole fraction. No stable simulation results could not obtained for small $N_2$ fractions. As expected, the final excitation levels of $O_2(a^1\Delta_g)$ and $O_2(b^1\Sigma_g^+)$ particles drop quickly for higher initial $[N_2]$.

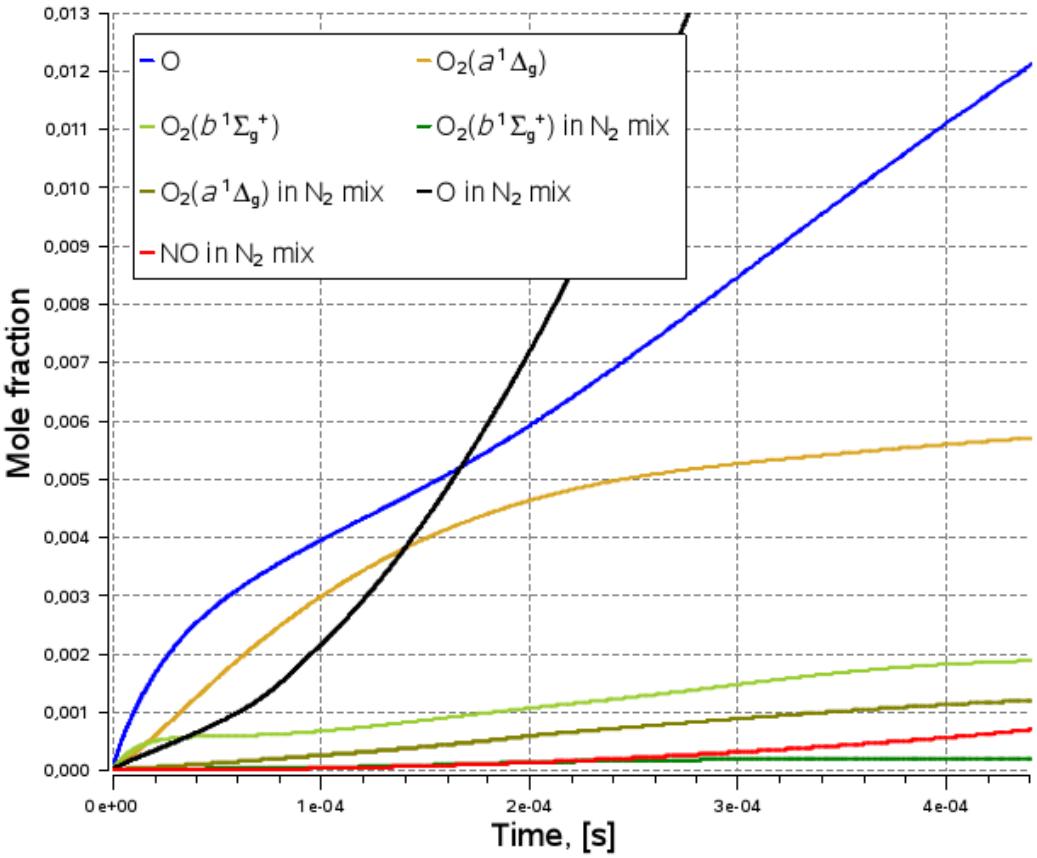


Figure 29: Mole fractions for two constant current simulations with discharge parameters as in figure 22: An initial $N_2$ fraction of about 1/3 reduces the excited oxygen yield most significantly.

With 945 kJ/mol, the bond energy of $N_2$ is almost twice as large as that of $O_2$. Therefore, as the current density is fixed, higher initial nitrogen mole fractions also lead to more $O_2$ and $N_2$ dissociations, as well as a steeper temperature rise. The final temperature for the nitrogen containing mixture in figure 29 rises well above typical flame temperatures.

## 10.3 Discussion of the discharge zone

The performed calculations predict species profiles in the plasma generator, the quenching of the plasma-treated oxidizer and also provide a comparison of the effect of the temperature increase by the generator, with the effect of the generation of excited and chemically active species, on the flame speed and ignition delay. The atomic oxygen chemistry was validated using a literature experiment that shares relevant conditions with the main experiment of interest, that has been performed in Magdeburg: The gas composition and electric field strength are very similar. However, in this case, in contrast to the Magdeburg experiment, a simple rectangular geometry allows a reliable estimate of the particle residence time. Figure 12 shows the simulation result for the atomic oxygen production.

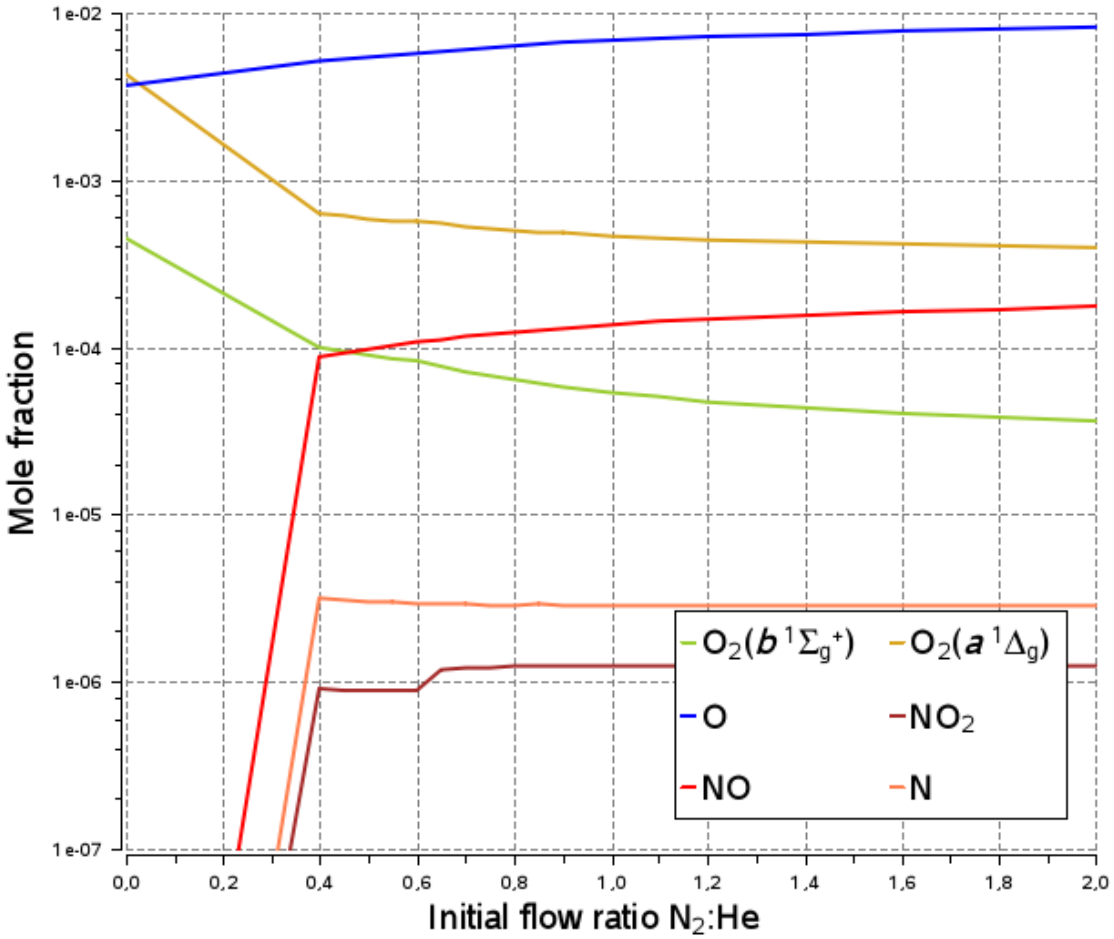


Figure 30: Mole fractions at $t = 5 \times 10^{-4}$s for $q_{O_2} = 0.01\,\mathrm{m}^3/\mathrm{h}$ and $q_{He+N_2} = 0.3\,\mathrm{m}^3/\mathrm{h}$ and $j = 0.2\,\mathrm{A/cm}^2$ for various ratios $He : N_2 = 1 : x$. For low $N_2$ fractions, stable results could not be obtained computationally.

The original mechanism describing the main $O_2^*$ species in a plasma (dashed lines) was adapted to account for helium plasma chemistry (solid lines) and compared with a literature mechanism (dotted, Waskoenig et al.), which negletcs electronically excited oxygen states. The second mechanism shows the best fit to the measured data (Kracke et al., 2010). The author's energy-efficiency estimate (the fraction of energy that is transmitted into the chemical degrees of freedom, in spite of all electrical and thermal losses in the gas) is given as $1/20 = 0.05$. Finally, the temperature development agrees with the experiment as well.

The setup of the experiment in Magdeburg is described in section 8. The almost constant current in the low temperature plasma is governed by the free electrons, responsible for the energy transfer to other chemical species. Rates were always computed by solving the Boltzmann equation for the electron energy distribution function. For the discharge breakdown and initiation of the electron cascade in Magdeburg experimental setup, the simulation predicts a required minimum field strength value of 24 Townsend. However, the main interest for this work is the chemical regime, starting after about $10^{-5}$ seconds.

The fraction of electrical energy effectively implemented in the plasma zone has a significant impact on typical reaction rates, in particular the oxygen dissociation. However, this numerical value, which depends on the whole apparatus, is very hard to estimate directly from experiment. To understand the plasma system despite the lack of definite effective power input data, parameter studies with respect to various current densities have been performed (section 10). Experimental temperature data were taken as boundary condition to the plasma dynamics in the computation. The species mole fractions for two reference points (just after the discharge zone and right in front of the flame zone) is shown in figure 27. As the temperature in the plasma zone rises by several hundred degrees, dissociation rates go up significantly. Thus, in comparison to the validation experiment, the ozone concentrations are insignificant for the system considered. Figure 20. shows an example of the species profiles for excited helium and oxygen particles for the standard parameters in the experiment. The species O, $O_2(a^1\Delta_g)$ and $O_2(b^1\Sigma_g^+)$ are those which may be relevant for the change in the combustion path, as shown in figure 29. This graph also demonstrates the development of a variation system at a constant current density, in which the flow with helium is replaced with a flow containing one third of nitrogen. In this case, as must be expected due to quenching, the production of excited oxygen is severely restricted (green and brown lines). Simultaneously, nitrogen oxides near the toxic threshold of 100 ppm were produced (red lines).

The two sections after the plasma zone were each modeled as a plug flow, see figures 24 and 25. The enlargement of the cross-section in the second tube and the artificial cooling of the experimental set-up were taken into account. For the simulated second tube with dimensions of 2.5 cm in length and 1.3 cm in diameter, the latter corresponds to a decrease in energy of $12\,\mathrm{J\,s^{-1}cm^{-1}}$. The density drop associated with the temperature rise is clearly visible in the graph. In any case, the time evolution of the mole fractions shows that the three plasma products most relevant for combustion, O, $O_2(a^1\Delta_g)$ and $O_2(b^1\Sigma_g^+)$, continuously increase. Simulations with higher initial $O_2$ percentage (or equivalently, a lower fraction of helium gas), lead to a stronger temperature, as must be expected. In this case, due to the chemical properties of $O_2$, a higher voltage is required for discharge breakdown. Here, the atomic oxygen mole fraction obtained for the simulation with a high current density of $j = 0.5\,\mathrm{A/cm^2}$ reaches a value of 0.012 at the end of the discharge zone (initial value of $O_2$ is 0.032), but recombines back to molecular oxygen in the subsequent zones. The species $O_2(a^1\Delta_g)$ on the other hand is stable, as compared to O and $O_2(b^1\Sigma_g^+)$. Therefore, even for the more realistic current density of $j = 0.06\,\mathrm{A/cm^2}$, a $O_2 : O_2(a^1\Delta_g)$ ratio of 11% is found at the beginning of the flame zone. Higher electrical powers lead to a higher degree of $O_2$ dissociation and a higher temperature rise. In conclusion, the result of the calculation of plasma-chemical processes predict that an experimental setup with smaller electrical power input leads to comparably high $O_2(a^1\Delta_g)$ production rates.

# 11 Simulation of the burner zone

## 11.1 Simulation approach

We are going to discuss the influence of excited particles on combustion for settings akin to the experimental conditions described in chapter 5 and contrast it with thermal effects. The configuration is depicted in figures 10 and 7. Two streams meet in a co-flow configuration at the burner outlet where the mixture is ignited:

- The premixed fuel at room temperature ($O_2$/He and either $H_2$ or $CH_4$),
- The $O_2$/He flow interacting with the plasma.

The chemistry of reactive flow mixing is investigated in a two step model: First, the temperature $T_{\text{mix}}$ of the combined flows is computed in an instantaneous mixing process using the mixing reactor in the *Chemical Workbench* software package. The effect of realistic temperature variations of the discharge zone on the flame velocity on an oxidizer stream without excited oxygen is estimated. Then, quenching and combustion of various concentrations of excited particles in the oxidizer affected by the plasma are studied using a premixed flame model.

## 11.2 Simulation results

### 11.2.1 Methane combustion

The discharge outlet results for a current of $j = 0.5\,\text{A/cm}^2$ were presented, in terms of mole fractions, in table 33. They correspond to the highest computed yield $\frac{[O_2(a^1\Delta_g)]}{[O_2]+[O_2(a^1\Delta_g)]}$ of $\frac{0.002}{0.01} = \frac{1}{5}$ or 20%.
The typical premixed methane fuel flow considered in the experiments, as well as the oxidizer stream from the discharge outlet, are presented in table 34. As the fuel flow rate is notably higher than the rate from the discharge flow, the effective excited oxygen mole fraction of the combined streams is reduced further. In fact, taking into account the 55 times larger oxygen stream from the premixed flow, after instantaneous mixing, the effective yield drops down to $\frac{0.002}{0.55+0.01} = \frac{1}{280}$, i.e. below 0.4%.

| **Flow rate** | **Premixed stream** | **Discharge outlet** |
|---|---|---|
| Total | $1.31\,\text{Nm}^3/\text{h}$ | $0.31\,\text{Nm}^3/\text{h}$ |
| $CH_4$ | 0.26 | / |
| He | 0.50 | 0.30 |
| $O_2(a^1\Delta_g)$ | / | $\leq 0.002$ |
| $O_2$ | 0.55 | $\leq 0.01$ |
| Temperature | 300 K | $\approx 740\,\text{K}$ |

Table 34: Methane premixed fuel- and discharge zone simulation output flow.

The significantly higher cold mass flow also largely determines the temperature $T_{\text{mix}}$ after mixing. Table 35 reveals that any temperature increment of the flow from the discharge zone by hundred Kelvin leads to a rise of only about fifteen Kelvin after mixing. Thus, for a temperature rise in the discharge of $\Delta T = 440\,\text{K}$, instantaneous mixing with the premixed methane fuel results in a mixture temperature of only $T_{\text{mix}} = 367.2\,\text{K}$.

To study auto-ignition behavior, bomb reactor simulations for the various fuel flows considered in this section have been carried out. The experiments described in section 5 never witness auto-ignition and this is indeed also the result for bomb reactor simulations.

| $T_{\text{discharge}}$ [K] | 300 | 400 | 500 | 600 | 700 | 800 | 900 | 1000 |
|---|---|---|---|---|---|---|---|---|
| $T_{\text{mix}}$ [K] | 300.0 | 315.5 | 330.7 | 346.0 | 361.1 | 376.3 | 391.3 | 406.3 |

Table 35: Mixing reactor temperatures vs. discharge outlet flow temperatures.

The results of the following flame simulations have been carried out using the well known Konnov mechanism for methane combustion [48], together with the $O_2(a^1\Delta_g)$ chain propagation, chain termination and quenching reactions proposed by Lebedev et al. [54], which were previously discussed in subsection 7.4.2.

Firstly, we perform flame simulations for flows as listed in table 34, while assuming zero oxygen excitation. Here we can easily estimate the effect of temperature variation on characteristic flame properties, by manually varying temperature of the discharge outlet. We find a flame velocity of $v_{\text{front}} = 217.5\,\text{cm/s}$ for a cold 300 K oxygen-helium stream.
It is worth noting that these velocities may appear high compared to stoichiometric methane-air mixtures. The reason is that we consider helium, while air contains a $N_2 : O_2 \approx 4 : 1$ fraction of the heavier nitrogen particles. Turning up the discharge temperature, the flame velocity linearly grows by 13.9 cm/s for each increment of hundred Kelvin. Thus, for $\Delta T = 440\,\text{K}$, as measured in the experiments, we get a growth of $\Delta v_{\text{front}} = 61.2\,\text{cm/s}$ and hence a flame velocity of $v_{\text{front}} = 278.7\,\text{cm/s}$. For a second parameter study, we fix the discharge outlet temperature to 740 K and vary the $O_2(a^1\Delta_g)$-fraction of the $q = 0.01\,\text{Nm}^3/\text{h}$ oxygen flow between 0 to 20%. The new reactions with the highest rates during the combustion process are the chain propagation reactions

$$CH_3 + O_2(a^1\Delta_g) \rightarrow CH_3O + O$$

and

$$CH_3 + O_2(a^1\Delta_g) \rightarrow CH_2O + OH.$$

Like a rise of initial temperature, the effect of a higher $O_2(a^1\Delta_g)$-fraction on the flame velocity is linear. In any case, even for 20% excited oxygen, we only find an additional flame velocity growth of about 1 cm/s, i.e. an improvement of $v_{\text{front}}$ by only 0.3%. This corresponds to a discharge temperature variation of less than 7.2 K. The overall small impact of the excited oxidizer stream is explained by the very small effective yield obtained after instantaneous mixing with the fuel.

### 11.2.2 Hydrogen combustion

The typical premixed hydrogen fuel flow considered in the experiments, as well as the oxidizer stream from the discharge outlet, are presented in table 36. The oxygen flow rate from the channel with the premixed fuel is $0.115\,\mathrm{Nm^3/h}$ and therefore significantly smaller than in the above consideration for methane. The highest excited oxygen mole fraction is the same as in the discussion of methane. After instantaneous mixing, the remaining effective yield is $\frac{0.002}{0.115+0.01} = \frac{1}{62.5}$ or 1.6%.

| **Flow rate** | **Premixed stream** | **Discharge outlet** |
|---|---|---|
| Total | $1.085\,\mathrm{Nm^3/h}$ | $0.31\,\mathrm{Nm^3/h}$ |
| $H_2$ | 0.250 | / |
| He | 0.720 | 0.30 |
| $O_2(a^1\Delta_g)$ | / | $\leq 0.002$ |
| $O_2$ | 0.115 | $\leq 0.01$ |
| Temperature | 300 K | $\approx 740\,\mathrm{K}$ |

Table 36: Hydrogen premixed fuel- and discharge zone simulation output flow.

The results of the following flame simulations have been carried out using the recent hydrogen-excited oxygen combustion mechanism by Starik [95], previously discussed in subsection 7.3.2.

For the flow rate listed in the above table 36, and $\Delta T = 440\,\mathrm{K}$ from the discharge, we end up with $T_{\mathrm{mix}} = 389.6\,\mathrm{K}$. Without excited oxygen, this leads to a hydrogen flame velocity of $v_{\mathrm{front}} = 273.0\,\mathrm{cm/s}$, figure 31. Each temperature rise of hundred Kelvin from the discharge leads to a rise of 20.3 K of the mixing temperature $T_{\mathrm{mix}}$ and a flame velocity growth of 23.5 cm/s. The effect of excited oxygen on the flame velocity is again linear. For the maximum yield of 20% (resp. 1.6% after instantaneous mixing), we find a flame velocity growth of $\Delta v_{\mathrm{front}} = 7.6\,\mathrm{cm/s}$, i.e. an improvement of $v_{\mathrm{front}}$ by 2.8%. This corresponds to a discharge temperature variation of less than 32.3 K. The reason for the small effect can again be found to be the small excited oxygen fraction obtained after instantaneous mixing with the fuel, where the maximum $O_2(a^1\Delta_g)$-yield effectively dropped down from 20% to 1.6%.

Using the flame simulation module, we can consider a case with significantly reduced thermal power. If we mix the discharge outlet flow with a pure $H_2$ flow of $0.155\,\mathrm{Nm^3/h}$, (instead of the premixed $1.085\,\mathrm{Nm^3/h}$ flow of $O_2/H_2/He$, thus removing the unexcited oxygen from the fuel channel, but keeping the final mixture stoichiometric), the increase of the flame velocity by excited oxygen exceeds 100%.

For validation purposes, the simulations without $O_2(a^1\Delta_g)$ molecules have also been performed, in particular using the hydrogen combustion mechanism by Li [56]. The change of flame velocity with variation of discharge temperature agree, however, it should be noted that all mechanisms are found to disagree on the exact value of parameters such as the flame velocity by tens of centimeter per second. Thus, the effect of chosing another mechanism is actually greater than the addition of excited oxygen particles that have been considered.

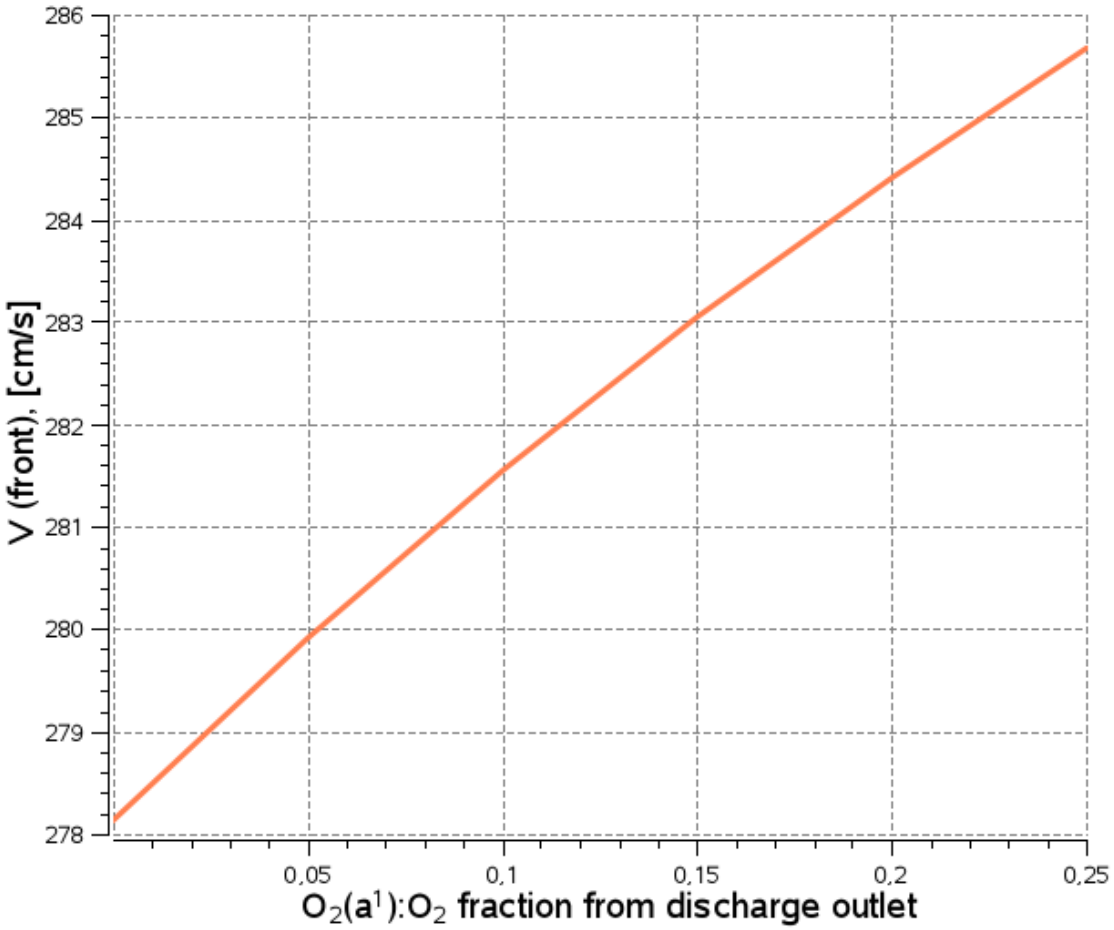


Figure 31: Flame velocity for the hydrogen flame for various excitation levels.

## 11.3 Discussion of the burner zone

The plasma and the fuel meet in the experiment in a co-flow configuration. A possible mixture with nitrogen from the surrounding air was not considered numerically. Concretely, the mixture, quenching and the influence on ignition delay and flame speeds for premixed flames were examined. As the lean to stoichiometric ($\Phi \leq 1$) premixed $O_2$ / fuel mixture is combined with a significantly higher volume flow (e.g. $CH_4 : O_2 : He = 0.5 : 1 : 1$ at a flow rate of $1.31\,m^3/h$) for the flame simulation, the $O_2(a^1\Delta_g)/O_2$ ratio is further reduced below 1%. After the temperature drops in the expanding volume, an experimentally determined temperature increase of up to 300 K remains and the plasma current thus reaches the premixed fuel with 600 K. This implies a temperature rise of the mixture of 15 K per 100 K from the plasma zone. For example, for the before-mentioned methane mixture and ignoring any of the excited oxygen chemistry, this temperature rise leads to an increase in the flame velocity from 218 cm/s to 279 cm/s (these values are generally high due to the helium percentage, as compared to nitrogen in air), see figure 31. With or without temperature rise, the addition of the products of the plasma source, especially O and $O_2(a^1\Delta_g)$, has an accelerating effect on the initiation reactions and consecutive to the flame speed.

However, it was shown that a percentage of plasma products in the single-digit range is ultimately negligible when compared to the effect of the temperature rise. This trend does not change when the mixture is further removed from the stoichiometric range.

The one-dimensional simulations for quenching without fuel or nitrogen match the experimental result so that excited oxygen particles are detectable centimeters above the outlet, even at atmospheric pressures. The fine influences on the cold mixture ("precombustion") observed in the experiment could not be reproduced in the simulation. This may be due to the simplicity of the mechanisms describing the ignition and oxidation at low temperatures. Finally, it must be emphasized that the difference for calculations using various established mechanisms is sometimes bigger than the difference, which is brought by an increase in temperature of 100 K from the plasma source itself. Thus, such mechanisms and their extension are useful to predict the concentration change of the oxidizer with and without a discharge, but are, at the moment, less reliable regarding the exact concentrations.

# 12 Summary

In this work, reaction mechanisms and computationally efficient simulation modules for plasma assisted combustion have been reviewed and developed. Design and validation for three reactor types have been performed: Spatially 0-dimensional plasma discharges, 1-dimensional plug flows and finally 1-dimensional mixing and flame zones. While literature on experimental concentration profiles for non-thermal oxidizing plasmas and its resulting reactive flows at atmostpheric conditions is scarce, the simulation's results for species profiles for the RF-discharge and its combustion provide realistic predictions or have been validated. The developed reaction mechanisms allow for time-efficient calculations of the model reactor in the plasma zone as well as in the flame zone (a maximum of a few hours on a standard PC). The improved oxygen plasma scheme (162 reactions) entails 24 additional reactions accounting for helium as diluent. Experiments documented in the literature with simple geometry have been used for the validation of the atomic oxygen chemical kinetics of the developed mechanism. The coupled simulation models consume little computational resources and can aid technical realizations of combustion systems for methane and hydrogen combustion.

The transfer of electrical to chemical energy in the simulation of the discharge zone is relatively low, meaning the plasma development is accompanied by a large temperature rise. A higher temperature also supports dissociation and thus the production of atomic oxygen particles, whereas the main target in the setup is the excitation of molecular oxygen. These species are much more stable in the plug flow that connects the discharge and the flame zone. Finally, the efficiency to produce excited molecular oxygen is observed to fall with growing current density, as those are correlated with higher temperatures.

The described results for the flame zone suggest that the effective use of an oxidizing plasma source in this configuration (radio-frequency plasma at atmospheric pressures) do not appear to be plausible. In particular, in a real application, nitrogen particles would most likely have to be taken into account, leading to an even higher quenching of excited oxygen particles. The range of different plasmas and parameter values (different geometries, duty cycle and addition of nitrogen) and of the resulting diversity of simulation approaches the literature strongly restricts the potential validation experiments. It should also be noted that in variations of the discharge and burner geometries can have particularly significant impact on residence times and therefore strongly affect the effective atomic oxygen and electronically excited oxygen species production. Due to the realistically low impact of the discharge products on the flame, the simulations in this work where chosen to be performed using the zero-dimensional model.

It remains an interesting question how the effect of complex geometries can be taken into account, without a significant rise of computational cost.

# References


[1] R. Arakoni, D. S. Stafford, N. Y. Babaeva, M. J. Kushner. *"$O_2(a^1\Delta_g)$ production in flowing $He/O_2$ plasmas. II. Two-dimensional modeling"*. Journal Of Applied Physics 98, 2005.

[2] Natalia Y. Babaevaa, Ramesh A. Arakonib, Mark J. Kushner. *"Production of $O_2(a^1\Delta_g)$ in flowing plasmas using spiker-sustainer excitation"*. J. Appl. Phys. 99, 2006.

[3] Moon Soo Bak, Hyungrok Do, Mark Godfrey Mungal, Mark A. Cappelli. *"Plasma-assisted stabilization of laminar premixed methane/air flames around the lean flammability limit"*. Combustion and Flame 159, 2012, pp. 3128-3137.

[4] V. Ya. Basevich, A. A. Belyaev. *"Hypothesis of a strong influence of singlet oxygen molecules $(a^1\Delta_g)$ on the flame speed in a $H_2$-$O_2$ mixture"*. Chem. Phys. Rep. 8, 1989, pp. 1124-1127.

[5] K. H. Becker, W. Groth, U. Schurath. *"The quenching of metastable $O_2(^1\Delta_g)$ and $O_2(b^1\Sigma_g^+)$ molecules"*. Chem. Phys. Lett 8, 1971, pp. 259-262.

[6] J. Benecke. *"Untersuchung des Einflusses von durch Plasma erzeugten, elektronisch angeregtem Sauerstoff auf die Verbrennung von Wasserstoff"*. Master's Thesis LSS-M03/13, Lehrstuhl für Strömungsmechanik und Strömungstechnik, University of Magdeburg "Otto von Guericke", 2014.

[7] L. V. Bezgin et al.. *"Evaluation of Prediction Ability of Detailed Reaction Mechanisms in the Combustion Performance in Hydrogen/Air Supersonic Flows"*. Combust. Sci. Technol., 185, 2013, pp. 62-94.

[8] G. J. M. Hagelaar and L. C. Pitchford. *"Solving the Boltzmann equation to obtain electron transport coefficients and rate coefficients for fluid models"*. Plasma Sources Sci. Technol. 14, 2005, pp. 722–733.

[9] A. Bourig, V. Lago, J.-P. Martin, K. Pliavaka, F. Pliavaka, S. Gorbatov, A. Chernukho. *"Generation of Singlet Oxygen in HV Pulsed + DC Crossed Discharge at Atmospheric Pressure for Oxygen-Enhanced Combustion"*. International Journal of Plasma Environmental Science and Technology, No.1, 2007, pp. 57-63.

[10] A. Bourig, J.-P. Martin, V. Lago, D. Thévenin, K. Zähringer. *"Modeling of the production of excited oxygen molecules in a crossed discharge (barrier discharge and CW discharge)"*. 18th International Symposium on Plasma Chemistry, 2007.

[11] A. Bourig, J.-P. Martin, V. Lago, D. Thévenin, K. Zähringer, F. Pliavaka, S. Gorbatov. *"Plasma generation of excited species for combustion enhancement"*. 18th International Symposium on Plasma Chemistry, 2007.

[12] A. Bourig, D. Thévenin, J.-P. Martin, G. Janiga, K. Zähringer, . *"Numerical modeling of $H_2$-$O_2$ flames involving electronically-excited species $O_2(a^1\Delta_g)$, $O(^1D)$ and $OH(^2\Sigma^+)$"*. Proceedings of the Combustion Institute, 2009, pp. 3171-3179.

[13] A. Bourig. *"Combustion modification by non-thermal plasma"*. PhD Thesis, Lehrstuhl für Strömungsmechanik und Strömungstechnik, University of Magdeburg "Otto von Guericke", 2014.

[14] S. Bowman, I.V.Adamovich, W.R.Lempert. *"Atomic Oxygen Measurements in $O_2(a^1\Delta_g)$ Injected Nonequilibrium Plasmas by Two Photon Absorption Laser Induced Fluorescence"*. AIAA, 2012.

[15] M. Capitelli, C. M. Ferreira, Gordiets, A. I. Osipov. *"Plasma Kinetics in Atmospheric Gases"*. Springer, 2000.

[16] M. Capitelli, D. Bruno, A. Laricchiuta. *"Fundamental Aspects of Plasma Chemical Physics"*. Springer, 2013.

[17] M. Deminsky, V. Chorkov, G. Belov, I. Cheshigin, A. Knizhnik, E. Shulakova., M. Shulakov, I. Iskandarova, V. Alexandrov, A. Petrusev, I. Kirillov, M. Strelkova, S. Umanski, B. Potapkin. *"Chemical Workbench(R) 4.0, Kintech laboratory"*. `http//www.kintechlab.com/products/chemical-workbench`, all library references dated August 2015. Comput. Mater. Sci., 2003, p.169

[18] I. Chernysheva et al. *"Chemical Workbench(R) 4.0, Kintech laboratory, mechanism library"*, "Discharge in He $O_2$ gas mixture", `http//www.kintechlab.com/products/chemical-workbench`, dated August 2015. Comput. Mater. Sci., 2003, p.169

[19] G. Dixon-Lewis, M.D. Smooke, J. Warnatz, G.H. Evans, R.S. Larson, R.E. Mitchell, L.R. Petzold, W.S. Reynolds, M. Caracotsios, W.E. Stewart, P. Glarborg, C. Wang, O. Adigun, W.G. Houf, C.P. Chou, S.F. Miller, P. Ho, D.J. Young. *"CHEMKIN release 4.0."*. Reaction Design, Inc., San Diego, California, 2004.

[20] G. G. Chernyi, S. A. Losev, S. O. Macheret, B. V. Potapkin. *"Physical and chemical processes in gas dynamics: Cross sections and rate constants"*. American Institute of Aeronautics and Astonautics, Inc., 2004.

[21] G. G. Chernyi, S. A. Losev, S. O. Macheret, B. V. Potapkin. *"Physical and chemical processes in gas dynamics: Physical and chemical kinetics and thermodynamics of gases and plasmas"*. American Institute of Aeronautics and Astonautics, Inc., 2004.

[22] Colby College, Waterville. *"Energy Units Converter"*. retrieved from `http://www.colby.edu/chemistry/PChem/Hartree.html` in 2015.

[23] H. J. Curran, S. M. Gallagher, and J. M. Simmie. *"A Comprehensive Modelling Study of Methane Oxidation"*. Proceedings of the European Combustion Meeting, 2003.

[24] M. A. Deminsky, I. Chernysheva, S. Umanskii, I. Kochetov, B. Potapkin, S.G. Saddoughi, J. Herbon, T.J. Sommerer. *"Low T, plasma assisted combustion in CH4/Air mixture at high pressure"*. International Plasma Chemistry Society Conference 20, 2009.

[25] D. Ellerweg, J. Benedikt, A. von Keudell, N. Knake, V. Schulz-von der Gatten. *"Characterization of the effluent of a He/$O_2$ micro scale atmospheric pressure plasma jet by quantitative molecular beam mass spectrometry"*. New Journal of Physics, Vol. 12, 2010.

[26] D. Ellerweg, A. von Keudell, N. Knake, J. Benedikt. *"Unexpected* O *and* $O_2$ *production in the effluent of* He/$O_2$ *mircroplasma jets emanating into ambient air"*. Plasma Sources Sci. Technol. 21, 2012.

[27] B. Eliasson, U. Kogelschatz. *"Basic data for modeling of electrical discharges in gases: oxygen"*. ABB Corp. Tes. Report KLR 96-11, 1986.

[28] F. Engelke. *"Aufbau der Moleküle"*. Teubner, 1985.

[29] A. Fridman, A. Chirokov, A. Gutsol. *"Non-thermal atmospheric pressure discharges"*. J. Phys. D: Appl. Phys. 38, 2005.

[30] A. Fridman, L. A. Kennedy. *"Plasma physics and engineering"*. CRC Press, 2011.

[31] G. Ya. Gerasimov and O. P. Shatalov. *"Kinetic mechasnism of combustion of hydrogran-oxygen mixtures"*. Journal of Engineering Physics and Thermophysics, Vol. 86, No. 5, 2013.

[32] G. P. Smith et al. *"GRI-Mech 3.0"*. Retrieved from `http://www.me.berkeley.edu/gri_mech/` in 2015.

[33] L. I. Grossweiner. *"Singlet Oxygen: Generation and Properties"*. Wenske Laser Center, Advocate/Ravenswood Hospital Medical Center, retrieved from `http://www.photobiology.com/educational/len2/singox.html` in 2015.

[34] T. Hemke, A. Willny, M. Gebhardt, R. P. Brinkmann, T. Mussenbrock. *"Spatially resolved simulation of a radio-frequency driven micro-atmospheric pressure plasma jet and its effluent"*. J. Phys. D: Appl. Phys. 44, 2011.

[35] G. Herzberg. *"Molecular spectra and molecular structure. Spectra of diatomic molecules. Vol. 1."*. New Jersey: D. van Nostrand Company, 1965.

[36] A. Hicks, S. Norberg, P. Shawcross, W. R. Lempert, J. W. Rich, I. V. Adamovich. *"Singlet oxygen generation in a high pressure non-self sustained electrical discharge"*. J. Phys. D: Appl. Phys. 38, 2005.

[37] J. O. Hirschfelder, C. F. Curtiss, R. B. Bird. *"The Molecular Theory of Gases and Liquids"*. Wiley, 1964.

[38] R. Y. N. Ho, J. F. Liebman, J. S. Valentine. *"Overview of the energetics and reactivity of oxygen"*. Active Oxygen in Chemistry, 1995, pp. 1-23.

[39] L. G. H. Huxley, R. W. Crompton. *"The diffusion and drift of electrons in gases"*. Wiley series in plasma physics, 1975.

[40] L. B. Ibraguimova, G. D. Smekhov, O. P. Shatalov. *"Recommended rate constants of chemical reactions in* $H_2$-$O_2$ *gas mixture with electronically excited species* $O(a^1\Delta_g), O(^1D), OH(^2\Sigma^+)$*"*. Institute of Mechanics of Lomonosov, Moscow State University, 2003.

[41] A. A. Ionin, I. V. Kochetov, A. P. Napartovich, N. N. Yuryshev. *"Physics and engineering of singlet delta oxygen production in low-temperature plasma"*. J. Phys. D: Appl. Phys. 40, 2007.

[42] A. A. Ionin, Yu M. Klimachev, A. A. Kotkov, A. Yu Kozlov, I. V. Kochetov, A. P. Napartovich, O. A. Rulev, L. V. Seleznev, D. V. Sinitsyn, N. P. Vagin, and N. N. Yuryshev. *"Influence of Nitrogen Oxides on Singlet Delta Oxygen Production in Pulsed Electric Discharge for Oxygen-Iodine Laser"*. XVII International Symposium on Gas Flow - Proc. of SPIE Vol. 7131, 2009.

[43] S. Kelly, M. M. Turner. *"Generation of reactive species by an atmospheric pressure plasma jet"*. Plasma Sources Sci. Technol. 23, 2014.

[44] S. Kelly, M. M. Turner. *"Power modulation in an atmospheric pressure plasma jet"*. Plasma Sources Sci. Technol. 23, 2014.

[45] K. S. Klopovskiy, D. V. Lopaev, N. A. Popov, A. T. Rakhimov and T. V. Rakhimova. *"Heterogeneous quenching of* $O_2(^1\Delta_g)$ *molecules in* $H_2 : O_2$ *mixtures"*. J. Phys. D: Appl. Phys. 32, 1999.

[46] N. Knake, S. Reuter, K. Niemi, V. Schulz-von der Gathen, J. Winter. *"Absolute atomic oxygen density distributions in the effluent of a micro scale atmospheric pressure plasma jet"*. J. Phys. D: Appl. Phys. 14, 2008.

[47] N. Knake, V. Schulz-von der Gathen. *"Investigations of the spatio-temporal build-up of atomic oxygen inside the micro-scaled atmospheric pressure plasma jet"*. Eur. Phys. J. D 60, 2010.

[48] A. A. Konnov. *"Implementation of the NCN pathway of prompt-NO formation in the detailed reaction mechanism"*. Combustion and Flame 156, 2009, pp. 2093-2105.

[49] A. S. Kovalev, D. V. Lopaev, Yu. A. Mankelevich, N. A. Popov, T. V. Rakhimova., A. Yu Poroykov., D. L. Carroll. *"Kinetics of* $O_2(b^1\Sigma_g^+)$ *in oxygen RF discharges"*. J. Phys. D: Appl. Phys. 38, 2005.

[50] I. N. Kosarev, N. L. Aleksandrov, S. V. Kindysheva, S. M. Starikovskaia, A. Yu. Starikovskii. *"Kinetics of ignition of saturated hydrocarbons by nonequilibrium plasma:* $CH_4$*-containing mixtures"*. Combustion and Flame 154, 2008, pp. 569-586.

[51] P. H. Krupenie. *"The Spectrum of Molecular Oxygen"*. J. Phys. Chem. Ref. Data 1, 423, 1972.

[52] N. Kuntner, U. Riedel, N. Slavinskaya, K. F. Pliavaka, K. Zähringer, D. Thévenin. *"Non-thermal plasma assisted combustion at atmospherical pressures by a high-voltage radio frequency generator"*. CNRS Conference Poster, Aerospace Thematic Workshop at Centre Paul Langevin, Aussois, France, 2013.

[53] S. Pancheshnyi, M. C. Bordage, B. Chaudhury, S. Chowdhury, G. J. M. Hagelaar, L. C. Pitchford, V. Puech, K. Bartschat, W. L. Morgan, L. Viehland, O. Zatsarinny, J. d'Urquijo, A. A. Castrejón-Pita, J. L. Hernández-Ávila, E Basurto, I. Bray, D. V. Fursa,

S. F. Biagi, Quantemol; L. L. Alves, C.M. Ferreira, I. Kochetov, A. Napartovich, Y. Itikawa, A. Stauffer, C. Brion, J. van Dijk *"LXCat project"*, retrieved from `http://nl.lxcat.net/data/set_type.php` in 2015.

[54] A. V. Lebedev, M. A. Deminsky, A. V. Zaitzevsky, B. V. Potapkin. *"Effect of* $O_2(a^1\Delta_g)$ *on the low-temperature mechanism of* $CH_4$ *oxidation"*. Combustion and Flame 160, 2013, pp. 530-538.

[55] F. Lenzner. *"Untersuchung des Einflusses von elektronisch angeregtem Sauerstoff auf die Verbrennung in einer vorgemischten Methanflamme"*. Bachelor's Thesis LSS-B06/12, Lehrstuhl für Strömungsmechanik und Strömungstechnik, University of Magdeburg "Otto von Guericke", 2012

[56] J. Li, Z. Zhao, A. Kazakov, F. L. Dryer. *"An updated comprehensive kinetic model of hydrogen combustion"*. International Journal of Chemical Kinetics, Vol. 36, Issue 10, 2004, pp. 566–575.

[57] James Y. Jeong, Jaeyoung Park, Ivars Henins, Steve E. Babayan, Vincent J. Tu,Gary S. Selwyn, Guowen Ding, Robert F. Hicks. *"Reaction Chemistry in the Afterglow of an Oxygen-Helium, Atmospheric-Pressure Plasma"*. J. Phys. Chem. A, 2000, pp. 8027-8032.

[58] V. J. Law, S. Daniels, J. L. Walsh, M. G. Kong, L. M. Graham, T. Gans. *"Non-invasive VHF monitoring of low-temperature atmospheric pressure plasma"*. Plasma Sources Sci. Technol. 19, 2010

[59] D. Liu, M. Rong, X. Wang, F. Iza, M. G. Kong, P. Bruggeman. *"Main Species and Physicochemical Processes in Cold Atmospheric-pressure* $He + O_2$ *Plasmas"*. Plasma Processes and Polymers, 2010, 7, pp. 846-865.

[60] A. P. Napartovich. *"Overview of Atomic Pressure Discharges Producing Nonthermal Plasma"*. Plasmas and Polymers, Vol. 6, 2001.

[61] K. Niemi, S. Reuter, L. M. Graham, J. Waskoenig, N. Knake, V. Schulz-von der Gathen, T. Gans. *"Diagnostic based modeling of radio-frequency driven atmospheric pressure plasmas"*. J. Phys. D: Appl. Phys. 43, 2010.

[62] K. Niemi, J. Waskoenig, N. Sadeghi, T. Gans, D. O'Connell. *"The role of helium metastable states in radio-frequency driven helium-oxygen atmospheric pressure plasma jets: measurement and numerical simulation"*. Plasma Sources Sci. Technol. 20, 2011.

[63] C. Olm et al.. *"Comparison of the performance of several recent hydrogen combustion mechanisms"*. Combustion and Flame 161, 2014, pp. 2219-2234.

[64] T. Ombrello, S. H. Won, Y. Ju, S. Williams. *"Flame propagation enhancement by plasma excitation of oxygen. Part I: Effects of* $O_3$*"*. Combustion and Flame 157, 2010, pp. 1906-1915.

[65] T. Ombrello, S. H. Won, Y. Ju, S. Williams. *"Flame" propagation enhancement by plasma excitation of oxygen. Part II: Effects of* $O_2(a)$. Combustion and Flame 157, 2010, pp. 1916-1928.

[66] Orlandini. *"Reaction mechanisms and simulation of reactive flows in the plasma reactor"*. PhD thesis, Combined Faculties for the Natural Sciences and for Mathematics, Ruperto Carola University, 2002.

[67] K. Pliavaka, A. Bourig, K. Zähringer, D. Thévenin, J.-P. Martin, V. Lago, E. Barbose, F. Pliavaka, S. Gorbatov, S. Shushkou, E. Prihodzka. *"Effect of singlet oxygen produced by cross discharge on methane combustion"*. Third International Workshop on Nonequilibrium Processes in Combustion and Plasma Based Technologies, Minks, Belarus, 2008, pp. 186-189.

[68] F. V. Pliavaka, K. F. Pliavaka, S. V. Harbatau, S. A. Zhdanok, A. P. Chernukho, V. V. Naumov, and A. M. Starik. *"Nonequilibrium electric discharge singlet-oxygen plasma source for nonthermals plasma-assisted combustion"*. Nonequilibrium processes in plasma, combustion, and atmosphere, 2010

[69] K. F. Pliavaka, K. Zähringer, F. V. Pliavaka, U. Riedel, N. Slavinskaya, N. Kuntner, D. Thévenin. *"Excited oxygen generation by atmospheric radio-frequency plasma discharge for combustion intensification"*. Proceedings, International Symposium on Nonequilibrium Processes, Plasma, Combustion and Atmospheric Phenomena, NEPCAP, 2012, pp. 174-178.

[70] K. F. Pliavaka, F. V. Pliavaka, S. Gorbatov, D. Thévenin, K. Zähringer. *"Atmospheric Generation of Excited Oxygen for Combustion Intensification by a RF Plasma Discharge"*. 6th European Combustion Meeting, 2013

[71] K. Zähringer, K. F. Pliavaka, D. Thévenin, N. Kuntner, U. Riedel. *"Influence of excited oxygen generated by a RF plasma discharge on atmospheric partially- premixed* $CH_4/O_2$ *and* $H_2/O_2$ *flames"*. 45th AIAA Plasmadynamics and Lasers Conference, 2014

[72] K. F. Pliavaka, K. Zähringer, F. V. Pliavaka, U. Riedel, N. Slavinskaya, N. Kuntner, D. Thévenin. *"Influence of oxygen excitation by a RF plasma discharge on the flow field of atmospheric partially premixed* $CH_4/O_2$ *and* $H_2/O_2$ *flames"*. 7th European Combustion Meeting (ECM), 2015

[73] N. A. Popov. *"The Effect of Nonequilibrium Excitation on the Ignition of Hydrogen-Oxygen Mixtures"*. Pleiades Publishing, Ltd., High Temperature, Vol. 45, No. 2, 2007, pp. 261-279.

[74] N. A. Popov. *"Effect of a Pulsed High-Current Discharge on Hydrogen-Air Mixtures"*. Plasma Physics Reports, 2008, Vol. 34, Issue 5, pp 376-391.

[75] N. A. Popov. *"Effect of singlet oxygen* $O_2(a^1\Delta_g)$ *molecules produced in a gas discharge plasma on the ignition of hydrogen-oxygen mixtures"*. Plasma Sources Sci. Technol. 20, 2011.

[76] Prockop L. D., Chichkova R. I.. *"Carbon monoxide intoxication: An updated review"*. Journal of the Neurological Sciences, Vol. 262, Issues 1-2, 2007, pp. 122–130.

[77] Y. P. Raizer. *"Gas discharge physics*. Springer, 1991.

[78] SanDiego. *"A. Williams, K. Seshadri"*. *"Chemical-Kinetic Mechanisms for Combustion Applications"*. `http://web.eng.ucsd.edu/mae/groups/combustion/mechanism.html`, all library references dated August 2015.

[79] Y. V. Savin, L. V. Goryachev, Y. A. Adamenkov, T. V. Rakhimova, Y. A. Mankelevich, N. A. Popov, A. A. Adamenkov, V. V. Egorov, S. P. Ilyin, Y. V. Kolobyanin, E. A Kudryashov, G. S. Rogzhnikov, B. A. Vyskubenko. *"Singlet oxygen production and quenching mechanisms in traveling microwave discharges"*. J. Phys. D: Appl. Phys. 37, 2004.

[80] D. Schröder, H. Bahre, N. Knake, J. Winter, T. de los Arcos, V. Schulz-von der Gathen. *"Influence of target surfaces on the atomic oxygen distribution in the effluent of a micro-scaled atmospheric pressure plasma jet"*. Plasma Sources Sci. Technol. 21, 2012.

[81] C. Schweitzer, R. Schmidt. *"Physical Mechanism of Generation and Deactivation of Singlet Oxygen"*. Chem. Rev., 2003, pp. 1685-1757

[82] A. S. Sharipov, A. M. Starik. *"Kinetic mechanism of* $CO$-$H_2$ *system oxidation promoted by excited singlet oxygen molecules"*. Combustion and Flame 159, 2012, pp. 16-29.

[83] A. S. Sharipov, A. M. Starik. *"Analysis of the reaction and quenching channels in a* $H + O_2(a^1\Delta_g)$ *system"*. Phys. Scr. 88, 2013.

[84] V. V. Smirnov, O. M. Stelmakh, V. I. Fabelinsky, D. N. Kozlov, A. M. Titova. *"Numerical Simulation of a Hydrogen-Oxygen Mixture in View of Electronically Excited Components"*. High Temperature, Vol. 45, No. 3, 2007, pp. 395-407.

[85] I. W. M. Smith. *"Kinetics and dynamics of elementary gas reactions"*. Butterworth, 1980.

[86] V. V. Smirnov, O. M. Stelmakh, V. I. Fabelinsky, D. N. Kozlov, A. M. Titova. *"On the influence of electronically excited oxygen on combustion of hydrogen-oxygen mixture"*. J. Phys. D: Appl. Phys. 41, 2008.

[87] J. S. Sousa, G. Bauville, B. Lacour, V. Puech, M. Touzeau, L. C. Pitchford. *"*$O_2(a^1\Delta_g)$ *production at atmospheric pressure by microdischarge"*. Applied Physics Letters 93, 2008.

[88] J. S. Sousa, K. Niemi, L. J. Cox, Q. Th. Algwari, T. Gans, D. O'Connell. *"Cold atmospheric pressure plasma jets as sources of singlet delta oxygen for biomedical applications"*. Journal Of Applied Physics 109, 2011.

[89] K. R. Stalder, R. J. Vidmar, G. Nersisyan, and W. G. Graham. *"Modeling the chemical kinetics of high-pressure glow discharges in mixtures of helium with real air"*. J. Appl. Phys. 99, 2006.

[90] D. S. Stafford, M. J. Kushner. *"*$O_2(a^1\Delta_g)$ *production in* $He/O_2$ *mixtures in flowing low pressure plasmas"*. Journal Of Applied Physics 96, 2004.

[91] D. S. Stafford, M. J. Kushner. *"*$O_2(a^1\Delta_g)$ *production in flowing* $He/O_2$ *plasmas. I. Axial transport and pulsed power formats"*. Journal Of Applied Physics 98, 2005.

[92] A. M. Starik, V. E. Kozlov and N. S. Titova. *"On mechanisms of a flame velocity increase upon activation of* $O_2$ *molecules in electrical discharge"*. J. Phys. D: Appl. Phys. 41, 2008.

[93] A. M. Starik, V. E. Kozlov, N. S. Titova. *"On the influence of singlet oxygen molecules on the speed of flame propagation in methane-air mixture"*. Combustion and Flame 157, 2010, pp. 313-327.

[94] A. M. Starik, B. I. Loukhovitski and A. P. Chernukho. *"Comprehensive analysis of combustion enhancement mechanisms in a supersonic flow of* $CH_4 - O_2$ *mixture with electric-discharge-activated oxygen molecules"*. Plasma Sources Sci. Technol. 21, 2012.

[95] A. M. Starik, L. V. Bezgin, V. I. Kopchenov, B. I. Loukhovitski, A. S. Sharipov, N. S. Titova. *"Numerical study of the enhancement of combustion performance in a scramjet combustor due to injection of electric-discharge-activated oxygen molecules"*. Plasma Sources Science and Technology 22, 2013.

[96] A. M. Starik, B. I. Loukhovitski, A. S. Sharipov, N. S Titova. *"Physics and chemistry of the influence of excited molecules on combustion enhancement"*. Philosophical Transactions A, Vol. 373, 2015, Issue 2048.

[97] A. Yu. Starikovskii. *"Plasma supported combustion"*. Proceedings of the Combustion Institute 30, 2005, pp. 2405-2417.

[98] A. Starikovskiy, N. Aleksandrov. *"Plasma-assisted ignition and combustion"*. Progress in Energy and Combustion Science 39, 2013, pp. 61-110.

[99] A. M. Starik, B. I. Loukhovitski, A. S. Sharipov, N. S Titova. *"Physics and chemistry of plasma-assisted combustion.* Philosophical Transactions A, Vol. 373, 2015, Issue 2048.

[100] Kinetic effects of non-equilibrium plasma-assisted methane oxidation on diffusion flame extinction limits. *"Wenting Sun, Mruthunjaya Uddi, Sang Hee Wona, Timothy Ombrello, Campbell Carter, Yiguang Ju"*. Combustion and Flame 159, 2012, 221–229

[101] W. Sun, S. H. Won, Y. Ju. *"In situ plasma activated low temperature chemistry and the S-curve transition in DME/oxygen/helium mixture"*. 8th U.S. National Combustion Meeting , 2013.

[102] M. Uddi, N. Jiang, I. V. Adamovich, W. R. Lempert. *"Nitric oxide density measurements in air and air/fuel nanosecond pulse discharges by laser induced fluorescence"*. J. Phys. D: Appl. Phys. 42, 2009.

[103] N. P. Vagin, A. A. Ionin, Yu M. Klimachev, I. V. Kochetov, A. P. Napartovich, D. V. Sinitsyn, N. N. Yuryshev. *"Glow Discharge in Singlet Oxygen"*. Plasma Physics Reports, Vol. 29, No. 3, 2003, pp. 211-219.

[104] A. N. Vasileva, K. S. Klopvskiy, A. S. Kovalev, D. V. Lopaev, Y. A. Mankelevich, N. A. Popov, A. T. Rakhimov, T. V. Rakhimova. *"Production of Singlet Oxygen in a Non-Self-Sustained Discharge"*. Plasma Physics Reports, Vol. 31, No. 4, 2005, pp. 325–337.

[105] A. N. Vasileva, K. S. Klopvskiy, A. S. Kovalev, D. V. Lopaev, Y. A. Mankelevich, N. A. Popov, A. T. Rakhimov, T. V. Rakhimova. *"On the possibility of* $O_2(a^1\Delta_g)$ *production by a non-self-sustained discharge for oxygen-iodine laser pumping"*. J. Phys. D: Appl. Phys. 37, 2004.

[106] J. Warnatz, U. Maas, R. W. Dibble. *"Verbrennung"*. Springer Verlag, 2001.

[107] J. Waskoenig, K. Niemi, N. Knake, L. M. Graham, S. Reuter, V. Schulz-von der Gathen, T. Gans. *"Atomic oxygen formation in a radio-frequency driven micro-atmospheric pressure plasma jet"*. Plasma Sources Science and Technology 19, 2010.

[108] D. Weldon, T. D. Poulsen, K. V. Mikkelsen, P. R. Ogilby. *"Singlet Sigma: The "Other" Singlet Oxygen in Solution"*. Photochemistry and Photobiology, 2003, pp. 369-379.

[109] X. Yuan, L. L. Raja. *"Computational Study of Capacitively Coupled High-Pressure Glow Discharges in Helium"*. IEEE transactions on plasma science, Vol. 31, No. 4, 2003.

# Appendix

## A Physical constants

| Quantity | Name | Value |
|---|---|---|
| $h$ | Planck constant | $6.626 \times 10^{-34}\,\mathrm{m^2\,kg/s}$ |
| $k_B$ | Boltzmann constant | $1.381 \times 10^{-23}\,\mathrm{kg\,m^2 s^{-2}/K}$ |
| $N_A$ | Avogadro constant | $6.022 \times 10^{23}/\mathrm{mol}$ |
| $\mathfrak{q}_{\mathrm{e}^-}$ | Electrical charge | $1.602 \times 10^{-19}\,\mathrm{A\,s}$ |
| $C_p^{\mathrm{He}}$ | Heat capacity of He | $\approx 20.7862\,\mathrm{J/(mol\,K)}$ |
| $C_p^{\mathrm{O_2/He}}$ | Heat capacity of $O_2$/He mixtures | $\approx 21.3\,\mathrm{J/(mol\,K)}$ |
| $D$ | Diffusion coefficient of $O_2$/He mixtures | $5 \times 10^{-3}\,\mathrm{cm^2/s}$ to $5 \times 10^{-2}\,\mathrm{cm^2/s}$ |

Table 37: Physical constants.

Recall that $1\,\mathrm{eV} = \mathfrak{q}_{\mathrm{e}^-}\,\mathrm{V} \approx 1.6 \times 10^{-19}\,\mathrm{J} \approx 96.49\,\mathrm{kJ/mol}$.

We also use the norm cubic meter $\mathrm{Nm}^3 \approx 44.615\,\mathrm{mol}$.

The following is a list of relevant steel electrode data as found in Kelly et al. [43]:

- Thermal conductivity: $44.5\,\mathrm{W/(m\,K)}$.
- Material density: $7850\,\mathrm{kg\,m^{-3}}$.
- Heat capacity: $475\,\mathrm{J/(kg\,K)}$.

## B Implementation of the Boltzmann equation

In the following, we present the differential equation implemented in the software *Chemical Workbench* as found in the manual and comment on it. The electron flux along the energy axis is

$$J_e(f) = -\frac{1}{3}\sqrt{\frac{2}{m_e}}\left(e\frac{E}{N}\right)^2 \frac{\varepsilon}{\sum_k \mathrm{x}_k\,\sigma_{mk}(\varepsilon)} N \frac{\partial}{\partial\varepsilon} f(\varepsilon)$$

and governed by the equation

$$\sqrt{\varepsilon}\,\frac{\partial}{\partial t} f(\varepsilon) = -\frac{\partial}{\partial\varepsilon} J_e(f) + N \sum_i Q_i(f).$$

Here, $m_e, M_k$ are the masses and $\mathrm{x}_k$ denotes the molar fraction of the $k^{\text{th}}$ species and is not to be confused with a spatial variable, denoted by $x$ in this text. Furthermore, $Q_i(f)$ are several collision integrals (or rather sums) and $I_{kj}$ is the threshold for the $j$'th inelastic process for the $k^{\text{th}}$ species. $B_{0k}$ is the rotational constant of the $k^{\text{th}}$ molecule and $\Lambda$ is the Coulomb logarithm:

- $Q_{el}[f] = \sqrt{8m_e}\frac{\partial}{\partial\varepsilon}\left[\left(\sum_k \frac{\mathrm{x}_k\,\sigma_{mk}(\varepsilon)}{M_k}\right)\varepsilon^2\left(f(\varepsilon) + k_B T_{mathrmg}\frac{\partial}{\partial\varepsilon}f(\varepsilon)\right)\right].$

The expression $Q_{el}$ describes the elastic collisions.

- $Q_{rot}[f] = 4\sqrt{\frac{2}{m_e}}\left[\sum_k B_{0k}\,\mathrm{x}_k\,\sigma_{rot,k}(\varepsilon)\right]\frac{\partial}{\partial\varepsilon}\left[\varepsilon\,f(\varepsilon)\right].$

The expression $Q_{rot}$ describes the energy exchange due to rotational excitation. The energy expression is proportional to the rotational constant.

- $Q_{in}[f] = \sqrt{\frac{2}{m_e}}\sum_k \mathrm{x}_k \sum_l \left[(\varepsilon + I_{kj})\,\sigma_{kj}(\varepsilon + I_{kj})\,f(\varepsilon + I_{kj}) - \varepsilon\,\sigma_{kj}(\varepsilon)\,f(\varepsilon)\right].$

The expression $Q_{in}$ describes the energy exchange due to various inelastic processes.

- $Q_{sup}[f] = \sqrt{\frac{2}{m_e}}\sum_k \mathrm{x}_k \sum_l \left[(\varepsilon + I_{kj})\,\hat{\sigma}_{kj}(\varepsilon + I_{kj})\,f(\varepsilon + I_{kj}) - \varepsilon\,\hat{\sigma}_{kj}(\varepsilon)\,f(\varepsilon)\right].$

The expression $Q_{sup}$ describes the energy exchange due to super-elastic processes.

- $Q_{att}[f] = -\sqrt{\frac{2}{m_e}}\left[\sum_k \mathrm{x}_k\,\sigma_{att,k}(\varepsilon)\right]\frac{\partial}{\partial\varepsilon}\varepsilon\,f(\varepsilon).$

The expression $Q_{att}$ describes the energy exchange and electron loss due to electron attachment to heavy particles.

- $Q_{ee}[f] = n_e \ln(\Lambda)\frac{\partial}{\partial\varepsilon}\left[f(\varepsilon)\int_0^\varepsilon \sqrt{\varepsilon}f(\varepsilon)\mathrm{d}\varepsilon + \left[\int_0^\varepsilon \varepsilon^{3/2}f(\varepsilon)\mathrm{d}\varepsilon + \varepsilon^{3/2}\int_\varepsilon^\infty f(\varepsilon)\mathrm{d}\varepsilon\right]\frac{2}{3}\frac{\partial}{\partial\varepsilon}f(\varepsilon)\right].$

The expression $Q_{ee}$ describes electron-electron interactions. This is why here we find the electron density and the electron distribution function itself in the expression. The power

$$P = F \cdot v_{\text{dr}} \propto E \cdot v_{\text{dr}}$$

can be considered the energy of the discharge spent per unit time. Hence, if $I_{ij}$ is an energy rise for a gas species per $ij$-collision, the number

$$\eta(i,j) := \frac{I_{ij} \cdot k_{ij}\mathrm{x}_i N}{E \cdot v_{\text{dr}}}$$

expresses the relative energy input efficiency distribution of the discharge. Similar ratios over the product $E \cdot v_{\text{dr}}$ can be formed to express the distribution for elastic and super-elastic processes.

# Curriculum vitae

| | |
|---|---|
| Name: | • Mag. Nikolaj Kuntner |
| Geboren: | • 19. November 1986 |
| Nationalität: | • Österreichisch |

| | |
|---|---|
| seit 06/2016 | • Konsultant für das **Kuratorium für Verkehrssicherheit** der Stadt Wien, statistische Auswertung von Polizeidaten zu Autounfällen in Österreich; freier Dienstvertrag |
| seit 03/2016 | • Techniker beim **Institute of Science and Technology Austria** in Klosterneuburg, Python-Programmierung von Messroutinen von Experimenten im Bereich der Elektrotechnik sowie der grafischen Interfaces für Instrumente, Verwaltung von Soft- und Hardware; Teilzeit |
| 11/2015 – 04/2016 | • Industriepraktikum bei **Infineon Technologies** am Standort Villach, MatLab-Programmierung, statistische Auswertung von Halbleiterbauelement-Fertigungsfehlern; Teilzeit |
| 07/2015 – 10/2015 | • Wissenschaftlicher Mitarbeiter am **Deutschen Zentrum für Luft- und Raumfahrt** in Stuttgart |
| seit 04/2012 | • Doktoratsstudium der Luft- und Raumfahrttechnik und Geodäsie an der **Universität Stuttgart** |
| 12/2011 – 10/2015 | • Bearbeitung des DFG-Projektes mit dem Titel „Verbrennung erneuerbarer Brennstoffe unter Zuhilfenahme nicht-thermischer Plasmen" im Rahmen der Doktorarbeit an der **Universität Stuttgart** unter Prof. Dr. Uwe Riedel am Deutschen Zentrum für Luft- und Raumfahrt |
| 02/2011 – 03/2011 | • Industriepraktikum beim **Austrian Center of Competence for Tribology** in Wiener Neustadt, MatLab-Programmierung, Computer-Simulationen von molekularen Grenzschichten |
| 10/2006 – 09/2011 | • Magisterstudium der Physik an der **Universität Wien**, Diplomarbeit unter H. Steinacker im Bereich der Differentialgeometrie |
| 10/2005 – 10/2006 | • Zivildienst beim **Arbeiter-Samariter-Bund** als Rettungssanitäter |
| 10/1997 – 10/2005 | • Matura am **Realgymnasium Rahlgasse** in Wien |